THE *HST*/ACS+WFC3 SURVEY FOR LYMAN LIMIT SYSTEMS. II. SCIENCE

John M. O'Meara[1], J. Xavier Prochaska[2], Gabor Worseck[2], Hsiao-Wen Chen[3], and Piero Madau[2]
[1] Department of Chemistry and Physics, Saint Michael's College. One Winooski Park, Colchester, VT 05439, USA
[2] Department of Astronomy and Astrophysics, UCO/Lick Observatory, University of California, 1156 High Street, Santa Cruz, CA 95064, USA
[3] Department of Astronomy and Astrophysics, University of Chicago, 640 S. Ellis Ave, Chicago, IL 60637, USA

ABSTRACT

We present the first science results from our *Hubble Space Telescope* survey for Lyman limit absorption systems (LLS) using the low dispersion spectroscopic modes of the Advanced Camera for Surveys and the Wide Field Camera 3. Through an analysis of 71 quasars, we determine the incidence frequency of LLS per unit redshift and per unit path length, $\ell(z)$ and $\ell(X)$, respectively, over the redshift range $1 < z < 2.6$, and find a weighted mean of $\ell(X) = 0.29 \pm 0.05$ for $2.0 < z < 2.5$ through a joint analysis of our sample and that of Ribaudo et al. Through stacked spectrum analysis, we determine a median (mean) value of the mean free path to ionizing radiation at $z = 2.4$ of $\lambda_{\mathrm{mfp}}^{912} = 243(252)\, h_{72}^{-1}$ Mpc, with an error on the mean value of $\pm 43\, h_{72}^{-1}$ Mpc. We also re-evaluate the estimates of $\lambda_{\mathrm{mfp}}^{912}$ from Prochaska et al. and place constraints on the evolution of $\lambda_{\mathrm{mfp}}^{912}$ with redshift, including an estimate of the "breakthrough" redshift of $z = 1.6$. Consistent with results at higher z, we find that a significant fraction of the opacity for absorption of ionizing photons comes from systems with $N_{\mathrm{H\,I}} \leqslant 10^{17.5}$ cm^{-2} with a value for the total Lyman opacity of $\tau_{\mathrm{eff}}^{\mathrm{Lyman}} = 0.40 \pm 0.15$. Finally, we determine that at minimum, a 5-parameter (4 power law) model is needed to describe the column density distribution function $f(N_{\mathrm{H\,I}}, X)$ at $z \sim 2.4$, find that $f(N_{\mathrm{H\,I}}, X)$ undergoes no significant change in shape between $z \sim 2.4$ and $z \sim 3.7$, and provide our best fit model for $f(N_{\mathrm{H\,I}}, X)$.

Key words: cosmology: observations – intergalactic medium – quasars: absorption lines – quasars: general – surveys – ultraviolet: general

Online-only material: color figures, machine-readable tables

1. INTRODUCTION

The importance of Lyman limit systems (LLS), those quasar absorption line systems with $N_{\mathrm{H\,I}} > 10^{17.2}$ cm^{-2}, has been well understood. Studies of LLS at redshifts $z > 2.6$ stretch back many decades, with the LLS being some of the first absorption line systems studied quantitatively (Tytler 1982). Through to the present day, ground-based surveys of the LLS span the full range of observability, $2.6 > z > 6$ (e.g., Sargent et al. 1989; Storrie-Lombardi et al. 1994; Péroux et al. 2001; Songaila & Cowie 2010; Prochaska et al. 2010). The 1990s also introduced studies of the LLS from space (e.g., Stengler-Larrea et al. 1995), with the largest datasets being provided by the Faint Object Spectrograph and Space Telescope Imaging Spectrograph on board the *Hubble Space Telescope* (*HST*) spanning the range $0.3 < z < 2.6$ (see Ribaudo et al. 2011 for a summary). The space-based studies peak in sensitivity at $z \sim 1$, declining to both higher and lower redshifts. Nearly all early studies of the LLS provided a general picture of a rapidly evolving population with an incidence frequency described by a $(1 + z)^{\gamma}$ power law, and $\gamma \simeq 1.5$. Early studies also provided constraints on the column density distribution function, describing it as a single power law over the full range in LLS hydrogen column density (e.g., Tytler 1987; Lanzetta 1991; Petitjean et al. 1993), while more recent studies (e.g., Péroux et al. 2003; O'Meara et al. 2007; Prochaska et al. 2010) have considered more complicated descriptions.

The optical depths from LLS at 1 ryd, combined with their increased frequency per unit redshift compared to the higher $N_{\mathrm{H\,I}}$ damped Lyα systems (DLAs; $N_{\mathrm{H\,I}} \geqslant 10^{20.3}$ cm^{-2}), suggest that they strongly influence, if not dominate, the attenuation of photons emitted by galaxies and quasars, and thus set the intensity of the extragalactic UV background, and determine the mean free path of ionizing photons in the intergalactic medium (IGM; e.g., Miralda-Escudé 2003; Prochaska et al. 2009, hereafter PWO09; Dall'Aglio et al. 2008; Calverley et al. 2011; McQuinn et al. 2011; Haardt & Madau 2012). Thus, LLS play a crucial role in the cosmological history of interplay between radiation and baryons.

Both the low density, highly ionized Lyα forest ($N_{\mathrm{H\,I}} < 10^{17.2}$ cm^{-2}) and the high density, predominantly neutral DLAs have been well studied and constrained in part because of their relative ease of observation. The Lyα forest is ubiquitous in quasar spectra, is visible from the ground at $z > 1.6$, and is relatively easy to constrain in terms of $N_{\mathrm{H\,I}}$ owing to its lack of saturation in the Lyman series. One must go to higher order Lyman series transitions to determine the $N_{\mathrm{H\,I}}$ as $N_{\mathrm{H\,I}}$ increases, but this can be achieved with high signal-to-noise ratio (S/N), high-resolution data (e.g., Rudie et al. 2012). The DLA show strong damping wing features in their Lyα line, allowing for easy determination of their $N_{\mathrm{H\,I}}$ even in low-resolution data (e.g., Wolfe et al. 2005). By contrast, the LLS, although frequently observed, are by comparison poorly constrained, as both the Lyα line and the Lyman break must be well covered in the spectrum to constrain the $N_{\mathrm{H\,I}}$ (e.g., Prochter et al. 2010). At the low end of the LLS H I column density range, significant wavelength coverage at rest wavelengths in the LLS frame of $\lambda < 912$ Å are required to accurately determine the $N_{\mathrm{H\,I}}$ through the shape of the recovery in flux. These complications place stronger constraints on the redshift range where large statistical surveys for LLS can be done from the ground, namely $z > 2.5$.

Nevertheless, our motivation for studying the LLS is clear. A complete census of absorption across the full range of $N_{\rm H\,I}$ is required to understand the properties of the IGM at a given redshift, and the evolution in redshift of that census provides tests of models of structure formation, evolution in the UV background, and the interplay between galaxies and their environment. At $z \sim 3.7$, Prochaska et al. (2010, hereafter POW10) analyzed spectra from the Sloan Digital Sky Survey (SDSS) DR7 catalog to establish the incidence frequency of LLS and to characterize a number of biases inherent in LLS analysis at any redshift. PWO09 also use the SDSS DR7 catalog, and produce a measurement of the mean free path to ionizing radiation, $\lambda_{\rm mfp}^{912}$, over the same redshift range in POW10. Combined with the incidence frequency measurements and measurements of the Lyα forest, LLS, and DLA in the literature, POW10 determined the column density distribution function $f(N_{\rm H\,I}, X)$ at $z = 3.7$. This $f(N_{\rm H\,I}, X)$ underscores the importance of the LLS to our complete understanding of absorbers in the universe, as it showed that a number of strong inflections in $f(N_{\rm H\,I}, X)$ exist at this redshift. Recent developments in theoretical models and simulations of the LLS regime (e.g., Altay et al. 2011) have made significant improvements in reproducing these inflections with the inclusion of self-shielding. The path forward is now clear: to move beyond a simple counting of the LLS and to extend the knowledge of $f(N_{\rm H\,I}, X)$ and $\lambda_{\rm mfp}^{912}$ to both higher and lower redshifts to provide a determination of their evolution with cosmic time, and to better understand their physical nature.

At lower redshifts ($z < 2.5$), a determination of $f(N_{\rm H\,I}, X)$ and $\lambda_{\rm mfp}^{912}$ which includes contribution from LLS is made difficult by the simple fact that one must go to space-based telescopes to obtain coverage of the Lyman break at rest wavelength $\lambda = 912$ Å. The region $1 < z < 2.5$ is particularly difficult, as most space-based instruments have poor NUV throughput at high resolution. Previous studies of LLS at $z < 2.5$ offered differing results regarding the evolution of the incidence frequency $\ell(z)$ of the LLS. Lanzetta (1991) argued for a fairly constant $\ell(z)$ with rapid evolution at higher z, whereas Stengler-Larrea et al. (1995) and Storrie-Lombardi et al. (1994) argued for a single power law evolution over the entire range $0 < z < 4$. Recently, Ribaudo et al. (2011) performed an *HST* archival study of the LLS frequency distribution at $z < 2.5$, with the bulk of their statistical power at $0.75 < z < 1.5$. They find that the LLS frequency with redshift $\ell(z)$ is well described by a power law $\ell(z) \propto (1 + z)^{\gamma}$ with $\gamma = 1.33 \pm 0.61$ at $z < 2.6$. They place constraints on $f(N_{\rm H\,I}, X)$ and $\lambda_{\rm mfp}^{912}$ (finding that the former is incompatible with a single power law), but do so largely by relying on measurements at redshifts different from the bulk of their sample for the higher column density LLS and the DLA.

In this paper, we present the first set of scientific results from our campaign to better explore the LLS at redshifts where our knowledge of optically thick systems is poorly constrained, namely $1 < z < 2.6$. Our data sample comes from a survey performed with the *HST* using the low-resolution NUV spectroscopic modes of the Advanced Camera for Surveys and the Wide Field Camera 3 instruments. The survey is described in the first paper in this series, O'Meara et al. (2011), which we refer to hereafter as Paper I. This paper is organized as follows: Section 2 summarizes the results of Paper I, Section 3 describes how we model LLS absorption in our sample, Section 4 describes our statistical analysis and results for the incidence frequency of the LLS, Section 5 describes our analysis of stacked spectra and the determination of the mean free path of ionizing photons under specific assumptions regarding the stacked QSO spectral energy distribution (SED) and any intrinsic inflections it might have, Section 6 presents our analysis of the column density distribution function, and Section 7 offers a summary and discussion.

Unless stated otherwise, all results in this paper assume a "standard" Lambda+CDM cosmology with $H_0 = 72$ km s^{-1} Mpc^{-1}, $\Omega_m = 0.26$, and $\Omega_\Lambda = 0.74$.

2. SUMMARY OF QUASAR SELECTION AND *HST* DATASETS

In Paper I, we reported in detail the quasar sample and *HST* observations for our survey. We also described the reduction procedures and presented the extracted 1D spectra that form the basis of the following analysis. This section provides a brief summary of Paper I.

For our *HST* snapshot programs in Cycles 15 and 17, we selected 100 quasars at $z_{\rm em} \approx 2.5$ from SDSS Data Release 5 based primarily on their optical photometry. Specifically, we restricted the list to quasars with $g < 18.5$ mag, $2.30 < z_{\rm em} < 2.60$, and spectra without very strong associated absorption. Because the SDSS quasar spectroscopic sample is based primarily on optical color selection (Richards et al. 2002), it is possible it may be biased relative to a complete quasar sample (e.g., Worseck & Prochaska 2011). Indeed, PWO09 demonstrated that the cohort of SDSS quasars at $z \approx 3.5$ are biased *toward* sightlines with strong Lyman limit absorption in the *u*-band. For our selection criteria, the presence of an intervening LLS should have negligible effect on the quasar colors. Nevertheless, quasars at $z \sim 2.5$ have a typical color that is sufficiently close to the stellar locus that the SDSS team chose selection criteria that favor UV-excess quasars. Worseck & Prochaska (2011) have demonstrated that this biases the spectroscopic sample at $z \sim 2.6$ to have bluer SEDs than a complete sample (see their Figure 16). We return to this issue later in the paper.

From this list (see Table 1 of Paper I), 18 quasars were queued in Cycle 15 to observe with the ACS/PR200L prism and 53 quasars with the WFC3/UVIS-G280 grism in Cycle 17. We developed customized software to extract, wavelength calibrate, and flux the data to produce a fully calibrated 1D spectrum for each quasar. The ACS/PR200L spectra cover observed wavelengths $\lambda = 1500$–5000 Å and the WFC3/UVIS-G280 spectra span roughly $\lambda = 2000$–6000 Å. Our spectra have relatively high S/N per pixel down to $\lambda \approx 1800$ Å for the ACS dataset and $\lambda \approx 2000$ Å for the WFC3/UVIS-G280 dataset. This reflects the relatively high UV fluxes of the quasars and the low dispersion of the spectrometers: at $\lambda = 2500$ Å the spectra have FWHM ≈ 60 Å. Uncertainties in the wavelength calibration are on the order of 2 pixels, in the form of a rigid shift in pixel space. Table 1 summarizes the quasars comprising the survey.

3. FITTING FOR LYMAN LIMIT ABSORPTION

The principal goal of our *HST* program was to survey $z \sim 2.5$ quasars for Lyman limit absorption at $z \lesssim 2$. At these redshifts, the Lyman limit lies below Earth's atmospheric cutoff and one requires space-borne UV spectroscopy. Because the Lyman limit is a continuum opacity, its analysis does not require high spectral resolution. Instead, well-fluxed spectra with high S/N, and, ideally, quasars without complex continua are preferred. Our dataset nicely achieves these criteria (Paper I).

Table 1
Quasar Sample and Continuum

Object Name	Plate[a]	Fiber[a]	z_{em}	g	C[b]	α[b]
Quasars Observed with WFC3/UVIS-G280						
J075547.83+220450.1	1264	163	2.319	17.58	92.3	0.4
J075158.65+424522.9	434	555	2.453	17.77	58.0	0.6
J084525.84+072222.3	1298	512	2.307	17.87	49.8	0.5
J085045.44+563618.7	448	466	2.464	18.05	65.7	0.3
J085316.55+445616.6	897	392	2.540	18.17	74.8	0.4
J085417.60+532735.2	449	273	2.418	17.20	113.4	0.9
J080620.47+504124.4	1780	181	2.457	17.57	144.1	0.0
J083326.82+081552.0	1759	283	2.581	17.80	90.9	0.1
J090938.71+041525.8	1193	296	2.444	18.01	73.1	0.2
J094942.34+052240.3	994	245	2.282	17.75	90.9	0.5
J105315.89+400756.4	1435	205	2.482	18.15	49.8	0.2
J100541.26+570544.6	558	30	2.308	18.02	90.5	0.0
J101120.39+031244.6	574	281	2.458	17.79	127.7	0.3
J113550.68+460705.0	1442	1	2.496	17.67	87.2	0.4
J114358.52+052445.0	838	591	2.561	16.95	190.7	0.3
J110735.58+642008.7	596	385	2.316	17.38	171.9	0.1
J111928.38+130251.0	1605	406	2.394	18.01	56.9	0.5
J110411.62+024655.3	508	520	2.532	18.21	41.5	0.5
J124831.65+580928.9	1317	577	2.599	17.74	77.9	0.2
J125345.49+051611.3	848	438	2.398	17.99	49.7	0.4
J125914.85+672011.8	495	494	2.443	17.93	97.8	0.2
J121519.42+424851.0	1450	486	2.310	17.73	124.0	0.2
J122015.50+460802.4	1371	327	2.446	18.01	81.9	0.4
J122836.05+510746.2	971	448	2.450	17.88	94.6	0.0
J123515.84+630113.4	780	546	2.383	17.38	157.8	0.4
J133521.96+454238.2	1463	29	2.452	18.00	114.3	0.0
J130055.67+055620.5	849	330	2.446	17.99	95.6	0.2
J130240.16+025457.6	524	427	2.414	17.84	117.5	0.2
J131123.09+453159.4	1375	459	2.403	18.20	61.8	0.0
J131855.75+531207.2	1041	319	2.321	18.08	70.3	0.5
J132312.83+414933.0	1462	482	2.440	18.06	105.2	0.4
J132552.17+663405.7	496	114	2.511	17.92	105.3	0.3
J133433.88+035545.2	853	220	2.583	18.14	89.3	0.2
J133523.82+463742.1	1463	586	2.474	17.97	86.7	0.0
J133646.56+015741.9	528	141	2.379	17.94	112.0	0.0
J134211.98+601525.0	786	255	2.399	17.91	101.2	0.1
J135412.28+542100.1	1323	213	2.294	17.98	72.5	0.3
J135445.66+002050.3	301	385	2.504	18.07	65.6	0.0
J135831.78+050522.8	856	469	2.455	17.17	155.9	0.4
J141528.47+370621.2	1643	537	2.374	17.63	96.3	0.3
J140028.81+643030.9	498	296	2.359	18.09	56.4	0.5
J145453.53+032456.8	588	103	2.368	17.97	95.4	0.0
J153335.82+384301.1	1293	30	2.529	17.50	128.3	0.2
J153514.65+483659.7	1167	471	2.542	17.84	108.0	0.1
J154042.98+413816.3	1053	306	2.516	17.46	89.7	0.0
J162516.42+294318.3	1421	463	2.357	17.72	70.6	0.3
J161003.54+442353.7	814	301	2.588	18.24	46.7	0.2
J162548.79+264658.7	1408	281	2.518	17.34	234.4	0.0
J165137.52+400218.9	630	560	2.343	17.46	109.1	0.6
J172409.19+531405.5	359	189	2.547	17.87	52.8	0.6
J211157.78+002457.5	986	403	2.325	17.85	94.0	0.3
J213629.44+102952.2	731	56	2.555	17.98	59.1	0.2
J233823.16+150445.2	747	493	2.419	17.62	108.9	0.2
Quasars Observed with ACS/PR200L						
J010657.94−085500.1	659	420	2.350	18.08	2.6	0.0
J023359.71+004938.5	407	600	2.522	17.85	4.0	0.4
J034024.57−051909.2	462	445	2.340	17.95	3.9	0.0
J040241.42−064137.9	464	32	2.432	17.93	3.0	0.1
J084619.53+365836.8	865	135	2.335	18.18	3.3	0.3
J080413.66+251633.8	1205	164	2.302	17.90	1.9	3.0
J085952.36+350724.7	1211	506	2.373	18.22	2.5	0.6
J092849.24+504930.5	767	41	2.349	18.14	3.1	0.1
J102900.79+622342.0	773	314	2.470	17.78	5.9	0.6

Table 1
(Continued)

Object Name	Plate[a]	Fiber[a]	z_{em}	g	C[b]	α[b]
J104321.55+624127.3	773	177	2.355	17.74	4.3	2.2
J114311.61+651513.5	597	604	2.392	17.59	4.7	0.0
J121944.79+461015.3	1451	140	2.484	18.02	2.5	0.1
J120729.75+042909.9	842	68	2.413	18.21	1.5	0.3
J145554.30+521828.5	1164	288	2.348	17.77	3.9	0.7
J165914.54+380900.7	632	120	2.343	18.12	3.0	1.2
J161815.53+370103.9	1056	623	2.496	17.74	4.1	0.2
J161538.88+392051.1	1336	137	2.315	18.11	3.0	0.0
J230011.74−102144.4	725	295	2.297	18.26	3.1	0.0

Notes. Quasars observed as part of our WFC3/UVIS-G280 and *HST*/ACS survey for LLS absorption (Paper I).
[a] SDSS-DR7 designations.
[b] Absorbed continuum fitting parameters. The modeled continuum is of the form: $f_\lambda^{conti} = C f_\lambda^{Telfer} (\lambda/2500\,\text{Å})^\alpha$. We caution the reader that these models are not meant to precisely describe the intrinsic spectral energy distributions of the quasars, but instead describes the flux attenuated by the Lyman series absorption (see the text).

Our approach to the Lyman limit analysis is straightforward. First, we must estimate the observed flux of each source in the absence of Lyman continuum opacity. This quantity is not the intrinsic flux of the quasar; the Lyα forest scatters light at rest wavelength $\lambda_r < 1215$ Å beginning with Lyα opacity and eventually including the full Lyman series. Because of the low spectral resolution of these spectra, we cannot identify individual absorption lines and therefore observe the intrinsic quasar flux attenuated by a relatively smooth Lyman series opacity (see Section 5.1 for a full description). Therefore, our approach was to fit a template spectrum to the flux at $\lambda_r \approx 950$–1150 Å. We have found that the data are reasonably well described by the Telfer et al. (2002) radio-quiet quasar template spectrum f_λ^{Telfer} shifted to the observer frame and allowing for a scaled normalization C and power law tilt α, i.e.,

$$f_\lambda^{conti}(\lambda_r < 1200\,\text{Å}) = C\, f_\lambda^{Telfer} \left(\frac{\lambda_{obs}}{2500\,\text{Å}}\right)^\alpha. \quad (1)$$

We emphasize that even though the Telfer spectrum is intended to represent the mean intrinsic SED of $z \sim 1$ quasars, f_λ^{conti} represents the intrinsic flux of each of our quasars attenuated by Lyman series opacity. The values for C and α were determined using a custom, interactive GUI that allows one to visually compare a model continuum with each quasar spectrum. In general, the data at $\lambda_{rest} = 950$–1150 Å in the QSO rest-frame constrain the C and α parameters with reasonable confidence ($\approx 10\%$–20% uncertainty). The analysis on each quasar was done independently by J.M.O. and J.X.P. and we report our preferred models in Table 1. We then extrapolate this model to $\lambda_r < 950$ Å.

With f_λ^{conti} estimated as above, we proceeded to fit any significant and sudden drop in the flux below $\lambda_{rest} = 912$ Å as Lyman limit opacity. Specifically, we model the observed flux as the continuum flux described above modulated by one or more "systems" yielding appreciable Lyman limit opacity. Each system is characterized by a redshift z_{abs} and an optical depth at the Lyman limit $\tau_{912}^{LL} \approx N_{H\,I}/10^{17.19}\,\text{cm}^{-2}$. In the following, we refer to systems with $\tau_{912}^{LL} \geqslant 2$ as Lyman limit systems (LLSs) and systems with $\tau_{912}^{LL} < 2$ as partial Lyman limit systems (pLLSs[4]), although we occasionally use LLS to

refer to all systems exhibiting detectable Lyman limit opacity. The resulting model is

$$f_\lambda^{model} = f_\lambda^{conti} \exp\left[-\sum_i^N \tau_\lambda^{LL,i} \right] \quad (2)$$

where the sum is over all absorbers identified along the sightline ($z_{abs} \leqslant z_{em}$) and τ_λ is the opacity in the rest frame of the absorber (Verner et al. 1996).

In a minority of cases ($\sim 30\%$), the observed spectra are well described by one or zero Lyman limit systems. For the remainder of cases, however, the data are best, and very well, modeled with multiple LLS with τ_{912}^{LL} varying from 0.2 to 2. As with the continuum estimation, the modeling was performed by hand using a custom GUI that accounts for the spectral resolution of the *HST* data. We also experimented with χ^2-minimization algorithms, but these gave unrealistically small statistical errors ($\approx 1\%$–2%) owing to the high S/N of the spectra (and high reduced χ^2 values because the models did not include Lyα forest absorption). Indeed, the results are dominated by the systematic error of continuum placement and, to a lesser extent, line-blending by the IGM. For these reasons, we have proceed with a by-hand approach and estimate the uncertainties through inter-comparisons amongst multiple authors, and further with the results from a Monte Carlo analysis.

Each spectrum was modeled independently by J.M.O. and J.X.P. and then the authors compared these results and agreed, along with a third author, G.W., on a solution for cases in dispute. For the systems with $\tau_{912}^{LL} > 2$ listed in Table 3, the two authors had agreed in 35/39 cases there was a $\tau_{912}^{LL} > 2$ system within $\delta z = 0.05$ of the redshift listed in the table. Of the four disparate cases, most had $\tau_{912}^{LL} \approx 2$. In these cases, the redshifts have an rms of ≈ 0.01. For the systems in the table with $0.5 < \tau_{912}^{LL} < 2$, both authors agreed on a system within $\delta z = 0.05$ in 20/27 cases. The rms in the optical depths between the two sets of models is ≈ 0.05 and the rms in redshifts is ≈ 0.02.

To gauge our ability to successfully identify LLS absorption, we performed an analysis on 100 mock quasar sightlines. The sightlines were generated by drawing randomly from Monte Carlo absorption line lists, each created using the best-fit column density distribution function described in Section 6.4. Absorption lines were generated from these lists, convolved to the WFC3 resolution, and were placed on absorption-free QSO spectra with varying power law tilts and S/Ns chosen to

---

[4] We note the difference between pLLS as defined here, and PLLS, which is a "proximate" LLS, i.e., one within 3000 km s^{-1} of the QSO redshift.
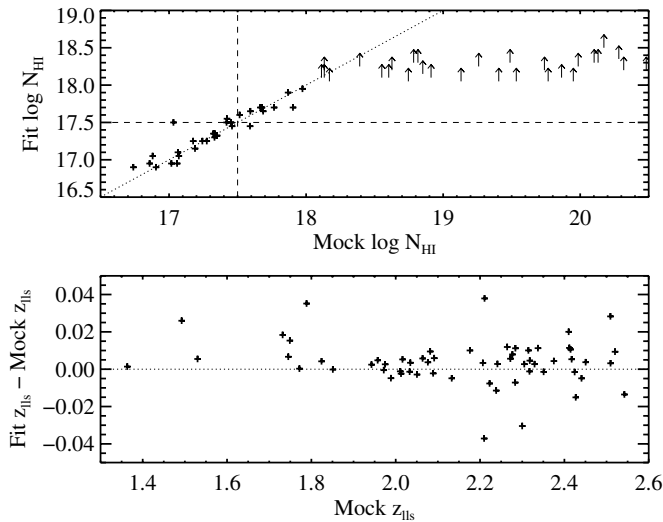
Figure 1. Comparisons between fit and input values for log $N_{\rm H\,I}$ (upper panel) and $z_{\rm LLS}$ (lower panel) for a mock sample of spectra designed to mimic the WFC3 data. The horizontal and vertical dashed lines in the upper panel correspond to $\tau_{912}^{\rm LL} = 2$. For most $\tau_{912}^{\rm LL} > 2$ LLS, we can only obtain a lower limit on log $N_{\rm H\,I}$ and denote those systems with arrows.

best mimic the data variety of our sample. The spectra were then surveyed by one author (J.M.O.) for LLS absorption using the same interface as with the real data. The results of this analysis are as follows: When we impose the survey definition criteria given in Section 4.1, the mock LLS spectra contain a total of 91 $\tau_{912}^{\rm LL} > 0.5$ absorbers in the survey path, with 72 systems having $\tau_{912}^{\rm LL} > 2$, 11 having $1 < \tau_{912}^{\rm LL} \leqslant 2$, and 8 with $0.5 < \tau_{912}^{\rm LL} \leqslant 1.0$. J.M.O. identified 76 systems having $\tau_{912}^{\rm LL} > 2$, 9 having $1 < \tau_{912}^{\rm LL} \leqslant 2$, and 10 with $0.5 < \tau_{912}^{\rm LL} \leqslant 1.0$. The primary nature of the discrepancy between the input mock LLS sample and those recovered dealt with systems very near the optical depth boundary of each bin. For example, in three of the four $\tau_{912}^{\rm LL} > 2$ discrepant cases, the input mock spectra had $17.4 < \log N_{\rm H\,I} \leqslant 17.5$, but were given a column density of either $\log N_{\rm H\,I} = 17.5$ or $\log N_{\rm H\,I} = 17.55$ Likewise, one of the two $1 < \tau_{912}^{\rm LL} \leqslant 2$ discrepancies and two of the three $0.5 < \tau_{912}^{\rm LL} \leqslant 1.0$ cases stemmed from the mock LLS lying within $\log N_{\rm H\,I} = 0.05$ of the boundary between bins in $\tau_{912}^{\rm LL}$. In one case, a single $\tau_{912}^{\rm LL} > 2$ system was used to describe two mock LLS with $\tau_{912}^{\rm LL} > 1$ which lied within $\delta z = 0.1$ of each other. In only a single case was a completely incorrect system used to model the input mock spectrum, where a spurious $\tau_{912}^{\rm LL} \sim 1$ system was included. Although not included in any of our statistical analyses below, >50% of all $0.2 < \tau_{912}^{\rm LL} < 0.5$ absorption was correctly identified, confirming our ability to be sensitive to such absorption.

Figure 1 gives a further exploration of the range of uncertainties in our data. In the upper panel, we show the estimates of log $N_{\rm H\,I}$ in LLS within the range log $N_{\rm H\,I} > 16.9$ derived from fits to the mock spectra compared to their input values. We choose this range to fully explore the range of values for which we can make more precise statements about $N_{\rm H\,I}$, namely the statistical survey range $0.5 < \tau_{912}^{\rm LL} < 2.0$ with additional measurements at higher optical depths when the data allows for an $N_{\rm H\,I}$ to be determined in the cases where we can observe the recovery in flux below the Lyman limit (although we note that all $\tau_{912}^{\rm LL} \geqslant 2$ absorption is lumped into a single bin for our statistical analysis). We find overall good agreement between the fit values

Table 2
LLS Models

Quasar	$z_{\rm abs}$	$N_{\rm H\,I}$
Quasars Observed with WFC3/UVIS-G280		
J075158.65+424522.9	2.380	16.50
	1.654	17.10
	1.545	17.35
J075547.83+220450.1	2.238	16.10
	2.024	17.25
	1.640	16.80
J080620.47+504124.4	1.840	16.95
	1.658	17.15
	1.343	16.80
	1.080	17.05
J083326.82+081552.0	1.911	16.40
Quasars Observed with ACS/PR200L		
J010657.94−085500.1	2.149	16.40
	1.947	18.10
J023359.71+004938.5	2.066	16.60
	1.393	16.35
J034024.57−051909.2	2.065	18.15
J040241.42−064137.9	2.160	17.10
	1.495	16.85
	1.778	16.65

(This table is available in its entirety in a machine-readable form in the online journal. A portion is shown here for guidance regarding its form and content.)

and the input mock values for $N_{\rm H\,I}$ over this range with a mean difference between fit and input of -0.02 and $\sigma = 0.12$. In the lower panel of Figure 1, we explore our ability to properly determine the redshift of the LLS for the $\tau_{912}^{\rm LL} > 0.5$ LLS. We find a mean difference between fit and input $z_{\rm lls}$ of -0.002 and $\sigma = 0.014$, again a good agreement.

These comparisons provide an estimate of the systematic uncertainty related to the LLS modeling. In addition, we estimate the systematic uncertainties of continuum uncertainty and system blending to be 1% ($\approx 1000\,{\rm km\,s^{-1}}$) for the redshift estimation and $\approx 15\%$ for the optical depth measurements.[5] Figures 2 and 3 present the spectra and adopted models for WFC3/UVIS-G280 and ACS/PR200L, respectively, and Table 2 tabulates the results.

4. THE STATISTICS OF LLS AT $z \approx 2$

4.1. Survey Definition

From the spectral analysis of the previous section, it is relatively straightforward to perform a statistical analysis of Lyman limit absorption. A fundamental description of IGM absorption systems is the $N_{\rm H\,I}$ frequency distribution, $f(N_{\rm H\,I}, X)$. Akin to a luminosity function, $f(N_{\rm H\,I}, X)$ gives the number of absorbers with column density $N_{\rm H\,I}$ per $dN_{\rm H\,I}$ interval and per path length dX, where

$$dX = \frac{H_0}{H(z)}(1+z)^2 dz. \qquad (3)$$

The absorption path length was introduced to yield a constant $f(N_{\rm H\,I}, X)$ for systems that arise from discrete absorbers (e.g., galaxies) with a constant product of comoving number density and physical size (Bahcall & Peebles 1969). Standard practice

---

[5] All models assume $b = 25\,{\rm km\,s^{-1}}$; this has no bearing on our results given the low spectral resolution.
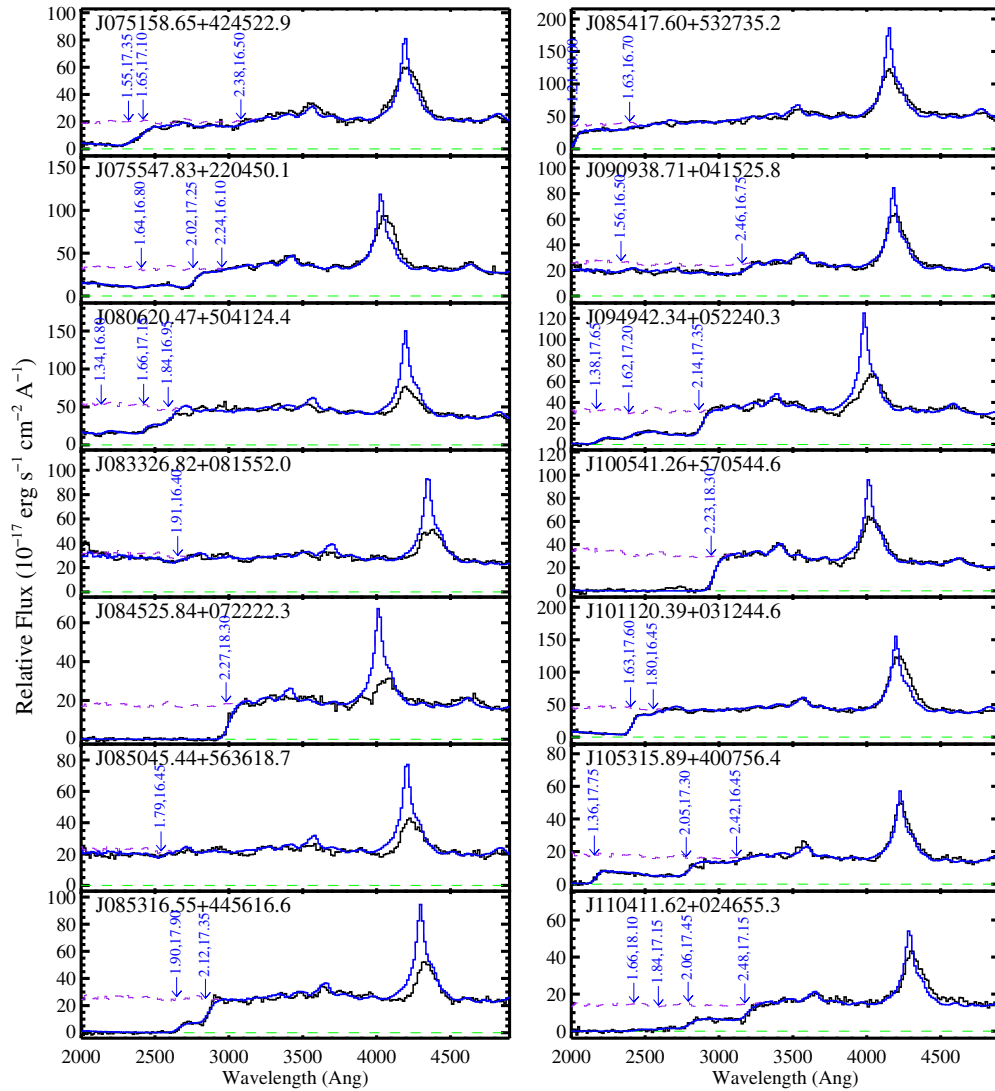
Figure 2. WFC3/UVIS-G280 quasar spectra (black histogram) and the models (blue solid line) we have generated to assess Lyman limit absorption along the sightlines. The arrows mark the redshift and $N_{\rm H\,I}$ values for each modeled LLS. The dashed purple line traces our estimate of the continuum without LL absorption but includes Lyman series opacity.

(A color version of this figure is available in the online journal.)

is to survey quasars for absorbers as a function of H I column density and estimate $f(N_{\rm H\,I}, X)$ from simple counting statistics.

Owing to uncertainties in the continuum placement and limitations in S/N limit, analysis of our quasar spectra has a limiting sensitivity to Lyman limit absorption of $\tau_{912}^{\rm LL} \gtrsim 0.2$ or $N_{\rm H\,I} \gtrsim 10^{16.5}$ cm^{-2}. However, as explained below, we only include those systems with $\tau_{912}^{\rm LL} > 0.5$ in our statistical exploration of incidence frequency and column density distribution. Furthermore, it is impossible to yield any estimate of $\tau_{912}^{\rm LL}$ beyond a lower limit for systems with $\tau_{912}^{\rm LL} > 4$ because all such systems have zero measurable flux below the Lyman limit. Although we can use the recovery in flux below the Lyman limit to obtain $N_{\rm H\,I}$ for LLS with $2 < \tau_{912}^{\rm LL} < 4$, such cases require significant spectral coverage which is not always available in our data. As a result, our statistical sample will consider all systems with $\tau_{912}^{\rm LL} > 2$ together as a single population.[6] In short, the analysis has sensitivity to $\tau_{912}^{\rm LL}$ over approximately one or-

der of magnitude and many systems only yield a lower limit to $\tau_{912}^{\rm LL}$. Therefore, one may estimate $f(N_{\rm H\,I}, X)$ directly in only a narrow range of H I column densities. For these reasons, studies of Lyman limit absorption have provided rather limited direct constraints on $f(N_{\rm H\,I}, X)$.

Instead, researchers have focused primarily on the zeroth moment of $f(N_{\rm H\,I}, X)$, i.e., the incidence of Lyman limit absorption per unit path length

$$\ell(X)_{\tau \geqslant \tau_{\rm limit}} = \int_{N_{\rm H\,I,limit}}^{\infty} f(N_{\rm H\,I}, X) \, dN_{\rm H\,I} \qquad (4)$$

or per unit redshift[7] $\ell(z)$. The incidence of Lyman limit systems is measured from a limiting optical depth $\tau_{\rm limit}$ corresponding to a limiting H I column density $N_{\rm H\,I,limit}$, generally set by the spectral quality.

In principle, the $\ell(z)$ quantity is a direct observable. Standard practice is to estimate it from the ratio of the number of systems

---

[6] One can improve the estimate for $N_{\rm H\,I}$ from the Lyman series, e.g., the damping wings of Lyα, but our spectral resolution precludes such analysis.
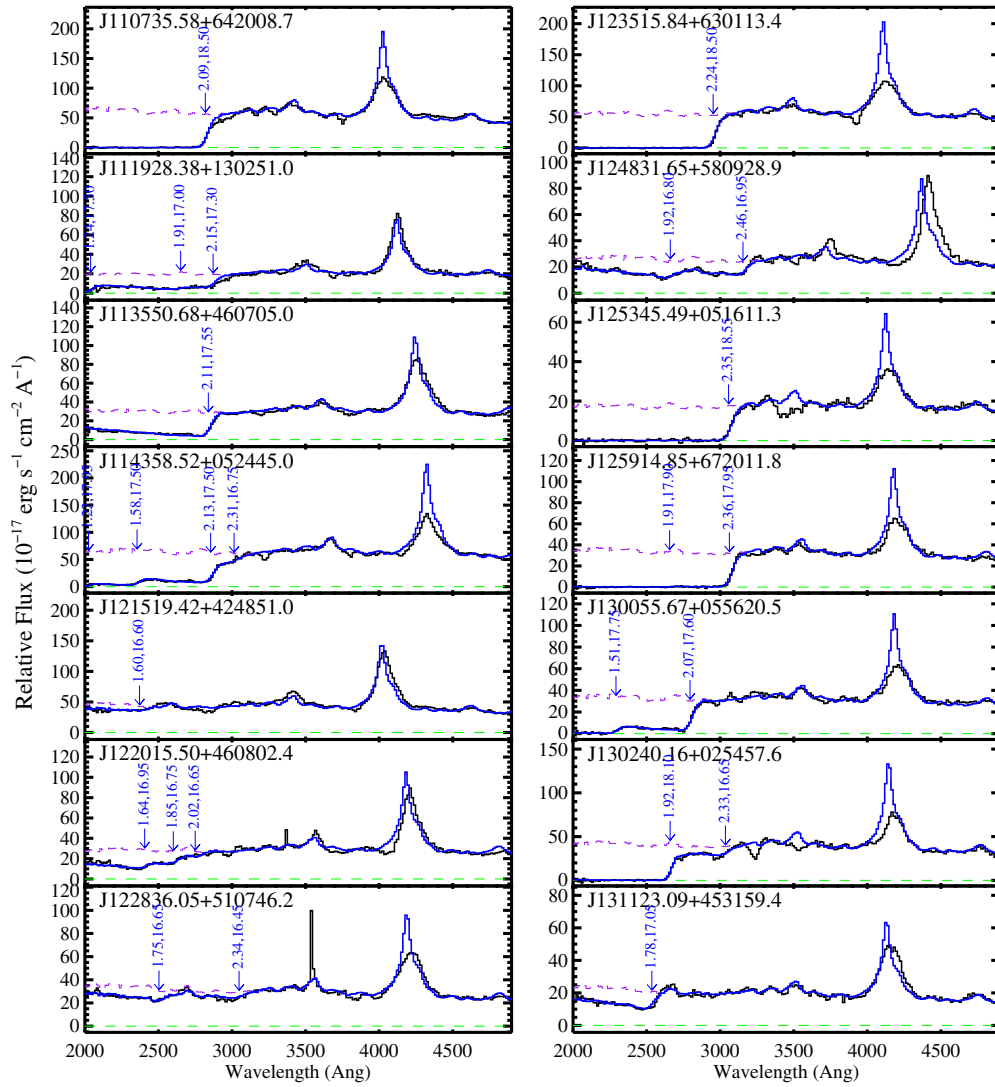
[7] Also commonly referred to as $d\mathcal{N}/dX$ and $d\mathcal{N}/dz$.

Figure 2. (Continued)

detected within a redshift interval $\mathcal{N}_{\mathrm{LLS}}$ to the total redshift path surveyed Δz:

$$\ell(z) = \frac{\mathcal{N}_{\mathrm{LLS}}}{\Delta z}. \qquad (5)$$

Observationally, there are several factors that complicate such an LLS survey (see, e.g., Appendix C in Tytler 1987). First, it is very challenging to successfully identify multiple LLSs that have small separations in redshift space. One is limited by the spectral resolution, the S/N of the data, the precise characteristics of the systems, and the density of the Lyα forest at the wavelengths of interest. For our data, we cannot resolve two LLS located within $|\delta v| < 10{,}000\ \mathrm{km\ s^{-1}}$ ($\delta z \approx 0.1$) and therefore consider all such complexes as a single LLS with a summed optical depth. Second, the presence of a partial LLS reduces the quasar flux and the resultant spectral S/N but may not prohibit the search for an additional LLS. As described in detail in POW10, one must establish a strict and proper criterion for the survey path or the results will suffer from a "pLLS bias."

To this end, we establish these criteria for the survey:

1. The ending redshift z_{end} is set to be $3000\ \mathrm{km\ s^{-1}}$ blueward of the quasar emission redshift. This is established in part to account for the relatively large uncertainty in quasar

redshifts and also to minimize any biases from gas in the environment including the quasar.

2. If there are no LLS detected, the starting redshift $z_{\mathrm{start}} = (2200\ \text{Å}/911.7641\ \text{Å}) - 1 = 1.4$ for the WFC3 data and $z_{\mathrm{start}} = 1.2$ for the ACS data. This provides enough spectral coverage (≈ 200 Å) to confidently identify an LLS system before the spectra deteriorate in quality.

3. For the WFC3 sample, identification of an LLS with $\tau_{912}^{\mathrm{LL}} \geqslant 0.5$ and $z = z_{\mathrm{abs}}$ precludes the search for any LLS with $z < z_{\mathrm{abs}}$ and $\tau_{912}^{\mathrm{LL}} \leqslant 1$.

4. For he WFC3 sample, identification of an LLS with $\tau_{912}^{\mathrm{LL}} \geqslant 1$ and $z = z_{\mathrm{abs}}$ precludes the search for any LLS with $z < z_{\mathrm{abs}}$ and $\tau_{912}^{\mathrm{LL}} < 2$.

5. In both samples, identification of an LLS with $\tau_{912}^{\mathrm{LL}} \geqslant 2$ and $z = z_{\mathrm{abs}}$ precludes the search for any other LLS with $z < z_{\mathrm{abs}}$. Because of potential sky subtraction complications (see Paper I), we have only performed a survey for $\tau_{912}^{\mathrm{LL}} \geqslant 2$ LLS in the ACS/PR200L spectra.

Together, the final four criteria establish z_{start} values for a range of limiting optical depth.

With these survey criteria, it is straightforward to evaluate the survey path of our dataset. This is described in Figure 4, which
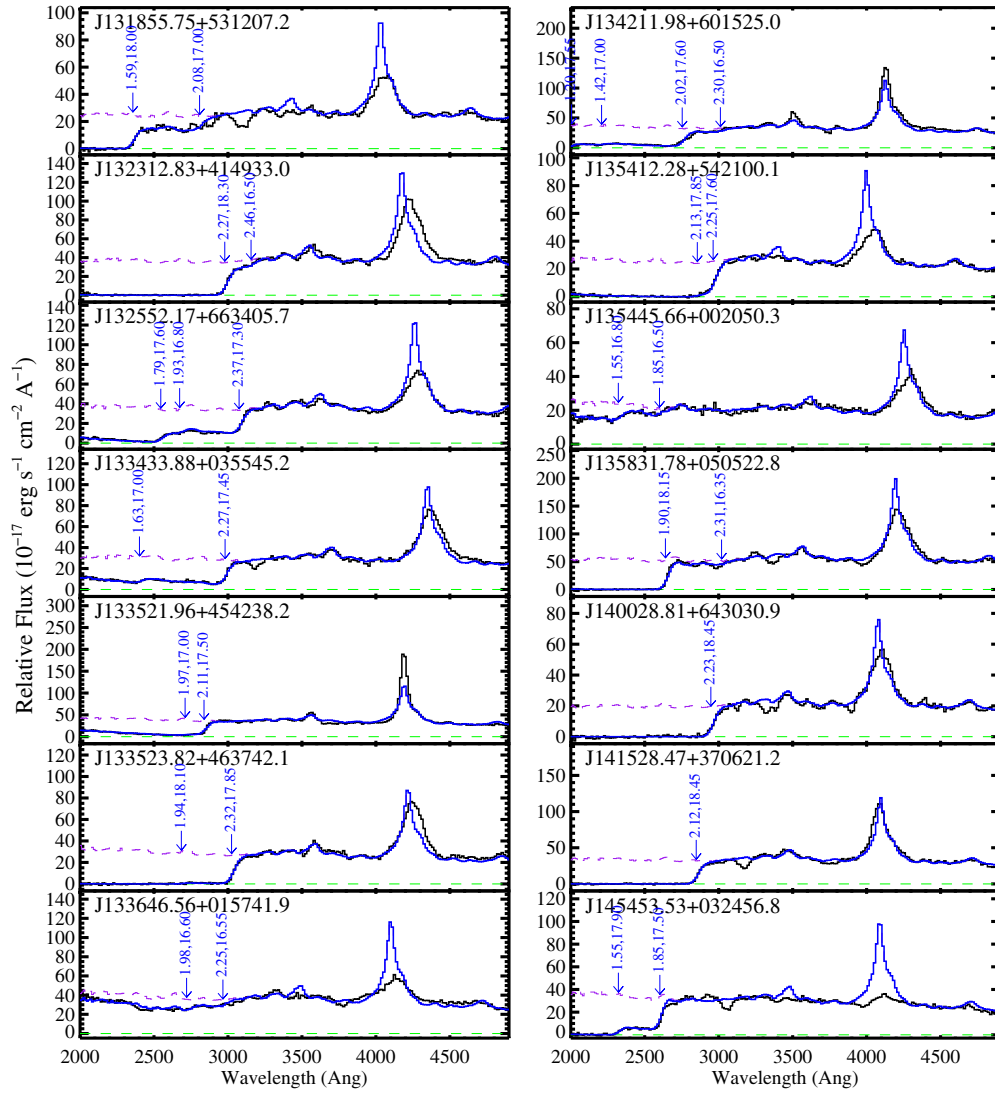
Figure 2. (Continued)

presents the so-called sensitivity function $g(z)$ for the survey, i.e., the number of unique quasar spectra at a given redshift where one can search for an LLS to a given optical depth limit. The survey path is similarly summarized in Tables 3 and 4 where we list the starting and ending redshift for the LLS survey of each QSO. We note that the sensitivity function is comparable to that from Ribaudo et al. (2011) at the low ($z \sim 1.5$) redshift end of our sample, increasing to nearly twice their value at higher redshifts, making the two samples highly complementary. None of the quasars that they surveyed are in our sample.

4.1.1. Results

One may now simply evaluate Equation (5) to derive estimates for the incidence of LLS absorption at $z < 2$, as a function of limiting optical depth. Figure 5 presents the results for the WFC3/UVIS-G280 survey for $\tau_{912}^{\rm LL} \geqslant 0.5$, 1 and 2, and for the ACS/PR200L survey for $\tau_{912}^{\rm LL} \geqslant 2$ LLS. We present the results for two redshift intervals, $z = [1.2, 2.0)$ and $[2.0, 2.6)$. As one predicts for an expanding universe, we observe a decreasing incidence between the two redshift bins for all samples. Overlaid on Figure 5 are the results from Songaila & Cowie (2010) for $\tau_{912}^{\rm LL} \geqslant 1$ determined over the redshift range $0 < z < 6$. Our

results are consistent with theirs and those of Ribaudo et al. (2011), but we note that our survey provides better sensitivity for the epochs $1.5 < z < 2.5$.

Equation (3), along with the transformation

$$\ell(X)dX = \ell(z)dz \qquad (6)$$

and the cosmological evolution of the Hubble constant

$$H(z) = H_0[\Omega_\Lambda + \Omega_m(1+z)^3]^{1/2} \qquad (7)$$

allows for the determination of $\ell(X)$ from our sample. We use the same bins in redshift and sub-sampling in $\tau_{912}^{\rm LL}$ as for $\ell(z)$. The results for $\ell(X)$ are shown in Figure 6. Also shown in Figure 6 is the single power law fit for $\tau_{912}^{\rm LL} \geqslant 2$ LLS from Ribaudo et al. (2011) which combines their analysis of $z < 2.5$ *HST* spectra and the $z > 3.5$ SDSS results from POW10. Our results generally agree with those of Ribaudo et al. (2011), namely that at redshifts $z < 2$, $\ell(X)$ evolves only very weakly (in fact, the WFC3/UVIS-G280 results are more consistent with no evolution), transitioning to a sharper evolution with z at $z > 2$. We further concur with their observation that the $2.5 < z < 3.5$ span must be fully explored to best understand this transition
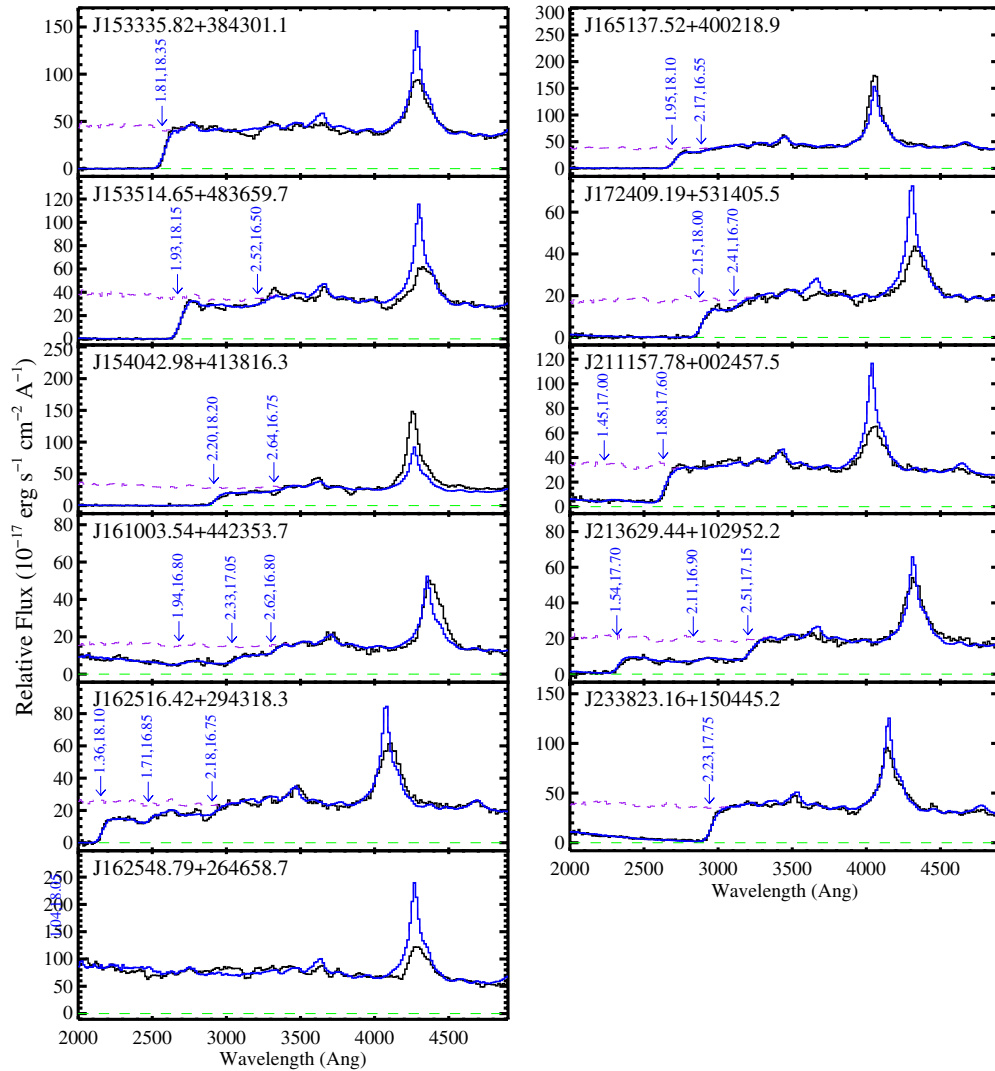
Figure 2. (Continued)

in the evolution of $\ell(X)$. Additionally, Ribaudo et al. (2011) use their results to constrain the differential column density distribution, $f(N_{H I}, X)$. We address this quantity below, using the additional information gained from an analysis of stacked spectra.

We now place our results for $\ell(X)$ from WFC3/UVIS-G280 alongside those obtained from the super Lyman limit system (SLLS; O'Meara et al. 2007) and the DLA (Prochaska & Wolfe 2009) in Figure 7. Quantitatively, we find that the SLLSs and DLAs (i.e., systems with $N_{H I} \geqslant 10^{19}$ cm^{-2}) contribute a significant fraction of $\ell(X)_{\tau \geqslant 2}$. By inference, this implies that there are relatively few LLS with $N_{H I} = 10^{17.5}$–10^{19} cm^{-2} and therefore that $f(N_{H I}, X)$ is shallow at these column densities. We return to this issue in Section 6.1. We also note with interest the relative contributions to $\ell(X)$ that each bracket in τ_{912}^{LL} makes. Specifically, we see that the integral contribution to $\ell(X)$ of the LLS with $0.5 < \tau_{912}^{LL} < 2$ is nearly equal in magnitude to that for the LLS with $\tau_{912}^{LL} > 2$. As $\ell(X)$ corresponds to the integral of $f(N_{H I}, X)$ over $N_{H I}$, this implies a pronounced change in shape in $f(N_{H I}, X)$ for $\tau_{912}^{LL} < 2$. We explore this result in greater detail in Section 6.2. Finally, we combine our results for $\tau_{912}^{LL} > 2$ for ACS/PR200L, WFC3/UVIS-G280, and the results from the archival study of Ribaudo et al. (2011). The weighted

mean for these results at $z \sim [2, 2.5]$ is $\ell(X)_{\tau \geqslant 2} = 0.29 \pm 0.05$. We adopt this measurement in all analysis that follows. Table 5 summarizes all of these results.

4.2. Systematic Errors in the Incidence Frequency

To assess the effects of uncertainty in the $N_{H I}$ and z_{abs} values for the LLS, we performed a Monte Carlo analysis where we randomly modified each system with a normal deviate and assuming $\sigma_{N_{H I}} = 0.05$ dex and $\sigma_z = 0.02$ (see Section 3). We then recalculated $\ell(z)$ 1000 times for each redshift bin. We find that none of the trials have an $\ell(z)$ value that lies outside the 85% confidence level given by Poisson uncertainty. Furthermore, we explored the effects of proximity to the quasar by varying our upper wavelength cut. This simultaneously addresses issues associated either with inaccurate quasar emission redshifts, z_{qso}, or with the possibility that quasars arise in overdense regions, which might effect our statistics. To do so, we expanded the proximity region from 3000 km s^{-1} blueward of the quasar emission redshift to 10,000 km s^{-1}, and find our results to be essentially unchanged.

In Prochaska et al. (2010) we identified and described at length a systematic bias to LLS surveys associated with pLLS. This bias occurs when one truncates the search path for an

Table 3
WFC3/UVIS-G280 LLS Statistical Survey

| Quasar	z_{em}	$z_{start}^{\tau>2}$	$z_{start}^{\tau>1}$	$z_{start}^{\tau>0.5}$	z_{LLS}	$\log N_{H\,I}$
J075158.65+424522.9	2.453	1.576	1.576	1.576	1.576	17.60
J075547.83+220450.1	2.319	1.400	2.026	2.026	2.026	17.30
J080620.47+504124.4	2.457	1.400	1.400	1.840	1.840	16.95
J083326.82+081552.0	2.581	1.400	1.400	1.400	. . .	. . .
J084525.84+072222.3	2.307	2.275	2.275	2.275	2.275	18.45
J085045.44+563618.7	2.464	1.400	1.400	1.400	. . .	. . .
J085316.55+445616.6	2.540	1.903	2.117	2.117	1.903	17.90
					2.117	17.35
J085417.60+532735.2	2.418	1.400	1.400	1.400	. . .	. . .
J090938.71+041525.8	2.444	1.400	1.400	1.400	. . .	. . .
J094942.34+052240.3	2.282	1.400	2.141	2.141	2.141	17.35
J100541.26+570544.6	2.308	2.239	2.239	2.239	2.239	17.75
J101120.39+031244.6	2.458	1.634	1.634	1.634	1.634	17.60
J105315.89+400756.4	2.482	1.400	2.050	2.050	2.050	17.35
J110411.62+024655.3	2.532	1.613	2.062	2.495	1.613	18.15
					2.062	17.40
					2.495	17.15
J110735.58+642008.7	2.316	2.093	2.093	2.093	2.093	18.15
J111928.38+130251.0	2.394	1.400	2.149	2.149	2.149	17.30
J113550.68+460705.0	2.496	2.114	2.114	2.114	2.114	17.55
J114358.52+052445.0	2.561	2.139	2.139	2.139	2.139	17.50
J121519.42+424851.0	2.310	1.400	1.400	1.400	. . .	. . .
J122015.50+460802.4	2.446	1.400	1.400	1.891	1.891	16.95
J122836.05+510746.2	2.450	1.400	1.400	1.400	. . .	. . .
J123515.84+630113.4	2.383	2.238	2.238	2.238	2.238	18.50
J124831.65+580928.9	2.599	1.400	1.400	2.487	2.487	16.95
J125345.49+051611.3	2.398	2.353	2.353	2.353	2.353	18.55
J125914.85+672011.8	2.443	2.359	2.359	2.359	2.359	17.95
J130055.67+055620.5	2.446	2.058	2.058	2.058	2.058	17.60
J130240.16+025457.6	2.414	1.917	1.917	1.917	1.917	18.10
J131123.09+453159.4	2.403	1.400	1.400	1.809	1.809	17.05
J131855.75+531207.2	2.321	1.585	1.585	2.080	1.585	18.00
					2.080	17.00
J132312.83+414933.0	2.440	2.267	2.267	2.267	2.267	18.30
J132552.17+663405.7	2.511	1.792	2.373	2.373	1.792	17.60
					2.373	17.30
J133433.88+035545.2	2.583	1.400	2.269	2.269	2.269	17.45
J133521.96+454238.2	2.452	2.110	2.110	2.110	2.110	17.65
J133523.82+463742.1	2.474	2.327	2.327	2.327	2.327	17.80
J133646.56+015741.9	2.379	1.400	1.400	1.400	. . .	. . .
J134211.98+601525.0	2.399	1.995	1.995	1.995	1.995	17.60
J135412.28+542100.1	2.294	2.249	2.249	2.249	2.249	17.60
J135445.66+002050.3	2.504	1.400	1.400	1.400	. . .	. . .
J135831.78+050522.8	2.455	1.895	1.895	1.895	1.895	18.15
J140028.81+643030.9	2.359	2.232	2.232	2.232	2.232	18.45
J141528.47+370621.2	2.374	2.124	2.124	2.124	2.124	18.45
J145453.53+032456.8	2.368	1.861	1.861	1.861	1.861	17.50
J153335.82+384301.1	2.529	1.815	1.815	1.815	1.815	18.35
J153514.65+483659.7	2.542	1.929	1.929	1.929	1.929	18.15
J154042.98+413816.3	2.516	2.186	2.186	2.186	2.186	18.50
J161003.54+442353.7	2.588	1.400	1.400	2.331	2.331	17.05
J162516.42+294318.3	2.357	1.400	1.400	1.400	. . .	. . .
J162548.79+264658.7	2.518	1.400	1.400	1.400	. . .	. . .
J165137.52+400218.9	2.343	1.949	1.949	1.949	1.949	18.10
J172409.19+531405.5	2.547	2.149	2.149	2.149	2.149	18.00
J211157.78+002457.5	2.325	1.884	1.884	1.884	1.884	17.60
J213629.44+102952.2	2.555	1.555	1.555	2.500	1.555	17.60
					2.500	17.15
J233823.16+150445.2	2.419	2.226	2.226	2.226	2.226	17.75
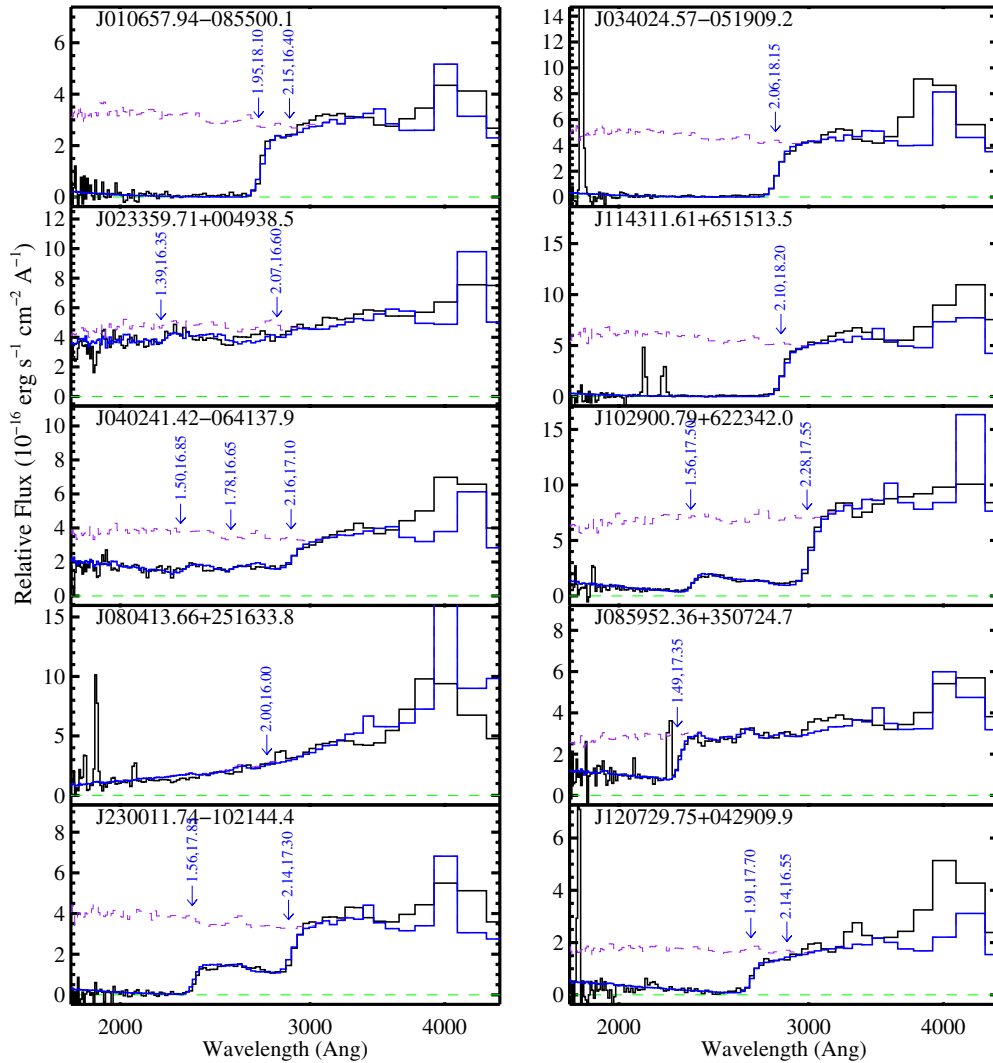
Figure 3. Same as for Figure 2 but for the ACS/PR200L observations. Note that the *x*-axis has a logarithmic scaling.
(A color version of this figure is available in the online journal.)

LLS owing to the presence of one or more pLLS, as we have done in this paper for systems with $\tau_{912}^{LL} < 2$. It is possible, therefore, that we have over-estimated the incidence of systems with $\tau_{912}^{LL} \approx 1$. The pLLS bias, however, is proportional to the incidence of Lyman limit absorption which at these redshifts is small. Indeed, we estimate that this is a <10% effect and therefore within the statistical error associated with our small sample size.

The other, and unavoidable, bias described by Prochaska et al. (2010) is related to the blending of Lyman limit systems. One or more systems localized to $\delta z \sim 0.1$ will be unresolved by our spectral resolution and therefore treated as a single LLS. This raises the incidence of $\tau_{912}^{LL} > 2$ systems at the expense of pLLS. Again, this bias is proportional to the overall incidence of LLS and at these redshifts the effects will be small (<10%; Figure 7 of Prochaska et al. 2010).

5. STACKED SPECTRUM ANALYSIS

In this section we generate an average quasar spectrum from the WFC3/UVIS-G280 spectra and then analyze this dataset to estimate the mean free path to ionizing radiation λ_{mfp}^{912}, following PWO09. We begin with a review and expansion of their formalism.

5.1. Formalism

In PWO09 we introduced a new technique for constraining the mean free path to ionizing radiation, λ_{mfp}^{912}. The approach analyzes a "stacked" quasar spectrum, constructed from a strict average of a cohort of quasars with common emission redshift, at wavelengths blueward of the Lyman limit. This stacked spectrum, by definition, yields the average observed flux $\bar{f}_\lambda^{obs}$ of quasars at a given redshift. For wavelengths redward of Lyα, the flux is dominated by the SED of quasars, with only a minor attenuation from the average metal-line absorption of gas in the IGM, $\tau_{eff}^{metals}(z)$. Blueward of Lyα, e.g., at ≈ 1125 Å, the observed flux $\bar{f}_{1125}^{obs}$ is the product of the average intrinsic quasar SED $\bar{f}_{1125}^{SED}$ and the average absorption from the Lyα forest[8] $\exp(-\tau_{eff}^{Ly\alpha})$ at the redshift $z_{Ly\alpha} = 1125$ Å $(1 + z_{em})/1215.67$ Å $- 1$,

$$\bar{f}_{1125}^{obs}(z_{em}) = \bar{f}_{1125}^{SED} \exp\left[-\tau_{eff}^{Ly\alpha}(z_{Ly\alpha})\right]. \qquad (8)$$

As one progresses to shorter wavelengths (lower $z_{Ly\alpha}$), $\tau_{eff}^{Ly\alpha}$ is observed to decrease because the incidence of Lyα lines

---

[8] Observationally, it is common practice to assess $\tau_{eff}^{Ly\alpha}$ to a limiting H I column density, e.g., to exclude DLAs or even LLSs.
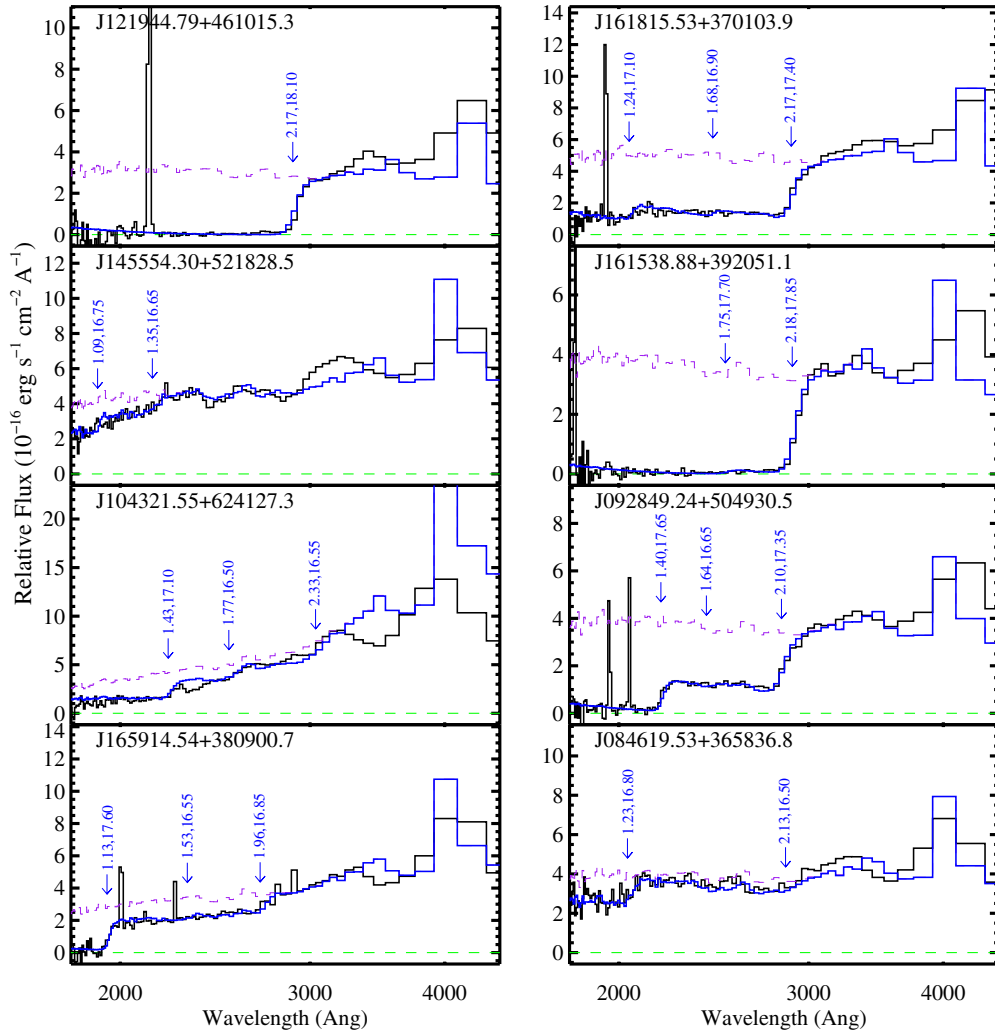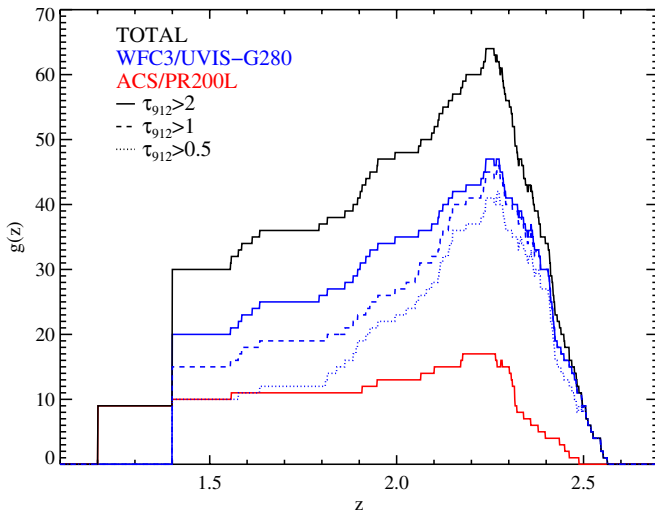
Figure 3. (Continued)

Figure 4. These $g(z)$ curves describe the survey size as a function of redshift. Specifically, $g(z)$ expresses the number of quasars at a given z that were surveyed for LLS absorption to a limiting optical depth at $\lambda_r = 912$ Å. They decrease with decreasing redshift because the presence of an LLS along a sightline often precludes the search for additional LLSs. The solid black curve shows the combined $g(z)$ functions for the *HST*/ACS and WFC3/UVIS-G280 datasets for $\tau_{912} \geqslant 2$.

(A color version of this figure is available in the online journal.)
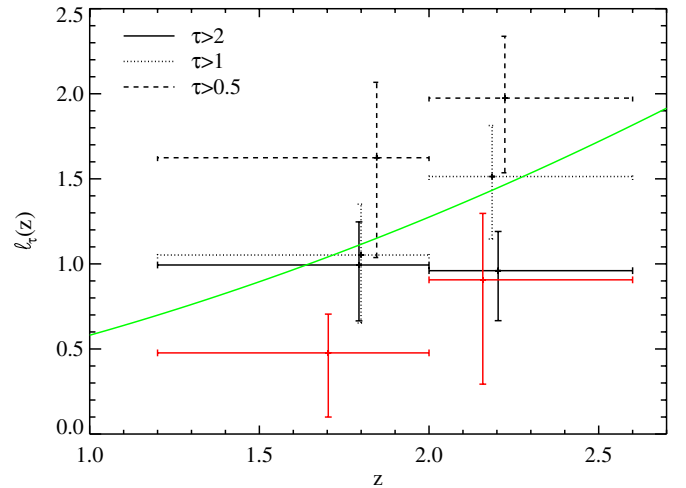
Figure 5. Incidence of LLSs per unit redshift $\ell(z)$, as estimated from our *HST* datasets. The WFC3/UVIS-G2803 data (black points) are shown for three limiting optical depths $\tau_{\rm limit}$. The red (solid) points are for the ACS/PR200L sample and $\tau_{\rm limit} \geqslant 2$. For each limiting optical depth, the data suggest only a modest (if any) evolution in $\ell(z)$ with redshift. The solid green line represents the fit by Songaila & Cowie (2010) for $\tau_{912}^{\rm LL} \geqslant 1$.

(A color version of this figure is available in the online journal.)
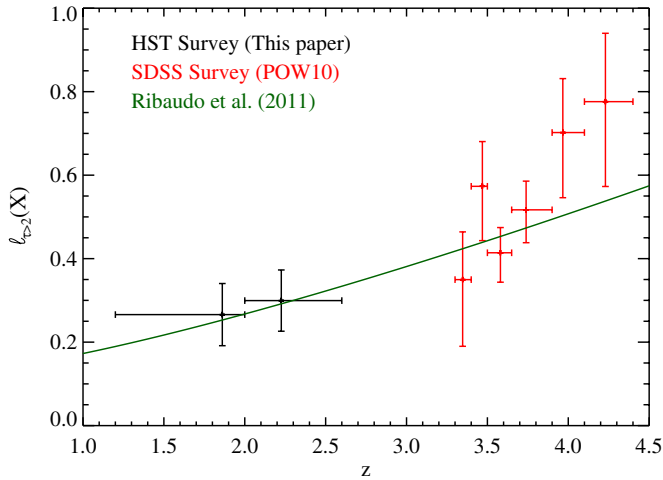
Figure 6. Incidence of LLSs per unit path length $\ell(X)$ restricted to $\tau_{\mathrm{limit}} > 2$, as estimated from our combined WFC3/UVIS-G280 and *HST*/ACS surveys. Shown in solid green is the $\ell(X)$ curve (converted to the cosmology adopted in this paper) of Ribaudo et al. (2011) derived from a single power law fit to archival analysis of lower z *HST* data and high z observations (Prochaska et al. 2010; Songaila & Cowie 2010). Their results are in good agreement with our estimates at $z < 2.5$ and together the data indicate mild evolution in $\ell(X)$ at low z.

(A color version of this figure is available in the online journal.)
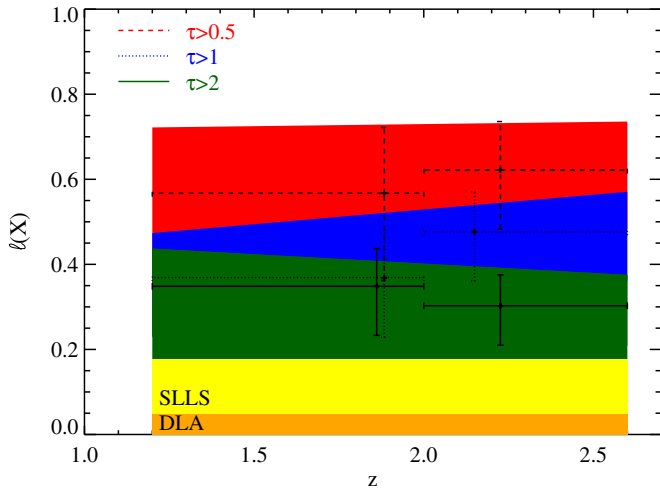
Figure 7. The points (and error bars) show the incidence per unit absorption length $\ell(X)$ for LLSs with limiting optical depths $\tau_{\mathrm{limit}} = 0.5$–2, for the WFC3/UVIS-G280 sample only. The red, blue, and green shaded regions express these same quantities. The orange shaded region shows an estimate for the incidence of DLAs taken from Prochaska & Wolfe (2009). Similarly, the yellow shaded region gives the contribution of super Lyman limit systems (SLLSs) to $\ell(X)$ (O'Meara et al. 2007). Together, systems with $N_{\mathrm{H\,I}} > 10^{19}\,\mathrm{cm}^{-2}$ have $\ell(X) \approx 0.18$, implying a contribution of 50%–80% to $\ell(X)_{\tau \geqslant 2}$.

(A color version of this figure is available in the online journal.)

decreases (e.g., Rauch 1998). However, one eventually incurs additional opacity from Lyβ from gas at redshift $z_{\mathrm{Ly}\beta} = \lambda/1025.72\,\text{Å} - 1$, and then Ly$\gamma$ opacity, and eventually the full Lyman series,

$$\tau_{\mathrm{eff}}^{\mathrm{Lyman}}(z_{\mathrm{em}}, \lambda) = \sum_{n=2}^{\infty} \tau_{\mathrm{eff}}^n(z_n), \tag{9}$$

with $z_n = \lambda(1 + z_{\mathrm{em}})/\lambda_n - 1$ and $n = 2, 3, 4, \ldots$ corresponding to Lyα, Lyβ, Lyγ, etc (e.g., Madau et al. 1996).

Table 4
ACS/PR200L LLS Statistical Survey

Quasar	z_{em}	$z_{\mathrm{start}}^{\tau>2}$	z_{LLS}	$N_{\mathrm{H\,I}}$
J010657.94−085500.1	2.350	1.947	1.947	18.10
J023359.71+004938.5	2.522	1.200	...	...
J034024.57−051909.2	2.340	2.065	2.065	18.15
J040241.42−064137.9	2.432	1.200	...	...
J080413.66+251633.8	2.302	1.200	...	...
J084619.53+365836.8	2.335	1.200	...	...
J085952.36+350724.7	2.373	1.200	...	...
J092849.24+504930.5	2.349	1.400	1.400	17.65
J102900.79+622342.0	2.470	2.279	2.279	17.55
J104321.55+624127.3	2.355	1.200	...	...
J114311.61+651513.5	2.392	2.101	2.101	18.20
J120729.75+042909.9	2.413	1.908	1.908	17.70
J121944.79+461015.3	2.484	2.171	2.171	18.10
J145554.30+521828.5	2.348	1.200	...	...
J161538.88+392051.1	2.315	2.177	2.177	17.85
J161815.53+370103.9	2.496	1.200	...	...
J165914.54+380900.7	2.343	1.200	...	...
J230011.74−102144.4	2.297	1.558	1.558	17.85

At $\lambda_r < 912$ Å, the emitted photons also experience the continuum opacity of Lyman limit absorption $\tau_{\mathrm{eff}}^{\mathrm{LL}}(z_{\mathrm{em}}, z_{912})$ with

$$z_{912} \equiv \frac{\lambda}{\lambda_{912}}(1 + z_{\mathrm{em}}) - 1. \tag{10}$$

This quantity is related to the mean free path $\lambda_{\mathrm{mfp}}^{912}$, defined to be the distance that a packet of photons travels before suffering an e^{-1} attenuation (on average). Specifically, we define $\lambda_{\mathrm{mfp}}^{912}$ to be the *physical* distance from z_{em} to the redshift z_{912}^{mfp} where $\tau_{\mathrm{eff}}^{\mathrm{LL}}(z_{912}^{\mathrm{mfp}}, z_{\mathrm{em}}) = 1$. Note that with this definition, $\lambda_{\mathrm{mfp}}^{912}$ applies to photons with energies greater than 1 ryd at z_{em}. The mean free path to ionizing photons establishes the mean intensity of the extragalactic UV background (EUVB; Haardt & Madau 1996; Meiksin 2009) and, in essence, defines the epoch of hydrogen reionization (i.e., $\lambda_{\mathrm{mfp}}^{912}$ has negligible value in a neutral universe).

Estimations of $\tau_{\mathrm{eff}}^{\mathrm{LL}}$ (and thereby $\lambda_{\mathrm{mfp}}^{912}$) have been made previously by integrating evaluations of the H I frequency distribution $f(N_{\mathrm{H\,I}}, z)$ of absorption systems in the IGM (e.g., Madau et al. 1999; Faucher-Giguère et al. 2008a):

$$\tau_{\mathrm{eff}}^{\mathrm{LL}}(z_{912}, z_{\mathrm{em}}) = \int_{z_{912}}^{z_{\mathrm{em}}} \int_0^\infty f(N_{\mathrm{H\,I}}, z') \\ \times \{1 - \exp[-N_{\mathrm{H\,I}}\sigma_{\mathrm{ph}}(z')]\}dN_{\mathrm{H\,I}}dz' \tag{11}$$

where σ_{ph} is the photoionization cross-section evaluated at the photon frequency. This approach is fraught with great uncertainty because: (1) the frequency of absorbers with roughly unit optical depth at the Lyman limit $\tau_{912}^{\mathrm{LL}} \lesssim 1$ is very difficult to ascertain; and (2) the incidence of optically thick absorbers ($\tau_{912}^{\mathrm{LL}} > 2$) suffers from significant systematic uncertainty (POW10).

In PWO09 we defined a new formalism to evaluate $\tau_{\mathrm{eff}}^{\mathrm{LL}}$ from stacked quasar spectra. We introduced an effective opacity from Lyman limits κ_{LL} which evolves with redshift and frequency as

$$\kappa_{\mathrm{LL}}(z, \nu) = \tilde{\kappa}_{912}(z)\left(\frac{\nu}{\nu_{912}}\right)^{-2.75} = \tilde{\kappa}_{912}(z)\left(\frac{1+z}{1+z_{912}}\right)^{-2.75}, \tag{12}$$

Table 5
Incidence of LLS

z	ΔX	Δz[a]	m_{LLS}[b]	$\langle z \rangle$[c]	$\ell(z)$	$\ell(X)$
WFC3/UVIS-G280; $\tau_{912}^{\mathrm{LL}} \geqslant 0.5$						
[1.20,2.00]	22.9	8.0	13	1.85	$1.62^{+0.44}_{-0.59}$	$0.57^{+0.15}_{-0.20}$
[2.00,2.60]	46.7	14.7	29	2.22	$1.97^{+0.36}_{-0.44}$	$0.62^{+0.11}_{-0.14}$
WFC3/UVIS-G280; $\tau_{912}^{\mathrm{LL}} \geqslant 1$						
[1.20,2.00]	32.5	11.4	12	1.80	$1.05^{+0.30}_{-0.40}$	$0.37^{+0.10}_{-0.14}$
[2.00,2.60]	52.5	16.5	25	2.19	$1.51^{+0.30}_{-0.37}$	$0.48^{+0.09}_{-0.12}$
WFC3/UVIS-G280; $\tau_{912}^{\mathrm{LL}} \geqslant 2$						
[1.20,2.00]	43.1	15.1	15	1.79	$0.99^{+0.25}_{-0.33}$	$0.35^{+0.09}_{-0.12}$
[2.00,2.60]	56.2	17.7	17	2.20	$0.96^{+0.23}_{-0.29}$	$0.30^{+0.07}_{-0.09}$
HST/ACS; $\tau_{912}^{\mathrm{LL}} \geqslant 2$						
[1.20,2.00]	23.3	8.4	4	1.70	$0.48^{+0.23}_{-0.38}$	$0.17^{+0.08}_{-0.14}$
[2.00,2.60]	17.4	5.5	5	2.16	$0.91^{+0.39}_{-0.61}$	$0.29^{+0.12}_{-0.19}$
Combined (with Ribaudo et al. 2011); $\tau_{912}^{\mathrm{LL}} \geqslant 2$						
[1.20,2.00]	108.0	39.0	29	1.77	$0.69^{+0.15}_{-0.15}$	$0.24^{+0.05}_{-0.05}$
[2.00,2.60]	107.8	34.8	32	2.21	$0.92^{+0.18}_{-0.18}$	$0.28^{+0.06}_{-0.06}$

Notes. The cosmology assumed has $\Omega_\Lambda = 0.74$, $\Omega_m = 0.26$, and $H_0 = 72\,\mathrm{km\,s^{-1}\,Mpc^{-1}}$. For the combined values, we adopted the measurements from Table 7 of Ribaudo et al. (2011) for the $z = [1.544, 1.947]$ and $z = [1.947, 2.594]$ bins. We also converted their $\ell(X)$ measurements to our cosmology with a simple scaling.
[a] Total redshift survey path.
[b] Number of LLS discovered in the survey path. Note that two LLS occurring within $\approx 10,000\,\mathrm{km\,s^{-1}}$ of one another have been treated as one system.
[c] Mean absorption redshift of the LLS.

where the second term accounts for the photoionization cross-section[9] (accurate to within 1% to $\lambda_r \approx 600$ Å). One may relate this opacity to the optical depth through the standard definition[10]

$$\tau_{\mathrm{eff}}^{\mathrm{LL}}(r, \nu) = \int_0^r \kappa_{\mathrm{LL}}(r', \nu)\, dr', \qquad (13)$$

and relate distance to redshift via cosmology

$$\frac{dr}{dz} = \frac{c}{(1+z)H(z)} = \frac{c/H_0}{(1+z)\sqrt{\Omega_m(1+z)^3 + \Omega_\Lambda}}. \qquad (14)$$

In PWO09 we performed this analysis at $z \sim 4$ where the Hubble parameter $H(z)$ is dominated by matter and one can approximate $dr/dz \propto (1+z)^{-5/2}$. At the redshifts of interest here ($z \lesssim 2$), we find that a power law representation,

$$\frac{dr}{dz}(z < 2.6) \approx \frac{dr}{dz}(z = 2.6)\left[\frac{1+z}{3.6}\right]^{-2.315}, \qquad (15)$$

is accurate to within 1% for $z = 1$–2.5. We adopt this power law approximation in the following, taking $dr/dz(z = 2.6) = 322\,h_{72}^{-1}$ Mpc. Altogether our expression becomes

$$\tau_{\mathrm{eff}}^{\mathrm{LL}}(z_{912}, z_{\mathrm{em}}) = 6237\,\mathrm{Mpc}\,(1 + z_{912})^{2.75}$$
$$\times \int_{z_{912}}^{z_{\mathrm{em}}} \tilde{\kappa}_{912}(z')\,(1 + z')^{-5.065}\,dz'. \qquad (16)$$

Note that this formalism is primarily introduced to parametrically solve for $\lambda_{\mathrm{mfp}}^{912}$ by establishing the redshift where $\tau_{\mathrm{eff}}^{\mathrm{LL}} = 1$. In contrast to the PWO09 analysis of SDSS spectra, the WFC3/UVIS-G280 data have the wavelength coverage and sensitivity to produce a stacked spectrum to $\lambda_r \approx 600$ Å. In part, this reflects the larger mean free path to ionizing radiation at $z \sim 2$ than $z \sim 4$. If one wishes to analyze the stacked spectrum to these wavelengths, however, it is not safe to assume that the modulations in flux at $\lambda_r < 912$ Å are due solely to Lyman limit opacity (as was done by PWO09[11]). First, one must consider evolution in the intrinsic SED f_λ^{SED} over these wavelengths. For example, the $z \sim 1$ average quasar spectrum produced by Telfer et al. (2002) follows a power law $\bar{f}_\lambda^{\mathrm{SED}} \propto \lambda^{-0.43}$ at $\lambda_r < 1200$ Å which implies a 20% higher flux at $\lambda_r = 600$ Å than at the Lyman limit. Second, the Lyman series opacity $\tau_{\mathrm{eff}}^{\mathrm{Lyman}}$ is certain to decrease with redshift. Therefore, the observed flux should increase at $\lambda_r < 900$ Å in the absence of Lyman limit opacity.

Lastly, we also expect the mean free path to increase with decreasing redshift as the universe expands. In the SDSS analysis at $z \sim 4$, the mean free path was so short that we had no sensitivity to redshift evolution in κ_{LL} from a single stacked spectrum (PWO09). By examining stacked spectra over a (narrow) range of redshifts, however, we revealed evidence for an increasing $\lambda_{\mathrm{mfp}}^{912}$ with decreasing redshift. In the WFC3/UVIS-G280 stacked spectrum, the flux covered includes opacity from absorbers spanning from $z_{912} \approx 1$–2.5 and one must consider explicit redshift evolution in κ_{LL}. We assume the $\tilde{\kappa}_{912}(z)$ opacity term in Equation (12) evolves as a power law with the

---

[9] In PWO09 we assumed a ν^{-3} dependence which is not as accurate. Furthermore, there is essentially no frequency dependence on the effective opacity for systems with very high $N_{\mathrm{H\,I}}$, which our approach ignores.
[10] This formalism wrongly ignores stimulated emission, but that has a negligible effect on our model.

[11] This assumption was justified, in part, because the analysis was performed over a very short wavelength (redshift) interval, $\lambda_r \approx 850$ Å–900 Å.

scale factor $a = 1/(1+z)$,

$$\tilde{\kappa}_{912}(z) = \tilde{\kappa}_{912}(z_{stack}) \left[\frac{1+z}{1+z_{stack}} \right]^{\gamma_\kappa}, \qquad (17)$$

where z_{stack} is the median redshift of the quasars whose spectra are averaged. This assumed functional form for $\tilde{\kappa}_{912}$ is motivated by the fact that the evolution should be dominated by expansion of the universe and the empirical observation that many aspects of the IGM are well modeled by power laws of the scale factor. We would reconsider this parameterization if it provided a poor model for the data.

5.2. Generating the WFC3/UVIS-G280 Stacked Spectrum

As described in the previous subsection, constraints on the mean free path at $z < 2.5$ may be derived from analysis of the average quasar spectrum of $z_{em} \approx 2.5$ quasars. Our WFC3/UVIS-G280 dataset comprises 53 quasars with $z_{em} = 2.3$–2.6 (median of 2.44), each chosen to be free of significant associated absorption. We have taken the following procedure to combine the individual spectra, accounting for the differences in z_{em} and also the non-uniform dispersion of the WFC3/UVIS-G280 grism spectra.

First, we correct for reddening of the quasar flux by adopting the $E(B-V)$ estimate from Schlegel et al. (1998) and a standard Galactic extinction curve Fitzpatrick & Massa (1990). In general, this is a small correction because the median reddening value is $E(B-V) = 0.02$ mag. On the other hand, our spectra cover the so-called 2175 Å bump in the extinction curve which implies an additional correction. Second, we generate a rest-frame wavelength array with fixed dispersion $\Delta\lambda$. The dispersion value was set to be large enough to include at least one entire pixel from the WFC3/UVIS-G280 spectra at rest wavelengths $\lambda_r < 1215$ Å. Specifically, we adopted $\Delta\lambda = 6.1897$ Å. Third, each quasar spectrum was shifted to the rest-frame and normalized by the median flux from $\lambda_r = 1450$ Å–1470 Å. Fourth, we assigned the entire flux of each pixel from the original spectrum to the nearest pixel of the stacked spectrum. Lastly, all of the flux values in the final spectrum were averaged to produce the $\bar{f}_\lambda$ spectrum, normalized to unity at $\lambda = 1450$ Å.

The resultant WFC3/UVIS-G280 stacked spectrum is shown as the solid black line in Figure 8, and tabulated in Table 6. To assess sample variance, we generated a set of stacked spectra with standard bootstrap techniques. Specifically, we generated 500 stacked spectra by drawing randomly from the 53 quasar spectra, allowing for duplications. The shaded region in Figure 8 shows the rms at each pixel after clipping any 3σ outliers. To some degree, this bootstrap analysis provides estimates on the uncertainty in our measurement of the average observed quasar flux at $z \approx 2.4$, subject to the selection criteria of the sample.

Overplotted on the stacked spectrum is the average radio-quiet quasar spectrum of Telfer et al. (2002), produced from a set of $z \sim 1$ quasars observed with UV spectrometers on *HST* and modified as follows. The Telfer spectrum has been normalized at $\lambda_r = 1450$ Å, smoothed to the WFC3/UVIS-G280 spectral resolution, and rebinned to the dispersion solution of the WFC3/UVIS-G280 stacked spectrum. At wavelengths $\lambda_r \approx 1300$ Å, the WFC3/UVIS-G280 stacked spectrum has flux that modestly exceeds the Telfer spectrum. This suggests that the WFC3/UVIS-G280 stack has a bluer underlying power law continuum but it could also result from strong line emission (e.g., O I 1302) at those wavelengths. We explore this issue in greater depth in Section 5.4.2.
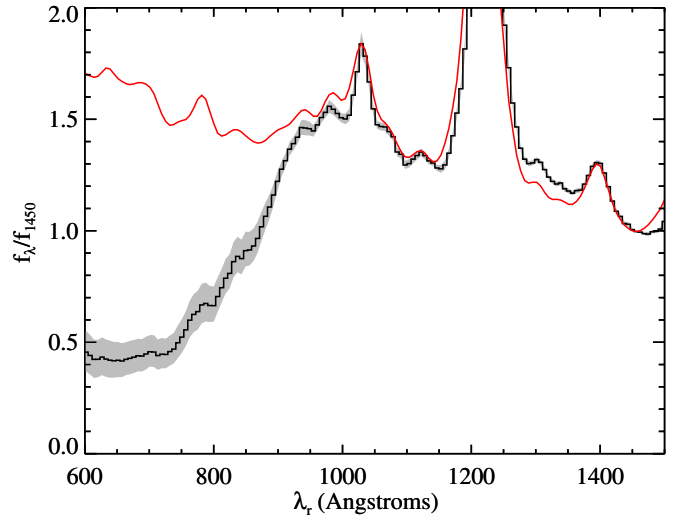

Figure 8. The black histogram shows the average quasar spectrum at $z = 2.44$ as estimated from a stack of the WFC3/UVIS-G280 spectra, each normalized to unit flux at $\lambda_r = 1450$ Å. Note the strong decrease in flux at $\lambda_r < 900$ Å due to the onset and cumulative effect of the Lyman limit opacity. The gray shaded region shows the rms at each pixel as measured from standard bootstrap analysis. The solid red curve shows the radio-quiet average quasar spectrum of Telfer et al. (2002), smoothed to the resolution and dispersion of the WFC3/UVIS-G280 stack. Their estimate of the intrinsic quasar flux, when normalized at $\lambda_r = 1450$ Å, lies below the WFC3/UVIS-G280 stack at $\lambda_r \approx 1300$ Å and would imply an effective opacity at Lyα $\tau_{eff}^{Ly\alpha}$ that is significantly smaller than previous estimates. We infer, therefore, that our WFC3/UVIS-G280 quasar cohort has an average SED that is bluer (harder) than the Telfer et al. (2002) sample at far-UV wavelengths.

(A color version of this figure is available in the online journal.)

Table 6
WFC3/UVIS-G280 Stacked Spectrum

λ_r (Å)	$f_\lambda{}^a$	$\sigma(f_\lambda)^b$
601.92	0.46	0.09
608.11	0.44	0.09
614.30	0.42	0.09
620.49	0.42	0.08
626.68	0.43	0.08
632.87	0.42	0.08
639.06	0.42	0.08
645.25	0.42	0.08
651.44	0.42	0.08
657.63	0.42	0.08
663.82	0.42	0.07
670.01	0.43	0.08
676.20	0.43	0.07
682.39	0.44	0.07
688.58	0.44	0.07
694.77	0.45	0.07
700.96	0.46	0.07
707.14	0.46	0.07
713.33	0.44	0.07
719.52	0.45	0.07

Notes.
[a] Flux per Å normalized to unity at $\lambda_r = 1450$ Å.
[b] rms (with 3σ clipping) in the flux from a bootstrap analysis (see text).

(This table is available in its entirety in a machine-readable form in the online journal. A portion is shown here for guidance regarding its form and content.)

At all wavelengths $\lambda_r < 1200$ Å, the Telfer spectrum exceeds the WFC3/UVIS-G280 stack. Here, the WFC3/UVIS-G280 stacked spectrum includes absorption by the intergalactic medium, whereas the Telfer spectrum has been corrected for IGM absorption (to the best of their abilities). For wavelengths $\lambda_r \approx 1100$ Å, the offset is $\sim 10\%$ and it increases with decreasing wavelength as additional terms in the Lyman series contribute (Equation (9)). Beyond the Lyman limit, the flux for the WFC3/UVIS-G280 stack drops rapidly owing to the integrated continuum opacity of the Lyman limit $\tau_{\rm eff}^{\rm LL}$ (Equation (11)). At $\lambda_r \approx 600$ Å, the ratio of the Telfer spectrum to the WFC3/UVIS-G280 stack implies a total effective optical depth $\tau_{\rm eff}^{\rm TOT} \sim 1.5$. We expect the opacity at these wavelengths to be dominated by the Lyman limit opacity. We now model this absorption and thereby place new constraints on the IGM at $z \sim 2$.

5.3. Mock Spectra

To better gauge the effects of sample variance, to test our stacking, and to examine the evolution of quantities such as $\tau_{\rm eff}^{\rm Lyman}$, we created a number of sets of mock WFC3/UVIS-G280 spectra. The mocks were utilized at each stage of the analysis of the real WFC3/UVIS-G280 stack described below, both to develop and test our analysis algorithms, and to better explore the range of likely errors for each measured quantity.

The mock spectra were generated from simulated H I line distributions based on empirical parameterizations (e.g., Madau et al. 1996; Worseck & Prochaska 2011). Under the implicit assumption that the Lyα forest is a collection of Voigt profiles with uncorrelated parameters (redshift z, column density $N_{\rm H\,I}$, Doppler parameter b), we populated each simulated sightline with absorbers until the Lyα effective optical depth converged to a given value. If the Lyα effective optical depth evolves as $\tau_{\rm eff}^{\rm Ly\alpha} \propto (1+z)^{\gamma+1}$, the line density is $l \propto (1+z)^{\gamma}$. At $z < 1.5$ we assumed $\tau_{\rm eff}^{\rm Ly\alpha} = 0.017(1+z)^{1.20}$ (Kirkman et al. 2007), whereas at $z > 1.5$ we incorporated the observed steepening in the $\tau_{\rm eff}^{\rm Ly\alpha}$ evolution by taking $\tau_{\rm eff}^{\rm Ly\alpha} = 0.0062(1+z)^{3.04}$ (Dall'Aglio et al. 2008).

For the Doppler parameters we adopted the single parameter distribution function by Hui & Rutledge (1999) $dn/db \propto b^{-5}\exp(-b^4/b_\sigma^4)$ with $b_\sigma = 24$ km s^{-1} (Kim et al. 2001) restricted to 10 km s$^{-1} \leqslant b < 100$ km s^{-1}. The main distribution of interest is the column density distribution for which we assumed a triple power law $f(N_{\rm H\,I}, N_{\rm H\,I}^{\rm min}, N_{\rm H\,I}^{\rm max}) = C_i \times N_{\rm H\,I}^{-\beta_i}$ over the range $12 < \log N_{\rm H\,I} < 22$. The constants C_i implicitly depend on the $\tau_{\rm eff}^{\rm Ly\alpha}$ evolution, so we determined them from 5000 simulated sightlines for each of our sets of slopes β_i. By varying these three slopes we recovered different values of the mean free path (Equation (11)). In total, we ran 42 different models that resulted in a wide range of mean free paths at $z = 2.4$ from 40 Mpc to the horizon length. For simplicity we discarded most of these and considered only those with simulated mean free paths close to our measured value.

With these Monte-Carlo simulated line lists we then generated mock WFC3/UVIS-G280 spectra as follows: For each of the 53 quasars in our sample we first generated a mock quasar SED by multiplying the Telfer et al. (2002) composite with a power law $f_\lambda = (\lambda_{\rm rest}/2500\,{\rm Å})^\alpha$ with α drawn from a Gaussian distribution with $\sigma = 0.2$. The mock SED was normalized between 1430 and 1470 Å. We then randomly drew one of the 5000 sightline realizations, simulated the resolved

Lyman series and continuum spectrum at $0 < z < z_{\rm em}$, multiplied it onto the interpolated SED, convolved it with the WFC3/UVIS-G280 grism line spread function and rebinned it to the WFC3/UVIS-G280 grism dispersion solution. Lastly, we added Gaussian noise to the spectra to match the quality of our WFC3/UVIS-G280 spectra (S/N ~ 30 at 1350 Å), taking into account both the shape of the mock quasar spectrum and the WFC3/UVIS-G280 sensitivity function.

5.4. Modeling the Stacked Spectrum

In this subsection, we describe our approach to modeling the stacked quasar spectrum from the WFC3/UVIS-G280 sample (Figure 8, Table 6). Our scientific emphasis is to place new constraints on the magnitude and evolution of the mean free path $\lambda_{\rm mfp}^{912}$ at $z \approx 2$. Nevertheless, the data redward of the Lyman limit offer additional constraints on the intrinsic SED of $z \sim 2.5$ quasars and also the Lyman series opacity at $z \sim 2$. We consider each of these in turn.

5.4.1. QSO SED

Central to our experiment is the fact that we use quasar light to probe the foreground IGM. To some extent, it is an observational necessity for revealing the nature of this medium. Galaxies are too faint for current facilities, especially at $\lambda_r < 2000$ Å, and gamma-ray bursts or supernovae are too faint and/or fade too rapidly to generate sufficiently large samples, especially with UV spectroscopy.

As is apparent from previous work on the rest-frame SED of quasars at UV wavelengths (e.g., Telfer et al. 2002; Vanden Berk et al. 2001; Scott et al. 2004), these sources do not have smoothly varying, intrinsic continua. Although the underlying SED is roughly a power law ($f_\lambda \propto \lambda^\alpha$ with $\alpha \approx -1.3$ for $\lambda_r > 1200$ Å), there are significant and broad emission lines from the H I Lyman series and metal-line transitions. Furthermore, individual quasars exhibit a range of power law slopes and varying strengths of line emission. Despite this diversity, it is remarkable that quasars as a population have a very similar average SED at all redshifts (e.g., Vanden Berk et al. 2001). Outside the Lyα forest, for example, the SED in the UV is nearly identical between the $z \sim 1$ Telfer spectrum and the average spectrum of $z \sim 3$ quasars (Vanden Berk et al. 2001). There is only a hint of a harder SED for higher z quasars (Telfer et al. 2002) and also modest differences in the equivalent widths of high-ionization emission lines (Baldwin 1977). At wavelengths $\lambda_r < 1200$ Å, however, Telfer et al. (2002) report a break in the quasar SED power law to $f_\lambda \propto \lambda^{-0.4}$ that is not evident in other analyses (e.g., Scott et al. 2004). This difference could be related to redshift evolution and/or the average luminosity of the quasars sampled. Recently, Shull et al. (2012) have published a composite spectrum from high-dispersion *HST*/COS observations (with corrected Lyman limit absorption) and find results that are in good agreement with the Telfer et al. SED.

Because of the remarkable similarity in the average SED of bright quasars with redshift, we adopt the following assumption for modeling the WFC3/UVIS-G280 stacked spectrum: we assume the underlying SED is the Telfer et al. radio-quiet spectrum modulated by a tilted power law,

$$\bar{f}_\lambda^{\rm SED} = C_{\rm T}\, f_\lambda^{\rm Telfer} \left(\frac{\lambda}{1450\,{\rm Å}}\right)^{\delta\alpha_{\rm T}}, \qquad (18)$$

and a scaling parameterized by C_T. Returning to Figure 8, we propose that the offset between the Telfer spectrum and the WFC3/UVIS-G280 stack at $\lambda_r \approx 1300$ Å may result from a difference in the average power law of the two stacked spectra. Indeed, the data are well matched if we assume $\delta\alpha_T \approx -0.5$. Interestingly, such a tilt is akin to arguing that there is no break in the average quasar SED at $\lambda_r \approx 1200$ Å, contrary to the findings of Telfer et al. (2002) but consistent with other estimations (Scott et al. 2004). The inclusion of a tilt also allows for the fact that Telfer et al. (2002) may not have properly or entirely corrected for IGM absorption at $\lambda < 900$ Å. For example, the authors did not correct for partial LLS, which are expected to be rare at $z < 1$ (Ribaudo et al. 2011) but not negligible.

In the following, we restrict $\delta\alpha_T$ by demanding that the effective Lyα opacity $\tau_{\mathrm{eff}}^{\mathrm{Ly}\alpha}$ derived from our stacked spectra matches previous estimates from analysis of higher spectral-resolution data (Kirkman et al. 2005). Similarly, the parameter C_T allows for a normalization offset between the Telfer stack and the WFC3/UVIS-G280 stack. Although each spectrum was normalized at $\lambda_r \approx 1450$ Å, there may be a modest difference in the emission-line strength at these wavelengths and it is non-trivial to precisely measure the flux of each stacked spectrum at a given wavelength. Therefore, we allow for a 5% modulation in the normalization.

5.4.2. Constraints on the Intrinsic SED from $\tau_{eff}^{Ly\alpha}$

As noted in the previous sub-section, we have significant reason to believe that the average intrinsic quasar SED for our WFC3/UVIS-G280 sample does not follow the standard Telfer quasar spectrum. This is suggested by the offset at $\lambda_r \approx 1300$ Å, but is even more apparent in the Lyα forest (Figure 8). At $\lambda_r \approx 1100$ Å, for example, the Telfer spectrum lies only a few percent above the stacked spectrum which would imply almost zero effective Lyα opacity at $z \approx 2$. This contradicts our knowledge of the IGM at these redshifts, as informed by high S/N, high spectral-resolution observations (e.g., Kirkman et al. 2005; Kim et al. 2007). Indeed, we now invert the problem to constrain the average quasar SED of our quasar sample, using previous estimates of $\tau_{\mathrm{eff}}^{\mathrm{Ly}\alpha}$.

Previous authors have estimated the effective opacity from the Lyα forest using higher spectral resolution data of $z \sim 2.5$ quasars (Kirkman et al. 2005; Kim et al. 2007). The standard approach is to estimate the intrinsic quasar continuum $\bar{f}^{\mathrm{SED}}$ from the data directly and then measure the average absorption,

$$D_A \equiv 1 - f^{\mathrm{obs}}/f^{\mathrm{SED}}, \qquad (19)$$

between the Lyα and Lyβ emission lines corresponding to a redshift slightly less than z_{em}. Depending on the author, estimations for D_A may include only the low density Lyα forest, all Lyα lines (i.e., including strong absorbers like DLAs), and/or metal-line absorption. Because our WFC3/UVIS-G280 stacked spectrum includes the opacity from all of these sources, we wish to compare against a total estimate D_A^T. Tytler et al. (2004) report a total D_A^T value at $z = 2.14$ of 0.18 ± 0.04. Analysis of SDSS quasar spectra provides a similar value (Dall'Aglio et al. 2008).

In Figure 9 we present a series of SED models for our intrinsic spectrum comparing to a range of tilts and normalizations ($\delta\alpha_T$, C_T) applied to the Telfer spectrum. In each case, we have demanded that the average opacity at $\lambda_r = [1080, 1140]$ Å fall within the 1σ interval given by D_A^T. Restricting C_T to $\pm 5\%$, we find $\delta\alpha_T$ values ranging from ≈ -0.2 to -1. It is very unlikely that the unaltered Telfer spectrum provides a good
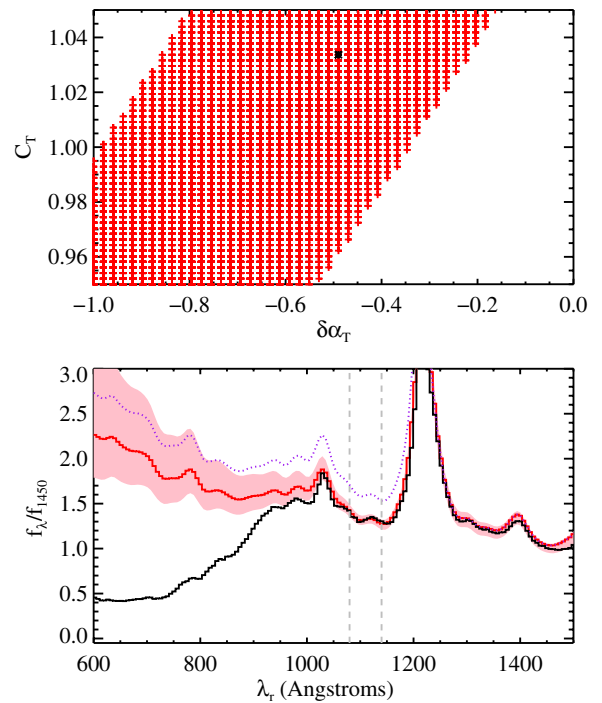

Figure 9. Upper panel: allowed values for the normalization C_T and tilt $\delta\alpha_T$ of the Telfer et al. (2002) quasar SED (relative to the Telfer et al. 2002 spectrum) that give the effective Lyα opacity $\tau_{\mathrm{eff}}^{\mathrm{Ly}\alpha}$ measured at $z = 2.14$ by Tytler et al. (2004). The black asterisk denotes the model that minimizes χ^2 from $\lambda_r = 1080$–1140 Å; this model of the intrinsic spectrum is shown in the lower panel. We find that the WFC3/UVIS-G280 stack favors a bluer SED ($\delta\alpha_T < 0$) than the Telfer spectrum. Lower panel: the black histogram is the WFC3/UVIS-G280 stacked spectrum and the dotted curve is the Telfer spectrum scaled and tilted to the "best" C_T and $\delta\alpha_T$ values (black asterisk in the upper panel). The solid red line shows this intrinsic SED attenuated by a constant $\tau_{\mathrm{eff}}^{\mathrm{Ly}\alpha} = 0.19$ for $\lambda < \lambda_{\mathrm{Ly}\alpha}$. The shaded region shows the range of models corresponding to the range of C_T and $\delta\alpha_T$ values in the upper panel. The gray dashed lines indicate the region where D_A was evaluated.

(A color version of this figure is available in the online journal.)

description of the intrinsic SED for our WFC3/UVIS-G2803 cohort. Instead, the data favor a bluer SED at $\lambda_r < 1200$ Å. In fact, the preferred tilt for $C_T = 1$ of $\delta\alpha_T \approx -0.5$ nearly corresponds to maintaining the $f_\lambda \propto \lambda^{-1.3}$ power law that is observed for quasars at $\lambda_r > 1200$ Å (Telfer et al. 2002; Vanden Berk et al. 2001). While it is possible that a portion of this tilt relates to error in the fluxing of the WFC3/UVIS-G2803 spectra (Paper I), it is very unlikely to be entirely explained by such systematic effects. Instead, we conclude that the WFC3/UVIS-G280 quasar cohort has a harder SED than the $z \sim 1$, Telfer et al. radio-quiet sample. In addition to the implications for our analysis of the IGM, a harder SED would imply a higher emissivity of ionizing photons from $z \sim 2$ quasars. In turn, it would increase the quasar contribution to the extragalactic UV background at these redshifts.

The bluer SED relative to the Telfer analysis may also arise from the color-selection of SDSS quasar candidates. At $z \sim 2.5$, the average quasar color lies near the stellar locus (e.g., Richards et al. 2006) and therefore, the SDSS team weighted their targeting algorithms toward quasars with UV-excess (i.e., bluer SED). Indeed, Worseck & Prochaska (2011) have estimated that SDSS quasars with spectroscopic redshift $z \approx 2.5$ would have $\delta\alpha_T \approx -0.3$ (see their Figure 16). We encourage additional analysis of quasars at $z > 2$ to further explore this issue.

Although the above analysis prefers a hard SED, we emphasize that a tilt $\delta\alpha_T \approx -1$ is not well supported by the individual spectra. None of the quasars exhibit such a blue SED at $\lambda \ll 1200$ Å. For example, the quasars J083326+081552 and J121519+424851, which appear to have minimal Lyman limit absorption from the IGM, are better described by $\delta\alpha_T \approx -0.5$ at such wavelengths. Therefore, in the following, we restrict the analysis to SED models with $\delta\alpha_T = [-0.8, -0.2]$.

5.4.3. Lyman Series Opacity

Although the Lyα forest is characterized by a series of narrow ($\delta v \leqslant 50\,\mathrm{km\,s^{-1}}$) and stochastically distributed absorption-lines, the WFC3/UVIS-G280 stacked spectrum exhibits no discrete absorption features. This follows from the low spectral-resolution of the individual WFC3/UVIS-G280 spectra and also the effects of spectral stacking. As detailed in Section 5.1, the Lyman series opacity should increase with decreasing rest-wavelength as additional transitions contribute (Equation (9)). Below the Lyman limit, however, the total Lyman opacity $\tau_{\mathrm{eff}}^{\mathrm{Lyman}}$ is then expected to decline with decreasing redshift (i.e., as the universe expands).

One may relate the effective opacity at a given Lyman transition to the frequency distribution of IGM absorption lines $f(N_{\mathrm{H\,I}}, b, z)$ as,

$$\tau_{\mathrm{eff}}^n = \int\int\int f(N_{\mathrm{H\,I}}, b, z)\exp\left(-\tau_\nu^n\right)dN_{\mathrm{H\,I}}\,db\,dz, \quad (20)$$

where τ_ν^n is the line opacity of transition n and is a function of $N_{\mathrm{H\,I}}$, b, and z. Because $f(N_{\mathrm{H\,I}})$ is estimated to decline at least as steeply as $N_{\mathrm{H\,I}}^{-1.5}$, one predicts the effective opacity of a given Lyman transition to be dominated by the minimum column density for line saturation. This means that $\tau_{\mathrm{eff}}^{\mathrm{Ly}\alpha}$ is set by lines with $N_{\mathrm{H\,I}} \approx 10^{14}\,\mathrm{cm^{-2}}$ whereas the higher order transitions are defined by lines with $N_{\mathrm{H\,I}} \approx 10^{17}\,\mathrm{cm^{-2}}$. Indeed, for reasonable $f(N_{\mathrm{H\,I}}, X)$ distributions we estimate that roughly half of the total opacity derives from the first few transitions ($n = 2$–5, i.e., Lyα–Lyδ) with the remainder contributed by higher order transitions.

To estimate the $\tau_{\mathrm{eff}}^{\mathrm{Lyman}}$ opacity from the frequency distribution, therefore, one requires: an accurate description over many orders of magnitude in $N_{\mathrm{H\,I}}$, an assessment of the Doppler parameter distribution, and also an accurate estimation of their evolution with redshift. While there has been some analysis on $f(N, b, z)$ at $z \sim 2$, the constraints are quite limited. Given this uncertainty, we have made our own estimate of $\tau_{\mathrm{eff}}^{\mathrm{Lyman}}$ from the WFC3/UVIS-G280 stacked spectrum, corresponding to $z = z_{\mathrm{stack}} = 2.44$. In Figure 10 we estimate $\tau_{\mathrm{eff}}^{\mathrm{Lyman}}$ allowing for the range of intrinsic quasar SEDs described in the previous subsection. The top panel shows the recovered $\tau_{\mathrm{eff}}^{\mathrm{Lyman}}$ values as a function of tilt $\delta\alpha_T$ in the SED. The bottom panel shows the range of allowed SEDs compared against the WFC3/UVIS-G280 stacked spectrum. We also present the unaltered Telfer spectrum (purple, dotted line) to further emphasize that this SED is inconsistent with the observations. If we assume that $\delta\alpha_T = -0.8$ to -0.2 at 95% c.l., then this implies $\tau_{\mathrm{eff}}^{\mathrm{Lyman}} = 0.40 \pm 0.15$ at similar confidence. There will be additional uncertainty from sample variance, but we estimate that this contributes less than the uncertainty related to the quasar SED.

This estimate for $\tau_{\mathrm{eff}}^{\mathrm{Lyman}}$ may be crudely compared against the incidence of $\tau > 1$ LLS derived from our spectra. Specifically,
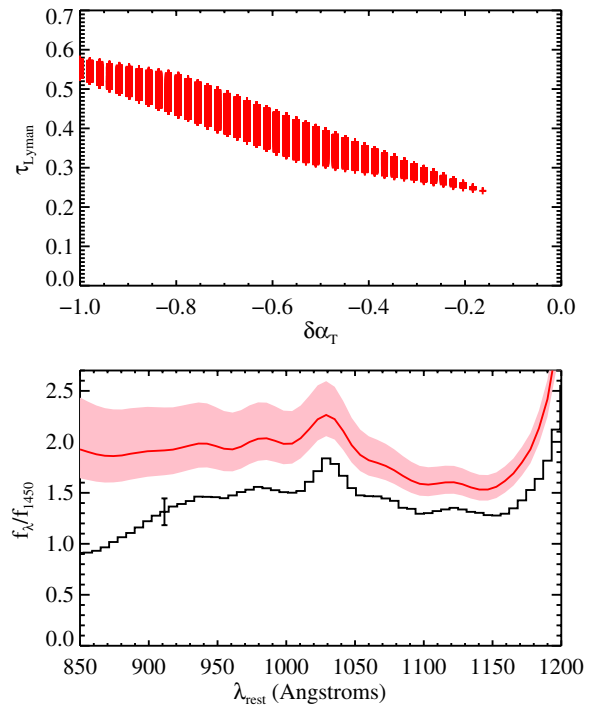

Figure 10. Upper panel: estimations of the effective Lyman series opacity $\tau_{\mathrm{eff}}^{\mathrm{Lyman}}$ as a function of the tilt in the Telfer quasar spectrum $\delta\alpha_T$. Naturally, one estimates larger $\tau_{\mathrm{eff}}^{\mathrm{Lyman}}$ values for steeper quasar SEDs. We estimate $\tau_{\mathrm{eff}}^{\mathrm{Lyman}} \approx 0.4$ at $z = 2.44$. Lower panel: the black histogram shows the stacked WFC3/UVIS-G280 quasar spectrum with the error bar at $\lambda_r = 912$ Å showing a 10% error estimate in the average observed flux at that wavelength. The solid red curves and the shaded region show the range of quasar SEDs that satisfy the $\tau_{\mathrm{eff}}^{\mathrm{Ly}\alpha}$ constraint (Figure 9). These are used in the estimates of $\tau_{\mathrm{eff}}^{\mathrm{Lyman}}$ shown in the upper panel.

(A color version of this figure is available in the online journal.)

one may assume that $\approx 50\%$ of the opacity is contributed by the higher order lines and then compare this value to an estimate for $\tau_{\mathrm{eff}}^{\mathrm{Lyman}}$ for LLS from an evaluation of Equation (11). Taking $N_{\mathrm{H\,I}} \geqslant 10^{17.19}\,\mathrm{cm^{-2}}$, $\ell(z) = 1.5$ for $z = 2.0$, $b_{\mathrm{eff}} = 35\,\mathrm{km\,s^{-1}}$, and assuming $f(N, z) \propto N^{-1.5}(1 + z)^{1.33}$ yields $\tau_{\mathrm{eff}} = 0.06$ for the transitions $n = 5$–30. This value is considerably lower than the $\tau_{\mathrm{eff}}^{\mathrm{Lyman}}$ value derived from above, and it suggests that systems with $N_{\mathrm{H\,I}} < 10^{17.2}\,\mathrm{cm^{-2}}$ dominate the Lyman series opacity. This conclusion is consistent with our inferences of a steep $f(N)$ distribution at $N_{\mathrm{H\,I}} \approx 10^{16}\,\mathrm{cm^{-2}}$ (Section 4.6; see also Ribaudo et al. 2011).

In the following, we model the WFC3/UVIS-G280 stacked spectrum with a range of $\tau_{\mathrm{eff}}^{\mathrm{Lyman}}$ values. In fact, we take exactly the $\tau_{\mathrm{eff}}^{\mathrm{Lyman}}$ value required to reproduce the observed flux at $\lambda_r = 912$ Å for a given quasar SED and then allow for a 10% variation which significantly exceeds what can be measured from our high S/N stack and therefore is a conservative range. For $\lambda_r < 912$ Å, we further assume that $\tau_{\mathrm{eff}}^{\mathrm{Lyman}}$ decreases as a $(1 + z)^{\gamma_\tau}$ power law,

$$\tau_{\mathrm{eff}}^{\mathrm{Lyman}}(\lambda_r) = \tau_{\mathrm{eff}}^{\mathrm{Lyman}}(\lambda_r = 912\,\text{Å})\left(\frac{1 + z_{912}}{1 + z_{\mathrm{em}}}\right)^{\gamma_\tau}. \quad (21)$$

This is justified by the fact that $f(N_{\mathrm{H\,I}}, z)$ is generally well-described by such a power law. On the other hand, different $N_{\mathrm{H\,I}}$ regimes and different redshift ranges may be described by different γ_τ values (Janknecht et al. 2006). We proceed under the

Table 7
Stacked Spectrum Model Parameters and λ_{mfp}^{912}

Parameter	Mean	Median	1σ c.l.	2σ c.l.
C_T	1.03	1.04	0.99,1.05	0.95,1.05
$\delta\alpha_T$	-0.37	-0.33	$-0.60, -0.20$	$-0.80, -0.20$
τ_{eff}^{Lyman}	0.29	0.28	0.24, 0.35	0.21, 0.44
γ_τ	1.64	1.73	1.40, 1.80	1.20, 1.80
$\tilde{\kappa}_{912}(z_{stack})$	33.64	33.93	28.12, 39.07	24.42, 47.15
γ_κ	0.42	0.00	0.00, 1.12	0.00, 2.55
z_{912}	1.877	1.890	1.791, 1.958	1.713, 2.018
λ_{mfp}^{912} (h_{72}^{-1} Mpc)	252.1	243.4	207.3,303.7	177.3,353.1

expectation that the total τ_{eff}^{Lyman} is nevertheless well described by a power law over the redshift interval relevant to our analysis $z_{912} \approx 1.5$ to 2.4. Specifically, we allow γ_τ to range from 1.2 to 1.8 which spans the range of values estimated for the Lyα forest (Janknecht et al. 2006) and LLS (Section 4; Ribaudo et al. 2011) at $z \lesssim 2$.

5.4.4. Lyman Limit Opacity

Following the formalism presented in Section 5.1, we characterize the Lyman limit opacity κ_{LL} as given by Equations (12) and (17). This is a two-parameter model that sets the normalization at $z = z_{stack}$ and allows for redshift evolution. In the following, we will demand that $\gamma_\kappa > 0$, i.e., that λ_{mfp}^{912} increases[12] with decreasing redshift as expected from the decreasing incidence of LLS (Section 4.1.1).

5.5. Constraining the Mean Free Path

We now proceed to compare a suite of models against the observed WFC3/UVIS-G280 stacked spectrum to estimate the mean free path λ_{mfp}^{912}. We proceed with standard χ^2 analysis where the uncertainty at each pixel in the stacked spectrum is estimated from a bootstrap analysis (Section 5.2). This yields a "best" estimate for λ_{mfp}^{912}. In turn, we provide an estimate of the uncertainty in this quantity by repeating such analysis on a set of stacked spectra generated with standard bootstrap techniques. There are several issues to note regarding this approach. First, the bootstrap analysis of the stacked spectrum provides an estimate of the rms at each pixel in the stack, but we caution that the probability density function need not follow a true Gaussian. On the other hand, we find our results are relatively insensitive to what we assume for the error in the stacked spectrum. Second, the bootstrap analysis may not properly reflect the full uncertainty in the stacked spectrum related to sample variance, i.e., the stacked spectrum was derived from a total of 53 quasars. Lastly, this approach ignores the fact that the data at $\lambda_r < 912$ Å are highly correlated. This correlation occurs because of the nature of Lyman limit absorption; a system at $z = z_{912}$ attenuates the flux at all wavelengths $\lambda_r < 912$ Å $(1 + z_{912})/(1 + z_{em})$. Therefore, one predicts (and observes) a monotonic decrease in the stacked spectrum for $\lambda_r < 912$ Å. The first two issues described above suggest an underestimate of the uncertainty while the last point may lead to an overestimate.

Our model has six parameters: two for the quasar SED ($\delta\alpha_T$, C_T), two to model the Lyman series opacity ($\tau_{eff}^{Lyman}(z = z_{em})$, γ_τ), and two to model the Lyman limit opacity ($\tilde{\kappa}_{912}(z_{stack})$, γ_κ).

---

[12] Formally, $\gamma_\kappa = 0$ also implies an increasing λ_{mfp}^{912} because of the expanding universe.
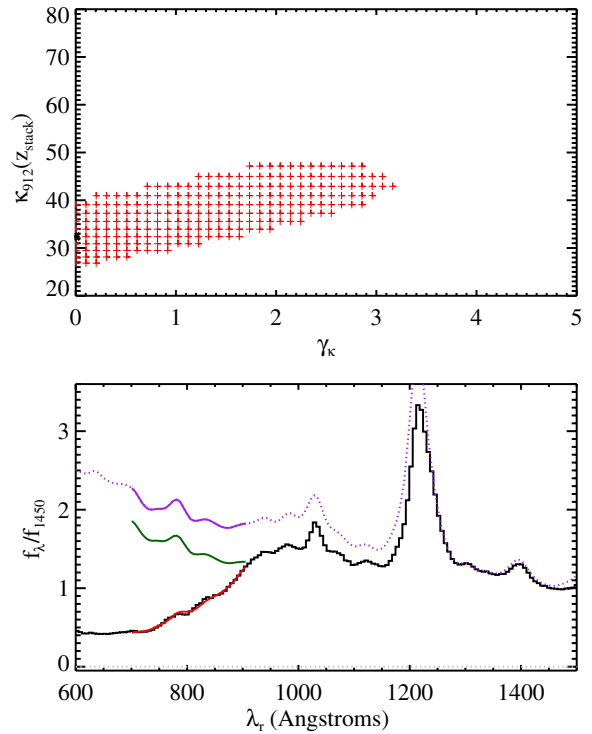

Figure 11. Upper panel: estimated constraints on $\tilde{\kappa}_{912}(z_{stack})$ and γ_κ, our model parameters for the opacity of the universe to ionizing radiation at $z_{stack} = 2.44$ (Equation (12)). These parameters are highly degenerate with one another. Lower panel: the black histogram is the WFC3/UVIS-G280 stacked quasar spectrum, normalized at $\lambda_r = 1450$ Å. The purple dotted curve shows the best estimate of the intrinsic quasar continuum, i.e., the scaled and tilted Telfer spectrum as given in Table 7. The solid green curve gives the intrinsic SED attenuated by Lyman series opacity τ_{eff}^{Lyman}, constrained to match the stacked spectrum at 912 Å to within 10% and assumed to decrease as $(1 + z)^{\gamma_\tau}$. Lastly, the solid red curve is the complete model that also includes the effective Lyman limit opacity τ_{912}^{LL}.

(A color version of this figure is available in the online journal.)

In the previous subsection we imposed constraints on the parameters as summarized in Table 7. We then constructed a χ^2 grid in this six-dimensional parameter space for rest wavelengths $\lambda_r = 700.0$–911.76 Å. Although the stacked spectrum extends to $\lambda_r = 600$ Å, uncertainty in the quasar SED, the evolution of τ_{eff}^{Lyman}, and sample variance are much greater at these wavelengths. Furthermore, our principle goal is to estimate λ_{mfp}^{912} which we find occurs at $\lambda_r \approx 800$ Å. These issues motivated our decision to terminate the quantitative comparison at $\lambda_r = 700$ Å.

Figure 11 shows the results for the best-fit model and the suite of models with $\Delta\chi^2 \equiv \chi_\nu^2 - \chi_{\nu,min}^2 < 0.5$. This choice for a limiting $\Delta\chi^2$ is primarily illustrative; it does not impact our uncertainty estimate for λ_{mfp}^{912}. The top panel displays the range of allowed γ_κ and $\tilde{\kappa}_{912}(z_{stack})$ values; there is an obvious degeneracy between these two parameters. In short, the data permit a more opaque universe at $z = 2.4$ that rapidly evolves to a lower opacity or a less opaque universe that evolves more slowly.

Despite this degeneracy in $\tilde{\kappa}_{912}(z_{stack})$ and γ_κ, the results imply a relatively tight constraint on λ_{mfp}^{912}. In Figure 12, we plot the $z_{912}^{\tau=1}$ values for the full set of allowed models as a function of the SED tilt $\delta\alpha_T$ and redshift evolution of the Lyman series opacity γ_τ. We find that $z_{912}^{\tau=1}$ values from 1.8–2.0 which for our adopted ΛCDM cosmology implies $\lambda_{mfp}^{912} = 150$–$300\, h_{72}^{-1}$ Mpc.
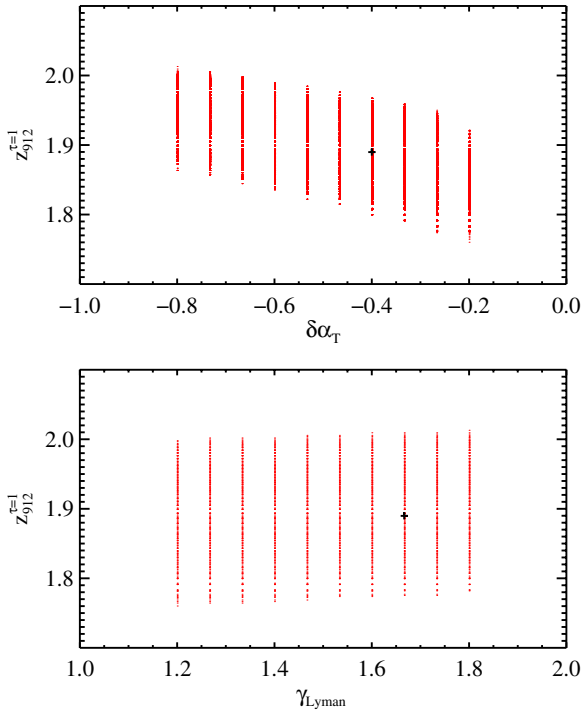
19

Figure 12. Each panel shows a crude estimate of the allowed $z_{912}^{\tau=1}$ values corresponding to $\tau_{912}^{LL} = 1$ from our analysis of the WFC3/UVIS-G280 stacked quasar spectrum, as a function of (upper) the quasar tilt $\delta\alpha_T$ and (lower) the assumed redshift evolution for τ_{eff}^{Lyman}. The plus sign indicates values from the "best fit" model shown in Figure 11. Aside from $\delta\alpha_T$ values near zero, we find $z_{912} = 1.85$–2.1 implying $\lambda_{mfp}^{912} \approx 150$–$300\ h_{72}^{-1}$ Mpc.
(A color version of this figure is available in the online journal.)

Again, we consider these estimates to be largely illustrative, not quantitative; systematic effects and sample variance dominate the uncertainty.

One approach to assessing uncertainty related to sample variance is to repeat the above analysis for a suite of stacked spectra generated by standard bootstrap techniques. Figure 13 presents the λ_{mfp}^{912} values for each of the 500 realizations of the stacked spectrum using the same formalism described above. We recover a median (mean) mean free path of $\lambda_{mfp}^{912} = 243(252)\ h_{72}^{-1}$ Mpc. We consider this value to be our best estimate for λ_{mfp}^{912} at $z = 2.44$. This same analysis suggests an uncertainty in λ_{mfp}^{912} of $\approx 20\%$. This should be considered a minimum estimate for the uncertainty. We also considered the systematic error reddening corrections might have on our stack analysis by turning off the de-reddening and re-computing λ_{mfp}^{912}. The results of this change are within our estimates on the error for λ_{mfp}^{912}, with the implied value approximately 15 Mpc lower than our fiducial value. The set of best-fit parameters are presented in Table 7.

Consider, further, the sources of error contributing to the λ_{mfp}^{912} measurement. Our analysis only considers the stacked WFC3/UVIS-G280 spectrum at rest wavelengths $\lambda_r = 700$–910 Å where one observes a rapid ($>60\%$) decline in the relative flux with decreasing λ_r. Our model of the relative flux consists of three independent effects: (1) a reduction in the flux due to the effective opacity of Lyman limit absorption τ_{eff}^{LL}; (2) an increase in the flux due to decreasing Lyman series opacity τ_{eff}^{Lyman}; and (3) changes in the flux owing to relative changes in the QSO SED. We emphasize that the latter two effects are
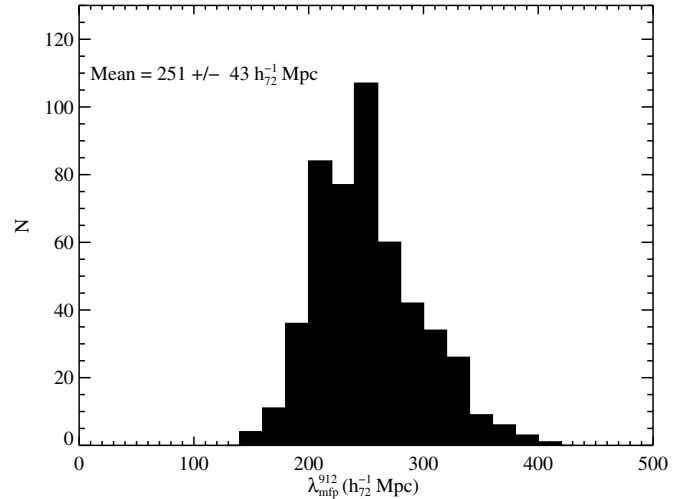

Figure 13. Bootstrap analysis of λ_{mfp}^{912} measured from the WFC3/UVIS-G280 stacked quasar spectrum ($z_{em} = 2.44$) and using the techniques describe in Section 5. The values peak at $\approx 250\ h_{72}^{-1}$ Mpc with a non-Gaussian tail extending to larger values.

expected to be small ($<10\%$ in relative flux), in particular because the analysis is performed on such a narrow range of λ_r. For example, if we ignore variations in τ_{eff}^{Lyman}, we recover the same λ_{mfp}^{912} value to within 3%. Similarly, varying the tilt in the QSO SED modifies λ_{mfp}^{912} by only several percent. These two aspects of the model, however, do work together in that they both give higher relative fluxes at lower λ_r. We find that adopting a redder QSO SED (e.g., the Telfer spectrum without any tilt) and no τ_{eff}^{Lyman} evolution would yield an $\approx 10\%$ higher λ_{mfp}^{912} value than our favored value. Even redder (i.e., $\delta\alpha_T > 0$) tilts have been considered, and would significantly increase our estimate of λ_{mfp}^{912}. These tilts are highly disfavored, however, as they summarily fail to reproduce the constraints provided by $\tau_{eff}^{Ly\alpha}$. We cannot reject the possibility that the underlying QSO SED could have additional strong inflections near rest frame wavelengths of 912 Å, thus adding significant additional uncertainties to our estimate of λ_{mfp}^{912}, but we see no indications of such features in other QSO SED studies (Telfer et al. 2002; Scott et al. 2004; Shull et al. 2012). We conclude, therefore, that uncertainties in these aspects of the modeling impose an $\approx 10\%$ systematic error in the λ_{mfp}^{912} analysis.

Presently, uncertainty in the estimated λ_{mfp}^{912} value is dominated by sample variation. As indicated in Figure 8, the stacked spectrum has an $\approx 20\%$ scatter at $\lambda_r \approx 800$ Å. This dominates the uncertainty in the results (Figure 13). We estimate that one would have to increase the sample size by at least a factor of four before uncertainties related to the QSO SED or τ_{eff}^{Lyman} would contribute substantially. Lastly, we comment that extending the λ_{mfp}^{912} analysis to lower redshifts ($z < 1.5$) where the λ_{mfp}^{912} value is presumably much larger will prove progressively more difficult. As the Lyman limit opacity has a weaker impact on the relative flux, uncertainties in the QSO SED and/or τ_{eff}^{Lyman} could dominate the analysis.

5.6. Comparisons with Other Estimates of λ_{mfp}^{912} at $z \sim 2.4$

Our bootstrap estimate of $\lambda_{mfp}^{912} = 252 \pm 52\ h_{72}^{-1}$ Mpc can now be compared with other estimates derived through different methods at this redshift, namely through application of

Equation (11) after adopting an estimate for $f(N_{H_I}, X)$. The exact approach to incorporating systems with $\tau_{912}^{LL} \approx 1$ can dramatically affect the results, and lend to very different estimates of λ_{mfp}^{912} when using this methodology. Faucher-Giguère et al. (2008a) arrive at a value of $\lambda_{mfp}^{912} = 163\,h_{72}^{-1}$ Mpc for $z = 2.4$, but establish the normalization of $f(N_{H_I}, X)$ by considering only those LLS with $\tau_{912}^{LL} > 1$. Songaila & Cowie (2010) provide new observations and analyses of LLS at $z > 4$, along with low redshift *Galaxy Evolution Explorer* LLS observations to adopt a single power law form for $f(N_{H_I}, X)$ in the LLS regime, and the same methodology as Faucher-Giguère et al. (2008a) to arrive at $\lambda_{mfp}^{912} = 172\,h_{72}^{-1}$ Mpc at $z = 2.4$. Worseck & Prochaska (2011) employ the λ_{mfp}^{912} from PWO09, plus new constraints on $f(N_{H_I}, X)$ at $14.5 < \log N_{H_I} < 19.0$ to determine a multiple power law $f(N_{H_I}, X)$, and arrive at a higher value of $\lambda_{mfp}^{912} = 220\,h_{72}^{-1}$ Mpc at $z = 2.4$. Finally, Haardt & Madau (2012) employ the $f(N_{H_I}, X)$ from POW10 to arrive at $\lambda_{mfp}^{912} = 185\,h_{72}^{-1}$ Mpc at $z = 2.4$, with a very steep redshift dependence at these redshifts (by $z = 2$, λ_{mfp}^{912} has increased to $242\,h_{72}^{-1}$ Mpc). Clearly, the derived λ_{mfp}^{912} values from $f(N_{H_I}, X)$ estimations are very sensitive to the poorly constrained regime at $\tau_{912}^{LL} \approx 1$. The methodology presented here has the advantage that it is wholly independent of $f(N_{H_I}, X)$ and the results for λ_{mfp}^{912} can then be used to offer constraints on $f(N_{H_I}, X)$, as in the next section.

6. CONSTRAINTS ON $f(N)$ AT $z \sim 2.2$

We now turn our focus to an exploration of the column density distribution function $f(N_{H_I}, X)$. Our analysis of $\ell(X)$ for the LLS along with our stacked spectrum analysis of λ_{mfp}^{912} allow us to place constraints on $f(N_{H_I}, X)$ over many decades in H I column density. We have already seen in Section 4.1.1 that we expect significant (and multiple) deviations from a single power law for $f(N_{H_I}, X)$ in order to match constraints from the Lyα forest on the low H I column density end, and the SLLS and DLA on the high H I column density column end. We address the problem in stages, from high to low N_{H_I} before performing a full and simultaneous fit to all of the observational constraints at $z \sim 2$.

6.1. Constraints on $f(N_{H_I}, X)$ for $N_{H_I} \gtrsim 10^{18}$ cm^{-2}

Our survey of Lyman limit systems provides an integral constraint on the N_{H_I} frequency distribution at high values (Equation (4); POW10). Specifically, we observe an incidence of $\tau > 2$ LLS at $z \approx 2$ of $\ell(X)_{\tau \geqslant 2} = 0.29 \pm 0.05$ corresponding to systems with $N_{H_I} \geqslant 10^{17.5}$ cm^{-2}. This integral constraint may then be compared against the observed incidence of SLLSs (10^{19} cm$^{-2} < N_{H_I} < 10^{20.3}$ cm^{-2}) and DLAs ($N_{H_I} \geqslant 10^{20.3}$ cm^{-2}) that have been estimated from surveys analyzing the damping wing of the Lyα transition (Péroux et al. 2005; Prochaska et al. 2005; O'Meara et al. 2007; Prochaska & Wolfe 2009). If one assumes a functional form for $f(N_{H_I}, X)$ at $N_{H_I} < 10^{19}$ cm^{-2}, e.g., a single power law, then we may directly constrain its parameters as follows.

Figure 7 presents our estimates for $\ell(X)_{\tau \geqslant 2}$ compared against the incidence of SLLS and DLAs, in cumulative form. For the DLAs we have assumed $\ell(X)_{DLA} = 0.05$ from the SDSS survey of Prochaska & Wolfe (2009), derived from the redshift interval $z = [2.2, 2.4]$. We note that systematic error associated with the SDSS spectral coverage affects $\ell_{DLA}(X)$ at these redshifts
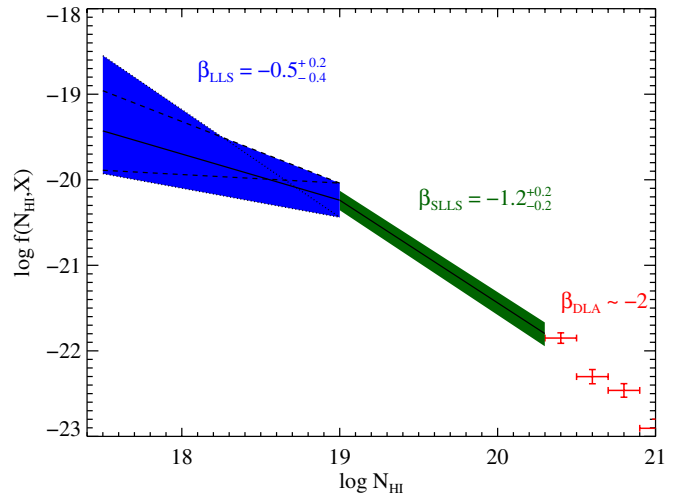

Figure 14. Estimates of the N_{H_I} frequency distribution $f(N_{H_I}, X)$ for systems with $N_{H_I} > 10^{17.5}$ cm^{-2} at $z \approx 2.4$. The measurements for the super Lyman limit systems (SLLSs) and damped Lyα systems (DLAs) were taken from O'Meara et al. (2007) and Prochaska & Wolfe (2009), respectively. The blue band is an estimate of $f(N_{H_I}, X)$ for LLSs having $N_{H_I} = 10^{17.5}$–10^{19} cm^{-2} for an assumed power law $f(N_{H_I}, X) \propto N_{H_I}^{\beta_{LLS}}$ and constrained by the observed incidence of SLLSs and $\ell(X)_{\tau \geqslant 2}$ (this paper). We find $\beta_{LLS} = -0.6_{-0.3}^{+0.2}$ (68% c.l.) for conservative estimates on the value of $f(N_{H_I}, X)$ at $N_{H_I} = 10^{19}$ cm^{-2} and allowing for the uncertainty in $\ell(X)_{\tau \geqslant 2}$. The dashed and dotted curves indicate the range of power laws that satisfy the observations.

(A color version of this figure is available in the online journal.)

(Noterdaeme et al. 2009), but the DLAs have a sufficiently small contribution that we may neglect this issue. We also adopt the $f(N_{H_I}, X)$ distribution for DLAs from Prochaska & Wolfe (2009) over the same redshift interval. This is plotted in Figure 14. For the SLLS, we adopt the value of $\ell(X)_{SLLS} = 0.13$ given by (O'Meara et al. 2007), which they derive for SLLS with $\log N_{H_I} \geqslant 19.0$ and $1.7 < z < 3$.

Together, Figure 7 shows that the SLLS and DLAs contribute $\approx 50\%$–80% of $\ell(X)_{\tau \geqslant 2}$. Even if we assume the upper end of our $\ell(X)_{\tau \geqslant 2}$ estimate,[13] it is evident that systems with $N_{H_I} = 10^{17.5}$ cm^{-2}–10^{19} cm^{-2} have a relatively modest contribution. In turn, this implies a shallow $f(N_{H_I}, X)$ for $N_{H_I} < 10^{19}$ cm^{-2}. Figure 14 shows the range of constraints for a single power law covering that N_{H_I} interval,

$$f(10^{17.5}\,\text{cm}^{-2} \leqslant N_{H_I} < 10^{19}\,\text{cm}^{-2}; X) = k_{LLS} N_{H_I}^{\beta_{LLS}}, \quad (22)$$

which assumes (1) $\ell(X)_{\tau \geqslant 2} = 0.29 \pm 0.05$; (2) $\ell_{DLA}(X) = 0.05$; (3) $\log f(N_{H_I} = 10^{19}\,\text{cm}^{-2}, X) = -20.2 \pm 0.2$. The latter constraint follows from $\ell(X)_{SLLS} = 0.13 \pm 0.04$ and $\beta_{SLLS} = -1.2 \pm 0.2$. We estimate $\log k_{LLS} = -9.2$ and $\beta_{LLS} = -0.9_{-0.05}^{+0.4}$, and note that the two parameters are highly correlated.

The derived slope for $f(N_{H_I}, X)$ in the LLS regime is very shallow; $\beta_{LLS} > -1$ implies the universe exhibits greater cross-section to gas with $N_{H_I} = 10^{19}$ cm^{-2} than 10^{18} cm^{-2}, which seems unlikely. However, a similar result was derived (in nearly identical fashion) for LLS at $z \sim 4$ by POW10. At both epochs, the relatively low incidence of $\tau > 2$ LLS implies a flattening of $f(N_{H_I}, X)$ at $N_{H_I} \approx 10^{18}$ cm^{-2} that we speculate is associated with transitioning from an optically thick to an optically thin regime. We return to this issue in Section 7.

---

[13] We further note that Ribaudo et al. (2011) reported $\ell(X)_{\tau \geqslant 2} = 0.27 \pm 0.09$ from their survey of the *HST* archive.

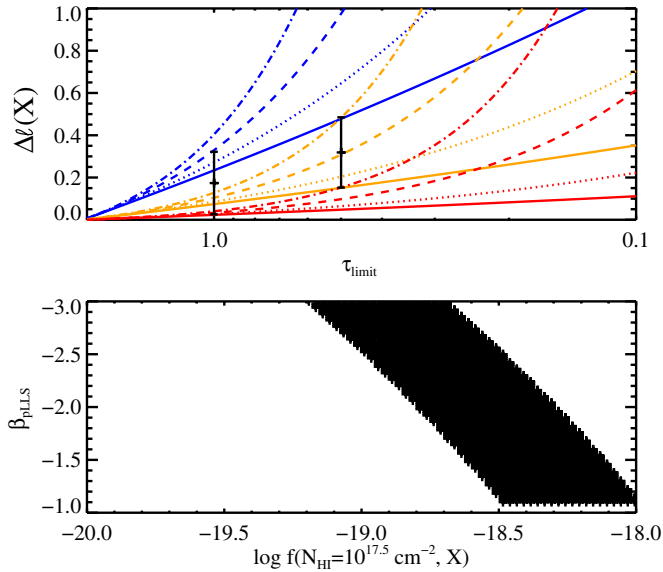**Figure 15.** Upper panel: the points with error bars show the measured offset $\Delta\ell(X)$ in incidence of LLS $\ell(X)$ from the $\tau_{\mathrm{limit}} > 2$ estimate plotted at the limiting optical depth. The curves show a series of model estimates for $\Delta\ell(X)$ as a function of τ_{limit} for an assumed $f(N_{\mathrm{H\,I}} = 10^{17.5}\,\mathrm{cm}^{-2}, X)$ of $10^{-19}\,\mathrm{cm}^2$ (red), $10^{-18.5}\,\mathrm{cm}^2$ (orange), and $10^{-18}\,\mathrm{cm}^2$ (blue). We also assume a range of slopes β_{pLLS} for an assumed single power law of -1 (solid), -1.5 (dotted), -2 (dashed), and -2.5 (dash-dotted). Models with $f(N_{\mathrm{H\,I}} = 10^{17.5}\,\mathrm{cm}^{-2}, X) < 10^{-19}\,\mathrm{cm}^2$ are ruled out by the observations. Similarly, models with $f(N_{\mathrm{H\,I}} = 10^{17.5}\,\mathrm{cm}^{-2}, X) \approx 10^{-18.5}\,\mathrm{cm}^2$ prefer $\beta_{\mathrm{pLLS}} < -1.5$. Lower panel: permitted values for β_{pLLS} and $f(N_{\mathrm{H\,I}} = 10^{17.5}\,\mathrm{cm}^{-2}, X)$ for an assumed single power law (Equation (23)) that match the observations within the 1σ uncertainty. Unless one adopts a large $f(N_{\mathrm{H\,I}} = 10^{17.5}\,\mathrm{cm}^{-2}, X)$ value, the observations require a very steep power law ($\beta_{\mathrm{pLLS}} < -1.5$).

(A color version of this figure is available in the online journal.)

6.2. Constraints on $f(N_{\mathrm{H\,I}}, X)$ for $N_{\mathrm{H\,I}} \approx 10^{17}\,cm^{-2}$

In Section 4 we presented results on the incidence of LLS for several limiting opacities at the Lyman limit: $\tau_{\mathrm{limit}} = 0.5, 1$, and 2. While these measurements are not independent[14] (they were derived from the same sightlines and the samples overlap), one may compare the results to offer an estimate for $f(N_{\mathrm{H\,I}}, X)$ in the interval $N_{\mathrm{H\,I}} = 10^{16.9}\,\mathrm{cm}^{-2} - 10^{17.5}\,\mathrm{cm}^{-2}$ corresponding to $\tau_{912}^{\mathrm{LL}} = 0.5-2$.

Once again, we parameterize $f(N_{\mathrm{H\,I}}, X)$ as a single power law,

$$f(10^{16.9}\,\mathrm{cm}^{-2} \leqslant N_{\mathrm{H\,I}} < 10^{17.5}\,\mathrm{cm}^{-2}; X) = k_{\mathrm{pLLS}} N_{\mathrm{H\,I}}^{\beta_{\mathrm{pLLS}}}. \tag{23}$$

To estimate both β_{pLLS} and k_{pLLS}, we must impose an additional constraint on $f(N_{\mathrm{H\,I}}, X)$ from the LLS analysis of the previous sub-section. Specifically, we consider the range of allowed values for $f(N_{\mathrm{H\,I}} = 10^{17.5}\,\mathrm{cm}^{-2}, X)$ which Figure 14 demonstrates could range from $\approx 10^{-18.5} - 10^{-20}\,\mathrm{cm}^2$. In Figure 15(a), we plot the offset in incidence $\Delta\ell(X)$ from the $\tau_{\mathrm{limit}} > 2$ measurement for $\tau_{\mathrm{limit}} > 1$ and $\tau_{\mathrm{limit}} > 0.5$. Overplotted on these offsets are a series of curves for the predicted offsets, as a function of τ_{limit}, for a range of $f(N_{\mathrm{H\,I}} = 10^{17.5}\,\mathrm{cm}^{-2}, X)$ and β_{pLLS} values. Models with $f(N_{\mathrm{H\,I}} = 10^{17.5}\,\mathrm{cm}^{-2}, X) < 10^{-19}\,\mathrm{cm}^2$ predict too few pLLS for $\beta_{\mathrm{pLLS}} > -2$. Indeed, only for

---

[14] We further remind the reader that $\ell(X)_{\tau \geqslant 0.5}$ was required to exceed $\ell(X)_{\tau \geqslant 2}$ in the analysis. While this must be true, it further emphasizes that the two results are highly correlated.
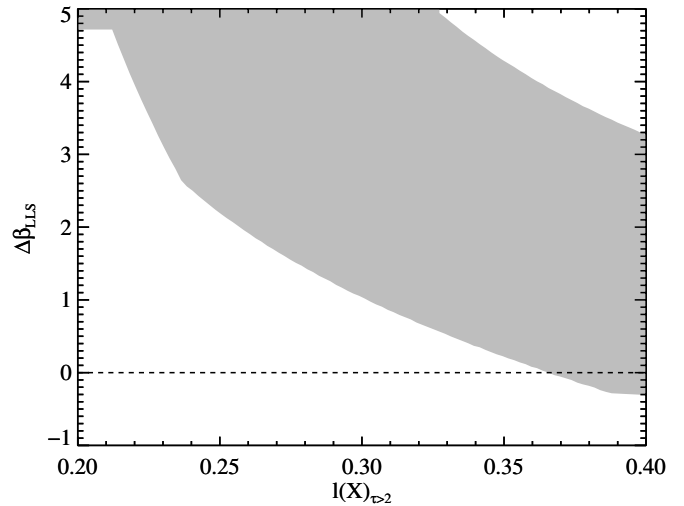

Figure 16. Estimates for the change in slope $\Delta\beta_{\mathrm{LLS}}$ of the $N_{\mathrm{H\,I}}$ frequency distribution from $N_{\mathrm{H\,I}} \approx 10^{18}\,\mathrm{cm}^{-2}$ to $10^{17}\,\mathrm{cm}^{-2}$ as inferred from the incidence of LLS at $z \approx 2$ in our *HST* survey. Results are plotted as a function of the incidence of $\tau > 2$ LLS, $\ell(X)_{\tau \geqslant 2}$. For our preferred value $\ell(X)_{\tau \geqslant 2} = 0.29 \pm 0.05$, the data indicate a significant steepening of $f(N_{\mathrm{H\,I}}, X)$ $\Delta\beta_{\mathrm{LLS}} > 1$, as one transitions from optically thick gas to optically thin regions.

$f(N_{\mathrm{H\,I}} = 10^{17.5}\,\mathrm{cm}^{-2}, X) = 10^{-18}\,\mathrm{cm}^2$ is a power law with $\beta_{\mathrm{pLLS}} \approx -1$ permitted in the pLLS regime.

This issue is further illustrated in Figure 15(b) where we indicate the allowed values for β_{pLLS} (i.e., in agreement within 1σ of both $\Delta\ell(X)$ values) as a function of $f(N_{\mathrm{H\,I}} = 10^{17.5}\,\mathrm{cm}^{-2}, X)$. We conclude that $f_{\mathrm{pLLS}}(N_{\mathrm{H\,I}}, X)$ must be steeper than $\beta_{\mathrm{pLLS}} = -1.5$ unless $f(N_{\mathrm{H\,I}} = 10^{17.5}\,\mathrm{cm}^{-2}, X) > 10^{-18.7}\,\mathrm{cm}^2$. A steepening of $f(N_{\mathrm{H\,I}}, X)$ in the pLLS regime has been previously reported by Ribaudo et al. (2011) based on their LLS analysis. Similarly, POW10 argued for a steepening of $f(N_{\mathrm{H\,I}}, X)$ at $N_{\mathrm{H\,I}} < 10^{17}\,\mathrm{cm}^{-2}$ in order reproduce the mean free path estimates of PWO09. We discuss this result further in Section 7.

While a steep $f(N_{\mathrm{H\,I}}, X)$ is permitted physically, it is quite surprising given the very shallow $f(N_{\mathrm{H\,I}}, X)$ estimated for the LLS systems in the previous sub-section. Indeed, at its extreme, the results imply a shift in slope $\Delta\beta_{\mathrm{LLS}} \equiv \beta_{\mathrm{LLS}} - \beta_{\mathrm{pLLS}}$ of unity or greater over an $N_{\mathrm{H\,I}}$ interval of ≈ 1 dex. This point is further illustrated in Figure 16 where we estimate $\Delta\beta_{\mathrm{LLS}}$ taking into account the $\ell(X)$ measurements and constraints on the SLLS (the DLA results are inconsequential). For our best estimate of $\ell(X)_{\tau \geqslant 2} = 0.3$, we recover $\Delta\beta_{\mathrm{LLS}} > 1$, i.e., a rapid steepening in $f(N_{\mathrm{H\,I}}, X)$. Only at the upper end of permissible values for $\ell(X)_{\tau \geqslant 2}$ may $\Delta\beta_{\mathrm{LLS}}$ be small. We further emphasize that any new measurements of $\ell_{\mathrm{SLLS}}(X)$ or $\ell_{\mathrm{DLA}}(X)$ that gave higher values would further increase $\Delta\beta_{\mathrm{LLS}}$.

6.3. Constraints on $f(N_{\mathrm{H\,I}}, X)$ for $N_{\mathrm{H\,I}} < 10^{17}\,cm^{-2}$

We complete our piece-meal examination of $f(N_{\mathrm{H\,I}}, X)$ by imposing constraints from the mean free path analysis of Section 5. Our evaluation of $\lambda_{\mathrm{mfp}}^{912}$ yields an additional integral constraint on $f(N_{\mathrm{H\,I}}, X)$ as described in Equation (11). Unlike $\ell(X)$, the $\lambda_{\mathrm{mfp}}^{912}$ constraint includes redshift evolution in the $N_{\mathrm{H\,I}}$ frequency distribution. Our results on $\ell(X)$ suggest very weak redshift evolution for $f(N_{\mathrm{H\,I}}, X)$ at $z < 2.5$ (Figure 6; see also Ribaudo et al. 2011), at least for systems with $N_{\mathrm{H\,I}} \approx 10^{17}\,\mathrm{cm}^{-2}$. Furthermore, our estimate of the mean free path is sufficiently short that we are only sensitive to $f(N_{\mathrm{H\,I}}, X)$ for a small redshift
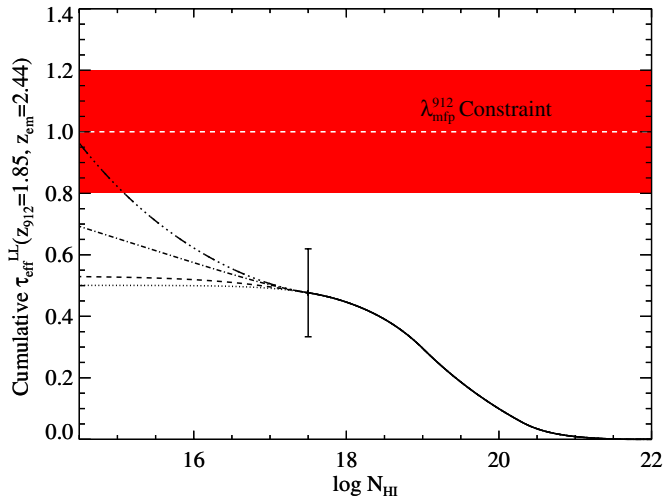
Figure 17. The curves trace the cumulative effective opacity for Lyman limit absorption $\tau_{\mathrm{eff}}^{\mathrm{LL}}$ evaluated from $z_{912} = 1.85$ to $z_{\mathrm{em}} = 2.44$ (Equation (11)). Each curve assumes an identical $f(N_{\mathrm{H\,I}}, X)$ distribution for $N_{\mathrm{H\,I}} \geqslant 10^{17.5}$ cm^{-2} as described by Figure 14. For $N_{\mathrm{H\,I}} < 10^{17.5}$ cm^{-2}, the curves adopt a fixed power law with $\beta = -1.0$ (dotted), -1.5 (dashed), -2.0 (dash-dotted), and -2.5 (triple-dot-dashed). The red shaded region shows our best estimate for τ_{912}^{LL} over this redshift interval, as assessed from our $\lambda_{\mathrm{mfp}}^{912}$ analysis (Section 7.1). This constraint strongly prefers a steep $N_{\mathrm{H\,I}}$ frequency distribution at these intermediate column densities, consistent with our analysis of the pLLS (Figure 15).

(A color version of this figure is available in the online journal.)

interval at $z \approx 2$. We proceed, therefore, by assuming no evolution in $f(N_{\mathrm{H\,I}}, X)$.

Figure 17 shows calculations of the effective Lyman limit opacity $\tau_{\mathrm{eff}}^{\mathrm{LL}}$ for a series of $f(N_{\mathrm{H\,I}}, X)$ models, identical for $N_{\mathrm{H\,I}} > 10^{17.5}$ cm^{-2} but with strict power laws at lower $N_{\mathrm{H\,I}}$ with $\beta_{\mathrm{pLLS}} = [-1, -1.5, -2, -2.5]$. In each case, we estimate $\tau_{\mathrm{eff}}^{\mathrm{LL}}$ from $z = 1.86$ to $z = 2.44$ which is the redshift interval for which our mean free path analysis yielded $\tau_{\mathrm{eff}}^{\mathrm{LL}} = 1$. The red shaded region indicates the 1σ uncertainty in this estimate.

For the favored values of $\lambda_{\mathrm{mfp}}^{912}$ and for the $f(N_{\mathrm{H\,I}}, X)$ estimates at $N_{\mathrm{H\,I}} > 10^{17.5}$ cm^{-2}, we find that LLS with $\tau > 2$ contribute approximately half of the required optical depth. Indeed, unless we adopt the largest $\lambda_{\mathrm{mfp}}^{912}$ allowed by the data and the highest incidence of LLS then systems with $N_{\mathrm{H\,I}} < 10^{17.5}$ cm^{-2} must make a significant contribution to $\tau_{\mathrm{eff}}^{\mathrm{LL}}$. Figure 17 indicates that $\beta_{\mathrm{pLLS}} \ll -1$; in fact $\beta_{\mathrm{pLLS}} < -2$ is preferred for our central values. This offers (nearly) independent evidence that $f(N_{\mathrm{H\,I}}, X)$ steepens significantly in the pLLS regime.

6.4. Joint Constraints on a Complete $f(N_{\mathrm{H\,I}}, X)$ Model

As the previous subsections reveal, our estimates of the mean free path $\lambda_{\mathrm{mfp}}^{912}$ and the incidence of LLS $\ell(X)$ provide new constraints on the $N_{\mathrm{H\,I}}$ frequency distribution $f(N_{\mathrm{H\,I}}, X)$ at $z \sim 2.5$, especially for $N_{\mathrm{H\,I}} \approx 10^{15}$–$10^{18}$ cm^{-2}. By combining these measurements with other evaluations and constraints on $f(N_{\mathrm{H\,I}}, X)$ from the literature, we may infer the $N_{\mathrm{H\,I}}$ distribution across ≈ 10 orders of magnitude. This evaluation informs astrophysical quantities sensitive to properties of the IGM (e.g., the EUVB; Haardt & Madau 2012) and provides insight into the physical origin of absorption line systems. At the most basic level, we test whether a single $f(N_{\mathrm{H\,I}}, X)$ model can reproduce all of the observational constraints. Any significant

Table 8
Revised $\lambda_{\mathrm{mfp}}^{912}$ Values from SDSS

$\langle z_q \rangle$	$\lambda_{\mathrm{mfp}}^{912}$ (Mpc^{-1})	$\sigma(\lambda_{\mathrm{mfp}}^{912})^{\mathrm{a}}$ (Mpc^{-1})
3.73	54.9	4.1
3.78	45.3	3.6
3.83	45.4	3.9
3.89	47.1	4.2
3.96	38.9	3.2
4.08	33.4	3.0
4.23	27.8	2.2

Notes. Re-evaluation of the $\lambda_{\mathrm{mfp}}^{912}$ values using the stacked SDSS quasar spectra from Prochaska et al. (2009), but update for cosmology ($H_0 = 72$ km s^{-1} Mpc^{-1}; $\Omega_m = 0.26$, $\Omega_\Lambda = 0.74$) and the definition of the mean free path applied in this paper.
[a] Based on a bootstrap analysis. There is additional systematic error not included in this estimate.

inconsistency would stress a fundamental flaw in our standard methods for studying the IGM.

Before proceeding, it is important to emphasize what may be a subtle distinction between two conceptualizations of $f(N_{\mathrm{H\,I}}, X)$: (1) an analysis of the $f(N_{\mathrm{H\,I}}, X)$ distribution that one uses to estimate quantities like $\tau_{\mathrm{eff}}^{\mathrm{Ly}\alpha}$ and $\lambda_{\mathrm{mfp}}^{912}$ (Equations (9), (11)) and (2) an observational $f(N_{\mathrm{H\,I}}, X)$ derived through line-fitting analysis of absorption-line spectra. At larger $N_{\mathrm{H\,I}}$ values, where the systems are rare and line blending is uncommon, the two types of $f(N_{\mathrm{H\,I}}, X)$ should equate. At low $N_{\mathrm{H\,I}}$, however, the two may diverge. Consider, for example, a mock spectrum generated from an analytic $f(N_{\mathrm{H\,I}}, X)$ following the procedures described in Section 5.3. One could then perform a line-profile analysis of the mock spectrum and would certainty find fewer low $N_{\mathrm{H\,I}}$ lines than inputted. Ultimately, neither type of $f(N_{\mathrm{H\,I}}, X)$ actually follows the physical description of the IGM suggested by cosmological simulations, i.e., the concept of an undulating density field. In this respect, any estimate of $f(N_{\mathrm{H\,I}}, X)$ has limited physical significance. We proceed, nevertheless, with the primary goal of estimating an analytic-oriented $f(N_{\mathrm{H\,I}}, X)$ distribution.

Absent a physically motivated model for $f(N_{\mathrm{H\,I}}, X)$, we assume that it follows a series of power laws, monotonically decreasing in value with increasing $N_{\mathrm{H\,I}}$ but discontinuous in the first derivative. This approach is partly motivated by previous estimations of $f(N_{\mathrm{H\,I}}, X)$ over modest $N_{\mathrm{H\,I}}$ intervals, but it primarily reflects our ignorance of the underlying distribution function. Analytically, a power law approach has the advantage of being robust to non-physical deviations, e.g., significant wiggles that a spline or higher-order polynomial may introduce. We normalize $f(N_{\mathrm{H\,I}}, X)$ at $N_{\mathrm{H\,I}} = 10^{12}$ cm^{-2} with the value $10^{k_{12}}$. We do not evaluate $f(N_{\mathrm{H\,I}}, X)$ for $N_{\mathrm{H\,I}} < 10^{12}$ cm^{-2} because there are very poor constraints at these column densities; for example, gas with such low column densities should contribute less than 5% to the total effective Lyα opacity.[15] We then describe $f(N_{\mathrm{H\,I}}, X)$ as a series of broken power laws with slope β in each segment defined by a series of $N_{\mathrm{H\,I}}$ "pivots." For example, $\beta_{20.3}$ defines the slope from $N_{\mathrm{H\,I}} = 10^{20.3}$ cm^{-2} to the next $N_{\mathrm{H\,I}}$ pivot. Initially, we also allowed for redshift evolution in $f(N_{\mathrm{H\,I}}, X)$, in particular to model $\lambda_{\mathrm{mfp}}^{912}$. We found, however, that the data

---

[15] Of course, such gas may trace the majority of the volume of the universe and could contribute a significant fraction of the mass density.

Table 9
$f(N_{\mathrm{H\,I}}, X)$ Constraints

Constraint	z[a]	$\log N_{\mathrm{H\,I}}$	Value[b]	Comment	Reference
			Constraints for $f(N_{\mathrm{H\,I}}, X)$ at $z \approx 2.4$		
Lya Forest	2.34	12.50–13.00	$-11.19^{+0.05}_{-0.04}$	Recalculated for our Cosmology	K02
		13.00–13.50	$-11.76^{+0.05}_{-0.05}$		
		13.50–14.00	$-12.54^{+0.07}_{-0.07}$		
		14.00–14.50	$-13.30^{+0.10}_{-0.09}$		
SLLS	2.51	19.00–19.60	$-20.63^{+0.13}_{-0.13}$	Only 30 systems total	OPB07
		19.60–20.30	$-21.50^{+0.16}_{-0.15}$		
DLA	2.51	20.30–20.50	$-21.83^{+0.06}_{-0.06}$	$z = [2.3, 2.7]$; modest SDSS bias (see Noterdaeme et al. 2009)?	PW09
		20.50–20.70	$-22.29^{+0.08}_{-0.08}$		
		20.70–20.90	$-22.41^{+0.08}_{-0.07}$		
		20.90–21.10	$-22.88^{+0.11}_{-0.10}$		
		21.10–21.30	$-23.36^{+0.15}_{-0.15}$		
		21.30–21.50	$-23.60^{+0.16}_{-0.15}$		
		21.50–21.70	$-24.33^{+0.34}_{-0.30}$		
		21.70–21.90	$-25.00^{+0.76}_{-0.52}$		
		21.90–22.10	$-99.00^{+-99.00}_{--24.63}$		
		22.10–22.30	$-99.00^{+-99.00}_{--24.83}$		
$\ell(X)_{\tau \geqslant 2}$	2.23	>17.49	0.30 ± 0.07		This paper
$\tau_{\mathrm{eff}}^{\mathrm{Ly\alpha}}$	2.40	12.00–17.00	0.198 ± 0.007	Converted to $\tau_{\mathrm{eff}}^{\mathrm{Ly\alpha}}$ from D_A. No LLS, no metals.	K05
$\lambda_{\mathrm{mfp}}^{912}$	2.44	12–22	$243 \pm 43\ h_{72}^{-1}$ Mpc		This paper
			Constraints for $f(N_{\mathrm{H\,I}}, X)$ at $z \approx 3.7$		
Lya Forest	3.75	13.65–14.05	$-12.42^{+0.10}_{-0.10}$	Read from Figure 4	K01
SLLS	3.58	19.00–19.60	$-20.37^{+0.12}_{-0.12}$	$z = [3.1, 4.5]$	OPB07
		19.60–20.30	$-21.22^{+0.14}_{-0.13}$		
DLA	3.61	20.30–20.50	$-21.68^{+0.06}_{-0.06}$	$z = [3.3, 4.2]$; modest SDSS bias (see Prochaska et al. 2009)	PW09
		20.50–20.70	$-21.98^{+0.07}_{-0.07}$		
		20.70–20.90	$-22.45^{+0.10}_{-0.10}$		
		20.90–21.10	$-22.71^{+0.11}_{-0.10}$		
		21.10–21.30	$-23.28^{+0.17}_{-0.16}$		
		21.30–21.50	$-23.53^{+0.18}_{-0.17}$		
		21.50–21.70	$-23.93^{+0.24}_{-0.22}$		
		21.70–21.90	$-24.53^{+0.45}_{-0.37}$		
		21.90–22.10	$-99.00^{+-99.00}_{--24.45}$		
		22.10–22.30	$-99.00^{+-99.00}_{--24.65}$		
β	3.70	12.50–14.00	-1.30 ± 0.15	Shallower than $z=2$, but very uncertain.	See text
$\ell(X)_{\tau \geqslant 2}$	3.76	>17.49	0.52 ± 0.07		POW10
$\tau_{\mathrm{eff}}^{\mathrm{Ly\alpha}}$	3.70	12.00–19.00	0.795 ± 0.062	Higher than other evaluations.	FG08
$\lambda_{\mathrm{mfp}}^{912}$	3.69	12–22	$51 \pm 5\ h_{72}^{-1}$ Mpc		PWO09

Notes.
[a] Effective redshift where the constraint was determined.
[b] $f(N_{\mathrm{H\,I}}, X)$ constraints are given in log.
Reference. KT97: Kirkman & Tytler 1997; K01: Kim et al. 2001; K02: Kim et al. 2002; K05: Kirkman et al. 2005; OPB07: O'Meara et al. 2007; PW09: Prochaska et al. 2009.

offered only very weak constraints. In the following, we assume a $(1 + z)^{1.5}$ evolution in $f(N_{\mathrm{H\,I}}, X)$, which is roughly consistent with the observed evolution in $\tau_{\mathrm{eff}}^{\mathrm{Ly\alpha}}$ at these redshifts (Kirkman et al. 2005).

In addition to the observational constraints imposed by the results of this paper ($\lambda_{\mathrm{mfp}}^{912}$, $\ell(X)$), we also include (1) evaluations of $f(N_{\mathrm{H\,I}}, X)$ estimated from the line-fitting survey of Kim et al. (2002) but re-evaluated to our own choice of $N_{\mathrm{H\,I}}$ binning and to our assumed cosmology. We restrict the evaluations to $N_{\mathrm{H\,I}} < 10^{14.5}$ cm^{-2} to maintain significant statistical power; (2) measurements of $f(N_{\mathrm{H\,I}}, X)$ for SLLS

from O'Meara et al. (2007); (3) measurements of $f(N_{\mathrm{H\,I}}, X)$ for DLAs from Prochaska & Wolfe (2009); and (4) an estimate of $\tau_{\mathrm{eff}}^{\mathrm{Ly\alpha}}$ (from D_A) at $z = 2.4$ (Kirkman et al. 2005). Table 9 lists these constraints and we discuss a few modifications to the reported values and errors below.

From the empirical constraints, we construct deviates between observation y and model m, $d \equiv (y - m)/\sigma$, with σ the 1σ uncertainty. This includes the integral constraints on $f(N_{\mathrm{H\,I}}, X)$: $\tau_{\mathrm{eff}}^{\mathrm{Ly\alpha}}$, $\ell(X)$ and $\lambda_{\mathrm{mfp}}^{912}$. For all of these, we assume Gaussian errors which is not formally correct but offers a fair approximation. For the case of $\tau_{\mathrm{eff}}^{\mathrm{Ly\alpha}}$, Kirkman et al. (2005)

estimated an error of only 3% but we adopt a more conservative error of 10% to account for systematic uncertainty and the fact that our model assumes a fixed Doppler parameter for the Lyα forest of $b = 24\,\mathrm{km\,s^{-1}}$. We adopt a model with the same constraint as the Kirkman et al. (2005) analysis that was restricted to systems with $N_{\mathrm{H\,I}} < 10^{17.2}\,\mathrm{cm^{-2}}$, but which includes metal line absorption. For the highest $N_{\mathrm{H\,I}}$ values (constrained by the DLAs), we calculate the deviate from $N_{\mathrm{H\,I}} = 10^{21.5}$–$10^{22.3}\,\mathrm{cm^{-2}}$ and consider this as a single constraint. Lastly, we optimized our parametric model with the software package MPFIT with initial guesses estimated through a by-eye comparison to the various constraints.

It is illustrative to consider a series of $f(N_{\mathrm{H\,I}}, X)$ models with increasing complexity, i.e., an increasing number of power law segments, to establish the simplest model which satisfies all constraints. Following the results of the previous sub-section, we model $f(N_{\mathrm{H\,I}}, X)$ at $N_{\mathrm{H\,I}} > 10^{18}\,\mathrm{cm^{-2}}$ with a series of three power laws, defined by $N_{\mathrm{H\,I}}$ pivots at $\log N_{\mathrm{H\,I}} = 20.3$ and 21.5 dex. We then optimized a 4-parameter model for $f(N_{\mathrm{H\,I}}, X)$ under the full set of observational constraints. This model assumes a single power law with slope β_{12} from $N_{\mathrm{H\,I}} = 10^{12}$–$10^{20.3}\,\mathrm{cm^{-2}}$. Not surprisingly, the model yields very poor results with a reduced chi-squared $\chi_\nu^2 > 10$. The model cannot match the shallow slope suggested by $\ell(X)$ (Figure 14) with the steep slope implied by $\lambda_{\mathrm{mfp}}^{912}$ (Figure 17) and the Lyα forest observations. In short, the data require a break in $f(N_{\mathrm{H\,I}}, X)$ below $N_{\mathrm{H\,I}} = 10^{18}\,\mathrm{cm^{-2}}$.

We next evaluated a set of 5-parameter models (4 power laws) with an additional $N_{\mathrm{H\,I}}$ pivot at $\approx 10^{17.5}\,\mathrm{cm^{-2}}$. To our surprise, we found this model well-reproduced ($\chi_\nu^2 \approx 1$) the $\tau_{\mathrm{eff}}^{\mathrm{Ly}\alpha}$, $\lambda_{\mathrm{mfp}}^{912}$, $\ell(X)$, and SLLS/DLA constraints provided $\beta_{12} \approx -1.65$ (Figure 18(a)). This implies a significant break to a shallower $f(N_{\mathrm{H\,I}}, X)$ ($\Delta\beta > 0.6$) for the LLS. Perhaps coincidentally, this slope is in good agreement with the shape of $f(N_{\mathrm{H\,I}}, X)$ reported for the $z < 1$ universe (Penton et al. 2004; Lehner & Howk 2007). This model also implies that absorption with low $N_{\mathrm{H\,I}}$ values ($< 10^{13.5}\,\mathrm{cm^{-2}}$) contribute significantly ($\sim 50\%$) to the effective Lyα opacity. In turn, the model severely over-predicts the incidence of such weak absorbers compared to the empirical estimations of Kim et al. (2002). Those authors reported a more shallow $f(N_{\mathrm{H\,I}}, X)$ at $N_{\mathrm{H\,I}} < 10^{14}\,\mathrm{cm^{-2}}$, inconsistent with our 5-parameter model. On the other hand, such low $N_{\mathrm{H\,I}}$ absorption is the most subject to uncertainties associated with S/N, continuum placement, and line blending. We also posit that this difference may be a manifestation of the distinction between the analytic and observational $f(N_{\mathrm{H\,I}}, X)$ distributions noted above. We proceed to consider a yet more complex model but note that one is not entirely required.

In an effort to reproduce all of the observational constraints given in Table 9, we examined a 6-parameter model (5 power laws) that includes two $N_{\mathrm{H\,I}}$ pivots between $\log N_{\mathrm{H\,I}} = 14$ and 19 dex. We experimented with parameterizing these two $N_{\mathrm{H\,I}}$ pivots and found very weak constraints on their values. Therefore, we have fixed them at $N_{\mathrm{H\,I}} = 10^{14.5}\,\mathrm{cm^{-2}}$ and $N_{\mathrm{H\,I}} = 10^{17.5}\,\mathrm{cm^{-2}}$ and caution that the results should not be considered unique. Figure 18(b) presents the best-fit $f(N_{\mathrm{H\,I}}, X)$ distribution compared against the observational constraints. The reduced χ^2 is near unity and is dominated by the $f(N_{\mathrm{H\,I}}, X)$ evaluations at low and high $N_{\mathrm{H\,I}}$. This model shows a shallow distribution function at low $N_{\mathrm{H\,I}}$ which steepens to $\beta_{14.5} \approx -2$ at $N_{\mathrm{H\,I}} \gtrsim 10^{14.5}\,\mathrm{cm^{-2}}$, as inferred by Kim et al. (2002). Again, we conclude that $f(N_{\mathrm{H\,I}}, X)$ is steeper than $\beta = -1.6$ at
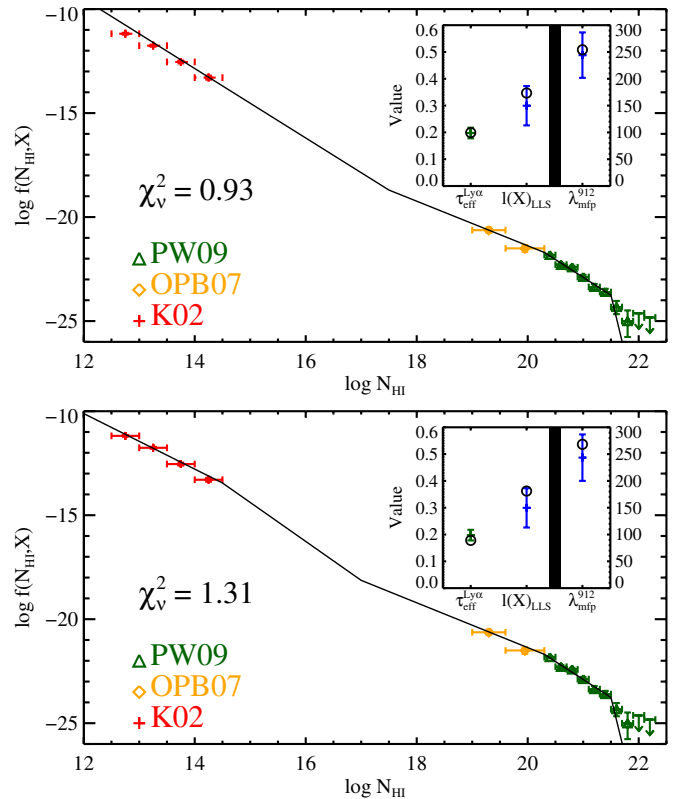

Figure 18. $N_{\mathrm{H\,I}}$ frequency distribution function at $z = 2.4$, as modeled by a series of broken power laws. The black curve shows the best-fit model, with parameters listed in Table 10. This model was derived by minimizing the reduced χ^2 calculated against the observational constraints shown in the figure (see also Table 9). This includes estimates of $f(N_{\mathrm{H\,I}}, X)$ for the Lyα forest (K01; Kim et al. 2001), the SLLS (OPB07 O'Meara et al. 2007), and the DLAs (PW09 Prochaska & Wolfe 2009). Furthermore, we adopted a model constraint on the power law index in the Lyα forest (Kim et al. 2002) and integral constraints on the opacity of the Lyα forest (Kirkman et al. 2005). Lastly, we also adopted results on $\lambda_{\mathrm{mfp}}^{912}$ and $\ell(X)$ estimated in this paper. We find that this simple (and assuredly non-physical) model for $f(N_{\mathrm{H\,I}}, X)$ provides a good description of all these observations.

(A color version of this figure is available in the online journal.)

$N_{\mathrm{H\,I}} \approx 10^{15}\,\mathrm{cm^{-2}}$ and then transitions to $\beta \approx -1$ in the LLS regime. This is consistent with our inferences based on the $\lambda_{\mathrm{mfp}}^{912}$ and partial LLS analyses (Sections 5.5, 6.3).

Despite the relatively low χ_ν^2 value for this 6-parameter model, there is significant tension. A shallow $f(N_{\mathrm{H\,I}}, X)$ at low $N_{\mathrm{H\,I}}$ values requires that a significant fraction of the Lyα opacity arise from systems with $N_{\mathrm{H\,I}} \approx 10^{14}\,\mathrm{cm^{-2}}$. Indeed, a 6-parameter model that pivots at $N_{\mathrm{H\,I}} = 10^{14}\,\mathrm{cm^{-2}}$ instead of $10^{14.5}\,\mathrm{cm^{-2}}$ under-predicts the $\tau_{\mathrm{eff}}^{\mathrm{Ly}\alpha}$ value and may be ruled out. The model shown in Figure 18, meanwhile, over-predicts the Kim et al. (2002) estimates of $f(N_{\mathrm{H\,I}}, X)$ at $N_{\mathrm{H\,I}} > 10^{14}\,\mathrm{cm^{-2}}$. As the precision in the observations improves, we speculate that it may become impossible to generate an $f(N_{\mathrm{H\,I}}, X)$ distribution that satisfies all of the constraints.

To summarize our main findings on $f(N_{\mathrm{H\,I}}, X)$ at $z \approx 2.4$:

1. All 4-parameter (3 power law) models for $f(N_{\mathrm{H\,I}}, X)$ are ruled out by the observations.
2. A 5-parameter model with a single power law ($\beta \approx -1.65$) spanning from $N_{\mathrm{H\,I}} = 10^{12}\,\mathrm{cm^{-2}}$ to $\approx 10^{17.5}\,\mathrm{cm^{-2}}$ reproduces the $\tau_{\mathrm{eff}}^{\mathrm{Ly}\alpha}$, $\lambda_{\mathrm{mfp}}^{912}$, $\ell(X)$, and SLLS/DLA observations well. This model predicts a large contribution to the

Table 10
Model and Correlation Matrix for the 5-Parameter $f(N_{\rm H\,I}, X)$

Param	Best	σ^{a}	δk_{12}	$\delta\beta_{12}$	$\delta\beta_{17.5}$	$\delta\beta_{20.3}$	$\delta\beta_{21.5}$
			Model for $f(N_{\rm H\,I}, X)$ at $z \approx 2.4$				
k_{12}	-9.52	0.07	1.00	-0.91	0.48	-0.06	0.01
β_{12}	-1.67	0.02	-0.91	1.00	-0.70	0.09	-0.02
$\beta_{17.5}$	-1.07	0.03	0.48	-0.70	1.00	-0.53	0.11
$\beta_{20.3}$	-1.71	0.12	-0.06	0.09	-0.53	1.00	-0.30
$\beta_{21.5}$	-11.10	7.54	0.01	-0.02	0.11	-0.30	1.00

Note. [a] Evaluated from the diagonal of the covariance matrix.

effective Lyα opacity from gas with low $N_{\rm H\,I}$ values and also over-predicts the incidence of such gas compared to the line analysis of Kim et al. (2002). Such line analysis is challenged, however, by S/N, continuum placement, and line blending and we recommend further consideration of the systematic uncertainties.

3. To fit the $f(N_{\rm H\,I}, X)$ evaluations from Kim et al. (2002), one must consider a 6-parameter model (5 power laws). This allows for a shallow $f(N_{\rm H\,I}, X)$ ($\beta_{12} \approx -1.3$) at $N_{\rm H\,I} \lesssim 10^{14}\,{\rm cm^{-2}}$ that must break sharply to a steep distribution ($\beta_{14.5} \approx -2$) for intermediate $N_{\rm H\,I}$ values.

4. All of the successful models require a relatively steep ($\beta < -1.6$) distribution function for $N_{\rm H\,I} = 10^{15}$–$10^{17}\,{\rm cm^{-2}}$ that then flattens in the LLS regime to $\beta \approx -1$.

Table 10 lists the best-fit values, the 1σ uncertainties derived from the diagonal elements of the covariance matrix, and the correlation matrix for the model. The parameters are well constrained, with the exception of the slope at $N_{\rm H\,I} > 10^{21.5}\,{\rm cm^{-2}}$ which is best considered as an upper limit ($\beta_{21.5} < -3$; Prochaska et al. 2005). On the other hand, several of the parameters are highly correlated (e.g., k_{12} and β_{12}) and one cannot assert that our model is unique. We also caution that our analysis ignored the parametric freedom of pivot placement; their values were motivated by the observations. Lastly, we re-emphasize that the broken power law model is assuredly non-physical and therefore an incomplete description of the universe. Nevertheless, the results impose a general description of $f(N_{\rm H\,I}, X)$, whose implications are discussed below.

7. DISCUSSION

We now consider the larger implications of our results.

7.1. Evolution in $\ell(X)$ and $\lambda_{\rm mfp}^{912}$

In Figure 19, we present our measurement of $\lambda_{\rm mfp}^{912}$ along with the revised results of PWO09 at higher redshift, which are given in Table 8. Overplotted on Figure 19 are curves which describe the evolution in $\lambda_{\rm mfp}^{912}$ with redshift when assume the 5-parameter model functional form for the IGM at $z = 2.4$. The different curves correspond to allowing $\ell(z)$ to evolve as $(1+z)^{\gamma}$, and letting γ vary from 1.5 to 2.5. The curves are forced to have the same value, and match the PWO09 SDSS result at $z = 4$. The importance of our new measurement for $\lambda_{\rm mfp}^{912}$ is immediately obvious: without information at lower redshifts, the high-redshift data has no discriminatory value in γ. With the inclusion of the *HST* data, however, we can rule out extrema in γ, especially toward the high end. Specifically, we can rule out $\gamma = 2.5$. We note that our results are again consistent with those of Ribaudo et al. (2011), who favor a value of $\gamma = 1.8$.
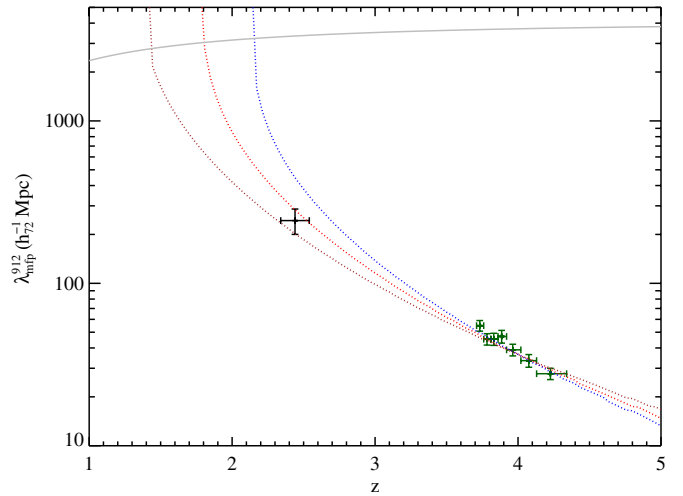

Figure 19. The data points trace the $\lambda_{\rm mfp}^{912}$ measurements as a function of redshift from this paper ($z \approx 2.44$; black) and the SDSS analysis of PWO09 ($z \sim 4$; green). The colored curves show the predicted evolution in $\lambda_{\rm mfp}^{912}$ for a series of assumed $f(N_{\rm H\,I}, X)$ models. Each has the functional form derived for the IGM at $z = 2.4$ (the 5 parameter model given in Table 10). We have allowed, however, the incidence of absorbers $\ell(z)$ to evolve as $(1+z)^{\gamma}$ with $\gamma = 1.5, 2.0, 2.5$ for line colors brown, red, and blue, respectively. Furthermore, each of the curves was forced to intersect the SDSS measurements at $z = 3.9$. Our WFC3/UVIS-G280 measurement rules out $\gamma = 1.5$ and favors $\gamma \approx 2$ which coincides well with the redshift evolution in $\ell(z)$ reported by Ribaudo et al. (2011). The gray curve in the figure traces the Horizon of the universe with redshift. An extrapolation of the $\lambda_{\rm mfp}^{912}$ curves predicts that the "breakthrough" epoch occurs at $z \approx 1.5$–2.

(A color version of this figure is available in the online journal.)

Their analyses, however, only explicitly determines $\lambda_{\rm mfp}^{912}$ for systems with $\tau_{912} > 2$. Figure 19 also shows the need for further exploration of $\lambda_{\rm mfp}^{912}$ at other redshifts, specifically at $z < 2$, $z \simeq 3$, and $z \geqslant 4.5$, to provide a full description of the evolution of $\lambda_{\rm mfp}^{912}$ over cosmic time. Songaila & Cowie (2010) present a measurement of $\lambda_{\rm mfp}^{912}$ at $5 < z < 6$ from the Echellette Spectrograph and Imager spectra which indicate a slightly lower value for $\lambda_{\rm mfp}^{912}$ than would be predicted from lower redshift power law fits, but we caution that the number of spectra in their sample is relatively low, and that their method for determining $\lambda_{\rm mfp}^{912}$ involves a number of assumptions not made in our analysis here.

The solid gray curve in Figure 19 shows the Horizon of the universe as a function of redshift. When $\lambda_{\rm mfp}^{912}$ exceeds this radius, ionizing photons are capable of traveling the visible universe before being attenuated. In this respect, every source of ionizing photons can "see" the other. This epoch is termed the "breakthrough" redshift (e.g., Meiksin & Madau 1993). Given
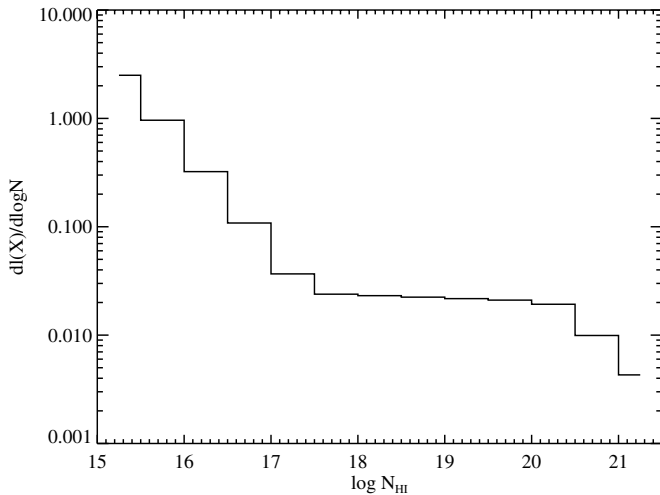
Figure 20. Differential contribution of absorption systems to $\ell(X)$ as a function of $N_{\mathrm{H\,I}}$, $d\ell(X)/d\ln N_{\mathrm{H\,I}}$. Abrupt changes in this quantity mirror inflections in $f(N_{\mathrm{H\,I}}, X)$. The transitions away from the near constancy of this quantity across the LLS regime are likely linked to ionization properties of the gas, either with the onset of the gas being optically thick ($N_{\mathrm{H\,I}} = 10^{17.2}$ cm^{-2}), or the onset of self-shielding ($N_{\mathrm{H\,I}} = 10^{20.5}$ cm^{-2}).

the current constraints on $\lambda^{912}_{\mathrm{mfp}}$ and the simple models presented in Figure 19, our best estimate is $z_{\mathrm{break}} = 1.6$ and we require $z_{\mathrm{break}} < 2$. Future observations on the incidence of optically thick absorption at $z \lesssim 1$ should firmly establish the value (J. C. Howk et al., in preparation).

7.2. The Inflection in $f(N_{\mathrm{H\,I}}, X)$ through the LLS Regime

One of the primary results of our analysis is that the frequency of systems with $N_{\mathrm{H\,I}} \lesssim 10^{17}$ cm^{-2} is significantly higher than that predicted from a simple extrapolation of the $f(N_{\mathrm{H\,I}}, X)$ distribution estimated for $N_{\mathrm{H\,I}} > 10^{17}$ cm^{-2}. Stated another way, our results demand a higher frequency of pLLS than one would predict based on the incidence of LLS. We have reached this conclusion from two complementary analysis of our dataset: (1) the direct counting of pLLS versus LLS (Figure 15); and (2) our analysis for the total effective Lyman limit opacity of LLS (Figure 17). Each of these results imply the steepening of $f(N_{\mathrm{H\,I}}, X)$ with decreasing $N_{\mathrm{H\,I}}$. Such a steepening of $f(N_{\mathrm{H\,I}}, X)$ at $N_{\mathrm{H\,I}} \lesssim 10^{17.2}$ has been inferred previously at $z = 3.7$ (POW10) based on $\lambda^{912}_{\mathrm{mfp}}$ analysis and at $z \approx 1.5$ from a direct survey of pLLS (Ribaudo et al. 2011).

This result is further illustrated in Figure 20 which plots the differential contribution of systems to $\ell(X)$ per $\Delta \log N_{\mathrm{H\,I}} = 0.5$ dex interval, $\Delta\ell(X)/\Delta \log N_{\mathrm{H\,I}}$. These $\Delta\ell(X)/\Delta \log N_{\mathrm{H\,I}}$ values were simply calculated from the power law description of $f(N_{\mathrm{H\,I}}, X)$ shown in Figure 18(b). As with $\ell(X)$, each evaluation here is proportional to the comoving number density of sources, n_c, that give rise to the absorption times their average physical cross-section ΔA at that range of column densities. For $N_{\mathrm{H\,I}} < 10^{17}$ cm^{-2}, the $\Delta\ell(X)$ values rise steeply with decreasing $N_{\mathrm{H\,I}}$. At $N_{\mathrm{H\,I}} \approx 10^{17.5}$ cm^{-2}, however, the $\Delta\ell(X)$ values flatten and are nearly constant until $N_{\mathrm{H\,I}} \approx 10^{20.5}$ cm^{-2}. This simply reflects, of course, the "inflection" in $f(N_{\mathrm{H\,I}}, X)$ across the LLS regime.

The flattening of $f(N_{\mathrm{H\,I}}, X)$ as $N_{\mathrm{H\,I}}$ decreases from $\approx 10^{20.5}$ has been recognized and discussed previously (O'Meara et al. 2007; Prochaska et al. 2010) at higher redshifts, and also at $z \sim 0$ (Corbelli & Bandiera 2002). This is expected to occur because of the transition in gas from a predominantly neutral

state to a predominantly ionized plasma (Zheng & Miralda-Escudé 2002). This leads to a significantly lower cross-section for gas with $N_{\mathrm{H\,I}} \leqslant 10^{20}$ cm^{-2} than otherwise and hence an observed flattening in $\Delta\ell(X)/\Delta \log N_{\mathrm{H\,I}}$. Detailed radiative transfer calculations of galaxies in high-resolution cosmological simulations have confirmed this picture (Faucher-Giguère & Kereš 2011; Fumagalli et al. 2011; Altay et al. 2011).

The steepening of $f(N_{\mathrm{H\,I}}, X)$ at $N_{\mathrm{H\,I}} \approx 10^{17}$ cm^{-2} with decreasing $N_{\mathrm{H\,I}}$ suggests a similar "phase transition." Because $N_{\mathrm{H\,I}} = 10^{17.2}$ cm^{-2} corresponds to $\tau^{\mathrm{LL}}_{912} = 1$, the obvious culprit for an inflection is the transition from the optically thin regime to optically thick gas. Qualitatively, this may work as follows. For systems with $N_{\mathrm{H\,I}} \ll 10^{17.2}$ cm^{-2}, the material is optically thin and one expects to receive roughly the same radiation field from the EUVB. In this case, the distribution of $N_{\mathrm{H\,I}}$ values that result is dominated by the distribution of densities within the volume (e.g., Schaye 2001). Our results indicate an $N_{\mathrm{H\,I}}$ distribution characterized by $f(N_{\mathrm{H\,I}}, X) \propto N_{\mathrm{H\,I}}^{-2}$. In the absence of radiation transfer effects (i.e., the transition to optically thick gas), we may presume that the $N_{\mathrm{H\,I}}$ distribution would have shown a similar shape for $N_{\mathrm{H\,I}} > 10^{17}$ cm^{-2}. Instead, as the gas becomes optically thick, the radiation field has been attenuated and one recovers a higher H I column density than in the optically thin limit. This non-linear effect naturally leads to the flattening of $f(N_{\mathrm{H\,I}}, X)$ at $N_{\mathrm{H\,I}} \approx 10^{17}$ cm^{-2}. A full treatment of these effects within the context of cosmological simulations is clearly warranted.

7.3. Evolution in $f(N_{\mathrm{H\,I}}, X)$

Buoyed by the relative success of our analysis, we reconsider the $N_{\mathrm{H\,I}}$ frequency distribution at $z \sim 3.7$, previously evaluated by Prochaska et al. (2010). Table 9 lists the observational constraints. For the Lyα forest ($N_{\mathrm{H\,I}} = 10^{12}$–$10^{14.5}$ cm^{-2}), we adopt a constraint on the slope of $f(N_{\mathrm{H\,I}}, X)$ based on line-fitting analysis (e.g., Kirkman & Tytler 1997; Kim et al. 2002). We allow for significant uncertainty in this constraint since, as explored by these and other authors, issues such as continuum placement, completeness, and non-uniqueness of models to address line blending often arise, especially at higher redshifts. The normalization of $f(N_{\mathrm{H\,I}}, X)$ at these low column densities is set by the integrated opacity $\tau^{\mathrm{Ly}\alpha}_{\mathrm{eff}}$. At $z \sim 4$, there is significant disagreement in the empirical estimates of $\tau^{\mathrm{Ly}\alpha}_{\mathrm{eff}}$; Faucher-Giguère et al. (2008b) report a value $\tau^{\mathrm{Ly}\alpha}_{\mathrm{eff}} \approx 0.8$ while other authors have published much lower values ($\tau^{\mathrm{Ly}\alpha}_{\mathrm{eff}} \approx 0.7$ Kim et al. 2007; Dall'Aglio et al. 2008). The difference in these values substantially exceeds the estimated uncertainties, statistical and systematic. In our primary analysis, we adopt the higher value but then comment on the implications of lower values. The other empirical constraints are estimates of $f(N_{\mathrm{H\,I}}, X)$ from the SLLS and DLAs (O'Meara et al. 2007; Prochaska & Wolfe 2009), and $\lambda^{912}_{\mathrm{mfp}}$ and $\ell(X)$ integral constraints (PWO09, POW10).

Table 10 summarizes the best-fit model for $z = 3.7$, error estimates, and the correlation matrix while Figure 21 presents a comparison of the best-fit model with the data. Similar to the $z = 2.4$ analysis, we find that a six parameter model (with identical $N_{\mathrm{H\,I}}$ pivots) provides a good description of the observational constraints at $z = 3.7$. More remarkably, the best-fit slopes all lie within 1σ of the estimates at lower redshift. The only statistically significant evolution lies in the normalization; k_{12} is ≈ 0.3 dex higher at higher redshift.
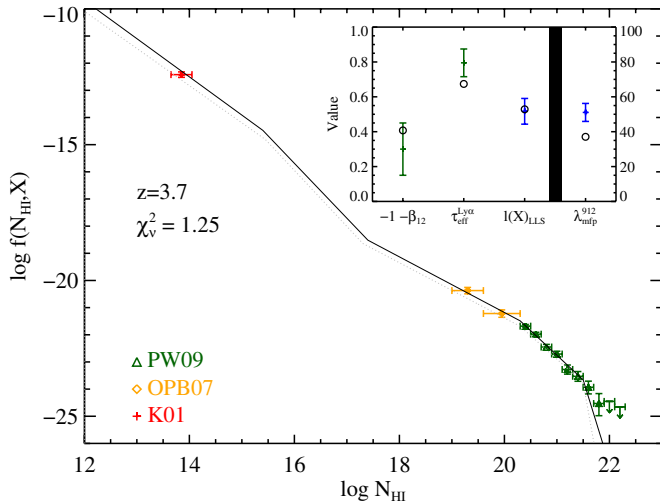
Figure 21. Similar to Figure 18 but for $z = 3.7$ and, therefore, for a different set of observational constraints (Table 9). For $\tau_{\rm eff}^{\rm Ly\alpha}$, we adopted the estimate of Faucher-Giguère et al. (2008b) and the $\ell(X)$ and $\lambda_{\rm mfp}^{912}$ measurements from POW10 and PWO09, respectively. The dotted gray line shows the best-fit model of $f(N_{\rm H\,I}, X)$ at $z = 2.4$. It has nearly identical shape but is offset to lower normalization by ≈ 0.3 dex.

(A color version of this figure is available in the online journal.)

The apparent lack of evolution in the shape of $f(N_{\rm H\,I}, X)$ between redshifts 2.4 and 3.7 takes on additional interest when we consider the strong evolution in $\ell(X)$ over the same timescale. As $\ell(X)$ relates to the comoving number density of absorbers and their physical size, we can surmise from our results that although either (or both) of these two quantities must evolve with time, a change in the column density distribution of absorbers producing the LLS does not. This implies that if it is the change in physical size which is providing the bulk of the evolution in $\ell(X)$, and if the LLS arise in galaxy halos, the distribution of the gas within the halos is the same over cosmic time. The same conclusion is reached by Fumagalli et al. (2011) in their simulations.

7.4. Implications for the Nature of LLS

Finally, we consider these results in the context of current understanding on the origin of the LLS. At low redshift, it has been statistically established that systems with $N_{\rm H\,I} \gtrsim 10^{14.5}$ cm^{-2} are associated with the circumgalactic medium (CGM) of galaxies (Prochaska et al. 2011; Rudie et al. 2012). Specifically, galaxies of all luminosity show a very high covering fraction of significant Lyα absorption to impact parameters $r \approx 300$ kpc which may be defined as the extended CGM of these systems. Prochaska et al. (2011) demonstrate that n_c for $L > 0.01\,L^*$ galaxies at $z \sim 0$ is large enough that all of the strong Lyα absorbers (>0.3 Å) are associated with this extended CGM. At high z, one also observes a significantly higher incidence of H I absorption in the CGM of $L \approx L^*$ galaxies (Rakic et al. 2012) and a remarkably high incidence of optically thick gas in the CGM of galaxies hosting quasars (Hennawi & Prochaska 2007). One may infer, therefore, that gas with $N_{\rm H\,I} \gtrsim 10^{15}$ cm^{-2} at $z \sim 2$ primarily traces the extended CGM of high z galaxies. From numerical simulations, one reaches similar conclusions (e.g., Fumagalli et al. 2011; van de Voort et al. 2012).

Recent work in cosmological simulations has also produced $f(N_{\rm H\,I}, X)$ with numerous inflections. For example, Altay et al.

(2011) provide a determination of $f(N_{\rm H\,I}, X)$ at $z = 3$ through a combination of line-fitting at low $N_{\rm H\,I}$ and projection at $N_{\rm H\,I}$ in the LLS and DLA regime. Their $f(N_{\rm H\,I}, X)$ is consistent with those presented here at both $z = 2.4$ and $z = 3.7$. Of particular interest is their observation that the presence of self-shielding produces the flattening of $f(N_{\rm H\,I}, X)$ in the LLS regime, as discussed above. Unfortunately, their results are constrained to a single redshift. Van de Voort et al. (2012) use the same set of simulations but focus instead on the gas fraction in halos, and the future history of LLS gas. They conclude that the majority of LLS gas is in cold-mode galaxy halo gas and will be incorporated in those galaxies' ISM within 1.2 Gyr. While they do not provide estimates of $f(N_{\rm H\,I}, X)$ at other z, one may interpret their result along with our observed lack in evolution of $f(N_{\rm H\,I}, X)$ to imply that to maintain the shape of $f(N_{\rm H\,I}, X)$ at later times in the universe, cold gas must continue to be placed in galaxy haloes and be observed as LLS. Finally, Fumagalli et al. (2011) also find that the majority of LLS are cold-mode gas. Notably, they follow their simulations through the redshift range $1.4 < z < 4$ and find, in agreement with our results, that $f(N_{\rm H\,I}, X)$ does not evolve with time.

8. SUMMARY AND FUTURE WORK

We have presented the first scientific results from our *HST* program to study Lyman limit absorption at redshift $z \simeq 2$. We have:

1. Determined $\ell(z)$ and $\ell(X)$ over the redshift range $1 < z < 2.6$, finding a weighted mean of $\ell(X) = 0.29 \pm 0.05$ for $2.0 < z < 2.5$.
2. Stacked our WFC3 spectra to find a median (mean) value of the mean free path to ionizing radiation of $\lambda_{\rm mfp}^{912} = 243(252)\,h_{72}^{-1}$ Mpc with an error on the mean value of $\pm 43\,h_{72}^{-1}$ Mpc.
3. Shown either that the SED of $z \sim 2$ quasars is harder than those at $z \sim 1$ or that there are significant systematics in the SDSS selection function.
4. Constrained the evolution of $\lambda_{\rm mfp}^{912}$ with redshift, and estimating the breakthrough redshift to be $z = 1.6$. The methodology behind this result is subject to the assumption that there are no significant inflections in the intrinsic QSO spectrum other than the one required to produce the observed Lyα forest opacity. Including further inflections would produce very large uncertainties in the derived $\lambda_{\rm mfp}^{912}$.
5. Shown that no 4-parameter (3 power laws) form can describe $f(N_{\rm H\,I}, X)$ at $z = 2.4$, and provide a best-fit 5-parameter model.
6. Shown that $f(N_{\rm H\,I}, X)$ does not vary significantly in shape between $z = 2.4$ and $z = 3.7$.

While the current data sample are more than adequate to constrain the incidence of LLS and their contribution to $f(N_{\rm H\,I}, X)$ and $\lambda_{\rm mfp}^{912}$ at $z \sim 2$, they are of too poor resolution to make any statements on metal absorption in the LLS. Given their increased number over the DLA at these (and all) redshifts, the LLS likely contribute to a significant fraction of the metal budget. In the next paper in this series, we combine our *HST* results with those from Keck+HIRES to address the metallicity of LLS at $z \sim 2$, a quantity which is currently poorly constrained.

REFERENCES

Altay, G., Theuns, T., Schaye, J., Crighton, N. H. M., & Dalla Vecchia, C. 2011, ApJL, 737, L37
Bahcall, J. N., & Peebles, P. J. E. 1969, ApJL, 156, L7
Baldwin, J. A. 1977, ApJ, 214, 679
Calverley, A. P., Becker, G. D., Haehnelt, M. G., & Bolton, J. S. 2011, MNRAS, 412, 2543
Corbelli, E., & Bandiera, R. 2002, ApJ, 567, 712
Dall'Aglio, A., Wisotzki, L., & Worseck, G. 2008, A&A, 491, 465
Faucher-Giguère, C.-A., & Kereš, D. 2011, MNRAS, 412, L118
Faucher-Giguère, C.-A., Lidz, A., Hernquist, L., & Zaldarriaga, M. 2008a, ApJ, 688, 85
Faucher-Giguère, C.-A., Prochaska, J. X., Lidz, A., Hernquist, L., & Zaldarriaga, M. 2008b, ApJ, 681, 831
Fitzpatrick, E. L., & Massa, D. 1990, ApJS, 72, 163
Fumagalli, M., Prochaska, J. X., Kasen, D., et al. 2011, MNRAS, 418, 1796
Haardt, F., & Madau, P. 1996, ApJ, 461, 20
Haardt, F., & Madau, P. 2012, ApJ, 746, 125
Hennawi, J. F., & Prochaska, J. X. 2007, ApJ, 655, 735
Hui, L., & Rutledge, R. E. 1999, ApJ, 517, 541

Janknecht, E., Reimers, D., Lopez, S., & Tytler, D. 2006, A&A, 458, 427
Kim, T., Cristiani, S., & D'Odorico, S. 2001, A&A, 373, 757
Kim, T.-S., Bolton, J. S., Viel, M., Haehnelt, M. G., & Carswell, R. F. 2007, MNRAS, 382, 1657
Kim, T.-S., Carswell, R. F., Cristiani, S., D'Odorico, S., & Giallongo, E. 2002, MNRAS, 335, 555
Kirkman, D., & Tytler, D. 1997, ApJ, 484, 672
Kirkman, D., Tytler, D., Lubin, D., & Charlton, J. 2007, MNRAS, 376, 1227
Kirkman, D., Tytler, D., Suzuki, N., et al. 2005, MNRAS, 360, 1373
Lanzetta, K. M. 1991, ApJ, 375, 1
Lehner, N., & Howk, J. C. 2007, MNRAS, 377, 687
Madau, P., Ferguson, H. C., Dickinson, M. E., et al. 1996, MNRAS, 283, 1388
Madau, P., Haardt, F., & Rees, M. J. 1999, ApJ, 514, 648
McQuinn, M., Oh, S. P., & Faucher-Giguère, C.-A. 2011, ApJ, 743, 82
Meiksin, A., & Madau, P. 1993, ApJ, 412, 34
Meiksin, A. A. 2009, RvMP, 81, 1405
Miralda-Escudé, J. 2003, ApJ, 597, 66
Noterdaeme, P., Petitjean, P., Ledoux, C., & Srianand, R. 2009, A&A, 505, 1087
O'Meara, J. M., Prochaska, J. X., Burles, S., et al. 2007, ApJ, 656, 666
O'Meara, J. M., Prochaska, J. X., Chen, H.-W., & Madau, P. 2011, ApJS, 195, 16
Penton, S. V., Stocke, J. T., & Shull, J. M. 2004, ApJS, 152, 29
Péroux, C., Dessauges-Zavadsky, M., D'Odorico, S., Kim, T.-S., & McMahon, R. G. 2003, MNRAS, 345, 480
Péroux, C., Dessauges-Zavadsky, M., D'Odorico, S., Sun Kim, T., & McMahon, R. G. 2005, MNRAS, 363, 479
Péroux, C., Storrie-Lombardi, L. J., McMahon, R. G., Irwin, M., & Hook, I. M. 2001, AJ, 121, 1799
Petitjean, P., Webb, J. K., Rauch, M., Carswell, R. F., & Lanzetta, K. 1993, MNRAS, 262, 499
Prochaska, J. X., Herbert-Fort, S., & Wolfe, A. M. 2005, ApJ, 635, 123
Prochaska, J. X., O'Meara, J. M., & Worseck, G. 2010, ApJ, 718, 392
Prochaska, J. X., Weiner, B., Chen, H.-W., Mulchaey, J., & Cooksey, K. 2011, ApJ, 740, 91
Prochaska, J. X., & Wolfe, A. M. 2009, ApJ, 696, 1543
Prochaska, J. X., Worseck, G., & O'Meara, J. M. 2009, ApJL, 705, L113
Prochter, G. E., Prochaska, J. X., O'Meara, J. M., Burles, S., & Bernstein, R. A. 2010, ApJ, 708, 1221
Rakic, O., Schaye, J., Steidel, C. C., & Rudie, G. C. 2012, ApJ, 751, 94
Rauch, M. 1998, ARA&A, 36, 267
Ribaudo, J., Lehner, N., & Howk, J. C. 2011, ApJ, 736, 42
Richards, G. T., Fan, X., Newberg, H. J., et al. 2002, AJ, 123, 2945
Richards, G. T., Strauss, M. A., Fan, X., et al. 2006, AJ, 131, 2766
Rudie, G. C., Steidel, C. C., Trainor, R. F., et al. 2012, arXiv:1202.6055
Sargent, W. L. W., Steidel, C. C., & Boksenberg, A. 1989, ApJS, 69, 703
Schaye, J. 2001, ApJ, 559, 507
Schlegel, D. J., Finkbeiner, D. P., & Davis, M. 1998, ApJ, 500, 525
Scott, J. E., Kriss, G. A., Brotherton, M., et al. 2004, ApJ, 615, 135
Shull, J. M., Stevans, M., & Danforth, C. W. 2012, ApJ, 752, 162
Songaila, A., & Cowie, L. L. 2010, ApJ, 721, 1448
Stengler-Larrea, E. A., Boksenberg, A., Steidel, C. C., et al. 1995, ApJ, 444, 64
Storrie-Lombardi, L. J., McMahon, R. G., Irwin, M. J., & Hazard, C. 1994, ApJL, 427, L13
Telfer, R. C., Zheng, W., Kriss, G. A., & Davidsen, A. F. 2002, ApJ, 565, 773
Tytler, D. 1982, Natur, 298, 427
Tytler, D. 1987, ApJ, 321, 49
Tytler, D., Kirkman, D., O'Meara, J. M., et al. 2004, ApJ, 617, 1
van de Voort, F., Schaye, J., Altay, G., & Theuns, T. 2012, MNRAS, 421, 2809
Vanden Berk, D. E., Richards, G. T., Bauer, A., et al. 2001, AJ, 122, 549
Verner, D. A., Ferland, G. J., Korista, K. T., & Yakovlev, D. G. 1996, ApJ, 465, 487
Wolfe, A. M., Gawiser, E., & Prochaska, J. X. 2005, ARA&A, 43, 861
Worseck, G., & Prochaska, J. X. 2011, ApJ, 728, 23
Zheng, Z., & Miralda-Escudé, J. 2002, ApJL, 568, L71